The Fabrication and Characterisation of Semiconductor Sensitized Photoanodes

Lauren Ann King

2012

Supervised by Prof. Jason D. Riley

A thesis presented for the degree of Doctor of Philosophy in the Department of Materials of Imperial College London and the Diploma of Imperial College London

I, Lauren Ann King, declare that the work presented in this thesis is my own. Where information has been derived from other sources, I confirm that this has been indicated in the thesis.

Lauren Ann King

29th December 2012

Abstract

Cadmium selenide (CdSe) quantum dots (QDs) and molybdenum disulfide (MoS_2) are considered as effective light harvesting assemblies for application in semiconductor sensitized solar cells (SSSCs).

CdSe QDs were synthesized following a trioctylphosphine oxide (TOPO) stabilized hot injection method. Prior to sensitization, QDs are subject to a common purification; cycles of alternate precipitation/re-dispersion in a non-solvent/solvent. Our study reveals the critical role of purification. With enhanced purification, the QD concentration at a functionalised surface has been shown to increase 5-fold. Imaging reveals that QD agglomerates on the surface decrease in size and increase in population. Photocurrent measurements demonstrate the importance of the morphology and QD population on QD photoinjection and thus the necessity to control purification.

Polysulfide electrolyte is the most commonly utilized electrolyte in quantum dot sensitized solar cells (QDSSCs). To date, there have been relatively few investigations into the stability of CdSe QDs in polysulfide solution. Bulk CdSe crystals have long been known to undergo sulfur substitution reactions resulting in CdS layers of a few nanometres thickness at the surface of CdSe crystals. Here, post exposure to polysufide a red-shift in the absorbance, and photocurrent onset of QDs is observed. Through structural, chemical and optical studies of QD only, and QD sensitized TiO_2 samples, the shift in onset is attributed to a combination of change in both QD structure and film morphologies.

Due to their photocatalytic stability and appropriate band gaps, group 6 transition metal dichalcogenides (TMD) such as MoS_2 have long been considered candidates for photoelectrochemical cells (PEC). Low dimensional materials have recently attracted significant attention, and in particular monolayer MoS_2 has been highlighted for its unique optical properties. Upon decreasing thickness, the indirect band gap of bulk MoS_2 shifts to a direct gap material for monolayer crystals. Here we investigate the photoelectrochemical properties of ultra-thin films of chemically exfoliated MoS_2 and its composites with TiO_2 nanoparticles. MoS_2 monolayer films are shown to exhibit effective PEC properties similar to bulk

materials, generating photocurrent at excitation wavelengths above the direct band gap edge at ~660 nm. We also demonstrate that MoS_2 monolayers sensitized to TiO_2 behave as effective photosensitizers. We find that in PEC cells with TiO_2-MoS_2 composite photoanodes, excited electrons in MoS_2 are able to inject into TiO_2 while holes are removed by the electrolyte so as to generate electrical current from incident light. Our results demonstrate the potential of solution-processed MoS_2 monolayers for PEC applications.

Table of Contents

Glossary

AFM: atomic force microscopy

APCE: absorbed photon conversion efficiency

CB: conduction band

Cd: cadmium

CdS: cadmium

CdSe: cadmium selenide

DA: direct absorbance

DSSC: dye sensitized solar cell

Eg: energy gap

FIB-SEM: focused ion beam – secondary electron microscopy

FT-IR: Fourier Transfer – Infrared

FTO: fluorine doped tin oxide

FWHM: full width half maximum

HOMO: highest occupied molecular orbital

ICP-OES: inductively coupled plasma – optical emission spectroscopy

IPCE: incident photon conversion efficiency

IR: infrared

LUMO: lowest unoccupied molecular orbital

MEG: multiple electron generation

MoS_2: molybdenum disulfide

3-MPA: 3-mercaptopropionic acid

Na_2S: sodium sulfide

Na_2SO_3: sodium sulfite

NMR: nuclear magnetic resonance

OTE: optically transparent electrode

PEC: photoelectrochemical cell

PL: photoluminescence

PV: photovoltaics

QD: quantum dot

QDSSC: quantum dot sensitized solar cell

S: sulfur

Se: selenium

SEM: scanning electron microscopy

SHE: standard hydrogen electrode

SIMS: secondary ion mass spectrometry

SSC: sensitized solar cell

SSSC: semiconductor sensitized solar cell

TEM: transmission electron microscopy

TiO_2: titanium dioxide

TMD: transition metal dichalogenide

TRES: time resolved emission spectroscopy

UV: ultra violet

UV-Vis: ultra violet visible

VB: valence band

VDW: van der Waal

XPS: x-ray photoelectron spectroscopy

List of Figures

Chapter 1. Introduction

Chapter 2. Fabrication, Instrumentation and Characterisation

Chapter 3. The Influence of Purification on QD Sensitization

Chapter 4. The Influence of Polysulfide Electrolyte on CdSe QDs

Figure 4.5. Typical examples of SEM and corresponding EDX of untreated (A) and polysulfide (B) and (C) polysulfide treated CdSe films. The areas analysed with EDX are shown in green boxes on each image.

Figure 4.6. SIMS profiles for CdSe single crystal samples; negative (a) and (b) and positive (c) and (d) ions are shown separately. (a) and (c) profiles are for CdSe untreated samples; (b) and (d) for polysulfide treated CdSe samples.

Figure 4.7. FT-IR spectra of an untreated (blue) and polysulfide treated (red) CdSe film. An FTO reference spectrum is also shown (black). Some of the distinct peaks/regions known to be present in the QD capping layer are labelled.

Figure 4.8. Low magnification SEM images of untreated (A (2 K magnification) and B (5 K magnification)) and polysulfide treated (C (2 K magnification) and D (5 K magnification)) CdSe films.

Figure 4.9. Higher magnification (15 K magnification) SEM images of untreated (A and B) and polysulfide treated (C and D) CdSe films.

Figure 4.10. High magnification SEM images of untreated (A and B (100 K magnification)) and polysulfide treated (C and D (50 K magnification)) CdSe films.

Figure 4.11. Typical low magnification (15 K) cross-sectional SEM images of untreated (A and B) and polysulfide treated (C and D) CdSe films.

Figure 4.12. STEM micrographs of QD sensitized TiO_2 imaged with the TITAN TEM at magnifications (A) 450 K and (B) 640 K.

Figure 4.13. (a) Absorbance and (b) normalized absorbance spectra (linear measurement) of an untreated CdSe QD film (on FTO) before (black) and after (red) polysulfide treatment. Both were measured in water/polysulfide solution. (c) Total absorbance of the same, dry films (measured with an integrating sphere). (d) The wavelength dependent change in absorbance plotted with the inverse of wavelength to the power of four.

Figure 4.14. Photoluminescence response of CdSe QD film before (black) and after (red) polysulfide treatment. The films were excited at 500 nm. (a) is the raw photoluminescence spectra; (b) is the normalized data (data points) and corresponding Gaussian fits (line).

Figure 4.15. (a) Temporal evolution of the absorbance spectra (linear measurement). The first measurement (black) was conducted pre-polysulfide treatment. (b) λ_{max} (the first excitonic peak absorbance spectra) of the QD film plotted with respect to time. All measurements were conducted in water/sodium sulphite solution.

Figure 4.16. (a) Evolution of absorbance with respect to time at 620 nm, 600 nm, 580 nm, 560 nm, 540 nm and 520 nm (b) normalized with absorbance at

first excitonic peak position, (c) normalized with absorbance at first excitonic peak position, the first 1600 s is only shown.

Figure 4.17. Photoluminescence delay rate, fit and instrument response function (IRF) trace of (a) untreated CdSe film, (b) polysulfide treated CdSe film and (c) CdSe QD sol used to prepare the films. The data was recorded with 560 nm excitation.

Figure 4.18. IPCE photocurrent (continuous lines) and normalized absorbance (dashed line) (at the first excitation peak) spectra measured in 0.5 M Na_2SO_3 (pH 7) pre (blue) and post (red) polysulfide treatment. The photocurrent was measured at 0 V against a silver/silver chloride reference electrode with a lock-in amplifier with a chopper frequency of 0.5 Hz.

Figure 4.19. The absorbed photon conversion efficiency (APCE) for the untreated (blue) and polysulfide treated (red) cadmium selenide photoanodes. The spectra were calculated from the data presented in Figure 4.18 and Figure 4.13(c).

Figure 4.20. IPCE photocurrent spectra of TiO_2 only film measured in pH 7, 0.5 M Na_2SO_3 pre (blue) and post (red) polysulfide treatment.

Figure 4.21. Photocurrent spectra of untreated (blue) and polysulfide treated (red) QD sensitized TiO_2 photoanode. The absorbance of the (untreated) QD sol is plotted for comparison.

Chapter 5. An Alternative Sensitizer, Molybdenum Disulfide

Figure 5.1. Schematic representing the route to MoS_2-TiO_2 electrodes. A. Addition of colloidal MoS_2 to TiO_2 nanoparticles. B. Doctor blade the composite paste onto FTO conductive glass to anneal at 300˚C in an argon atmosphere.

Figure 5.2. (a) UV-VIS absorbance of the MoS_2 thin films of different thicknesses (see legend) deposited on FTO conductive glass and annealed in a nitrogen environment at 300˚C. The average film thicknesses were calculated from the empirical data of reference.[17] The inset shows the absorbance dependence on MoS_2 thickness for each of the four excitonic peaks A, B, C and D. (b) An approximate interband structure for MoS_2 adapted from ref[21]. The transitions labelled A, B, C and D correspond to the transitions labelled in (a).

Figure 5.3. Normalized absorbance spectra (a) entire spectra, (b) 400 – 500 nm only, highlighting the red shift in absorbance peak for the thinnest films.

Figure 5.4. (a) Averaged (3 data for each film thickness) APCE spectra of the MoS_2 films of different film thickness (solid lines) conducted at 0 V potential against Ag/AgCl/1 M KCl reference electrode. The spectra are overlaid with the normalized UV-Vis absorbance of a thin (1.7 nm) MoS_2 film (dashed black line). It is of note that relatively large APCE signals recorded for $\lambda > 680$ nm is due to

accentuated noise (the monolayer has extremely low absorbance across this region, the IPCE data is shown in b). (c) Wavelength specific APCE values plotted with respect to film thickness.

Figure 5.5. (a) The average IPCE photocurrent response plotted against potential (v SHE reference electrode) of a 4 nm MoS_2 film on FTO substrate. Between every second and third potential photocurrent measurement, the IPCE was re-measured at 0 V to confirm that the sample had not degraded from the photocatalytic efficiency. (b) The possible mechanistic routes for the decay of a C/D exciton. On the right hand side (red), k_1 and k_2 are the possible routes of injection of the electron into the FTO. On the left hand side (blue), k_3, k_4 and photoluminescence (k_6) are the competing recombination loss mechanisms. We propose that the upper conduction band can also decay to the lower conduction band via k_5.

Figure 5.6. The Raman spectra of TiO_2, MoS_2 and MoS_2-TiO_2 composite films after annealing. (a) Full scale (b) The enlarged spectra at 400 cm^{-1} evidencing the presence of MoS_2.

Figure 5.7. (a) SEM and (b) TEM image of an annealed TiO_2 film. (c) SEM and (b) TEM image of MoS_2-TiO_2 film. Lattice planes circled in blue corresponds to TiO_2. Red arrows indicate lattice fringes assigned as MoS_2.

Figure 5.8. (a) Averaged IPCE (3 data sets) photocurrent spectra (solid lines) of MoS2/TiO_2 composite (blue and red) and TiO_2 only films (green). The spectra are overlaid with the normalized absorbance of 1.7 nm MoS2. (b) The estimated APCE for the prepared composite films. The estimate is calculated utilizing the known concentration and volume of MoS_2 in each photoanode. The vertical dashed line represents the onset of photocurrent response from TiO_2.

Figure 5.9. Schematic representing the conduction bands (positioning and relevant gaps) of MoS_2 and TiO_2 plotted on SHE scale. The energy levels of TiO_2 and MoS_2 were obtained from ref 28 and ref 21, respectively.

Appendix

Figure A.1. Schematic for the three step assembly of photoanodes. A. Addition of 1 M 3-MPA to the TiO2 particles. B. Addition of QD sol. C. Doctor blade QD-3-MPA-TiO_2 onto FTO conductive glass.

Figure A.2. Normalized UV-visible absorbance spectra for the QD sol and films; untreated (red), pressed (green), annealed (blue) and pressed and annealed (purple).

Figure A.3. Normalized photoluminescence spectra for an untreated (blue) and annealed (red) CdSe film.

Figure A.4. Normalized photoluminescence spectra of untreated (black) and pressed (red) CdSe films.

Figure A.5. Transient Photocurrent spectra of a pressed TiO_2 only film. The measurement is conducted with chopped illumination (frequency of chopping was altered throughout measurement). (a) is enlarged over the first 1000 s, (b) full data. Red lines (dotted) represent the turning on of light (400nm), blue lines are where the light is blocked.

Figure A.6. Normalized average IPCE spectra for pressed (blue), annealed (red) and pressed and annealed (black) QD sensitized TiO_2 photoanodes. TiO_2 only is also shown for reference (green). All measurements were conducted in 0.5 M Na_2SO_3, pH 7.

List of Publications

Journal publications from this thesis:

1) Laurie A King and D. Jason Riley "Importance of QD Purification Procedure on Surface Adsorbance of QDs and Performance of QD Sensitized Photoanodes" *Journal of Physical Chemistry C*, 116, 3349–3355, 2012.

2) Laurie A. King, Weijie Zhao, Manish Chhowalla, D. Jason Riley and Goki Eda "Photoelectrochemical properties of chemically exfoliated MoS_2", s*ubmitted.*

Acknowledgements

There are so many people in this world who have shared so much with me and without whom this thesis would not have been possible. Firstly I thank Jason for his infinite electrochemical and general chemistry knowledge. Always willing to listen, and full of interesting ideas and suggestions, you have also given me so many opportunities to travel to conferences and courses which really have taught me so much. I would also like to highlight special thanks to Goki for his molybdenum disulfide, his guidance and his general kindness.

Within the department of Materials, there have been many technicians and academic staff who without whom much of this work would not have been possible. In particular I must emphasise my thanks to Katy, Mahmoud, Ben, and Ivo who have been so imperative to helping me with so much of the experimental work in this thesis.

A PhD is only possible with great lab-mates. Over the past 3 years there have been an uncountable number Postdocs, PhD and Master students who have worked in the lab with me. Some of you brought me laughter, happiness and departmental gossip, some of you just brought me fear for my life expectancy, but all of you taught me so much. In particular, I could not have reached this point without Alice, who's name I still pronounce incorrectly, but you literally got me through each and every day particularly by revolutionising my 10.45 am; Ning, our alpha male, always caring and ready to help; Little Teo, always willing to eat roast chicken, up for a chat and has great music taste; Susi, the break dancer, but also the sweetest person I have ever met. Finally, Lefteris, you have also helped me so much, especially with the science in the final push for this thesis; thank you. To all of the guys who've been in the offices with us; and in particular the Starbucks frequenters, Chaek/Ted, thank you for bringing such laughter and friendship to these years.

Away from work there are so many friends and family members who have shaped these three years. Most importantly of all, I have to thank my sister, Babs, primarily for not knowing or caring about anything in the world of science, not even gravity. I would also like to thank my parents for their "advice" and, if I'm honest,

for inspiring me to push this far. Also, Ted; Project X really has rocked my world. To my grandparents, you have always been there for me, each in a different and yet truly inspiring way; thank you so much.

There are many other friends who have always been there for me. In particular Jambo, Ratchet, Lizzy, Harry and the rest of the Flan; Richard and Lucy too, you are particularly wonderful. To Dominik, I thank you for your sheer delight in titanium dioxide and, of course, your love of a Duvel. I also thank Alex, Martyn and all other past and present members of the Tizard family for filling every second of my waking day with something to do and generally making me smile.

This thesis is dedicated to all of you mentioned here. It's been tricky, but also a lot of fun. Most of all I hope that one day I can inspire others to take part and care for the world of science as much as you have taught me to.

LAK

Chapter 1. Introduction

1.1 Motivation

The depletion of fossil fuels combined with extensive scientific evidence outlining the catastrophic effects of burning such fuels (climate change) and the growing energy demand, illustrates the necessity for alternative, clean energy sources.[1-3] New and sustainable energy resources are paramount to maintaining the current lifestyles of the 7 billion (and growing) inhabitants of the planet. The options currently available for the replacement of fossil fuels are nuclear power and the renewable energy technologies. Renewable energy technologies rely on capturing the natural energy fluxes from wind, gravity, geothermal heat, the sun and tidal power.

The ultimate solution for the replacement of fossil fuels will undoubtedly be an amalgamation of renewable energies, nuclear, fusion and other "carbon free" technologies. Solar energy is the largest sustainable, clean, free, environmentally benign and highly abundant energy resource.[4,5] The total amount of solar energy that illuminates the earth each day is sufficient to supply the energy of the planet for an entire year. Despite the immense and free energy resource, photovoltaics (solar power) currently contributes less than 0.01 % of worldwide energy production.[3] It is estimated that by covering 0.16 % of the planet's surface with 10 % efficient solar modules would be sufficient to match the projected energy requirements (20 TW) of the earth by 2050.[6] Whilst this remains an ambitious challenge, photovoltaics will undoubtably play a vital role in the replacement of fossil fuels.

In combination with a drive to enhance the fundamental scientific understanding of the solar cells presented herein, the opportunity to promote solar radiation as a clean and renewable energy source has been a source of motivation for this work.

1.2 Photovoltaic devices

The phenomenon whereby electrons are ejected from a material when exposed to photons (of sufficient energy) is known as the photoelectric effect. The photoelectric effect was discovered in 1839 by Edmond Becquerel.[7] Experimentally, Becquerel observed that direct current was produced when a silver coated platinum electrode

immersed in electrolyte connected to a counter electrode, was illuminated with light. Photovoltaic devices (PV) utilize the photoelectric effect to convert solar energy into electricity. Solar flux spans energies of approximately 0.3 – 4 eV (Figure 1.1) and hence, an optimised solar cell must harvest the majority of photons in this region. It is the fraction of the solar flux converted into electrical power which determines the efficiency of a device. Hence, a compromise between voltage and current limits the theoretical power efficiency of an ideal solar cell. This is approximately 33% in a single junction photovoltaic cell (determined by a combination of recombination, spectral and blackbody losses).[8]

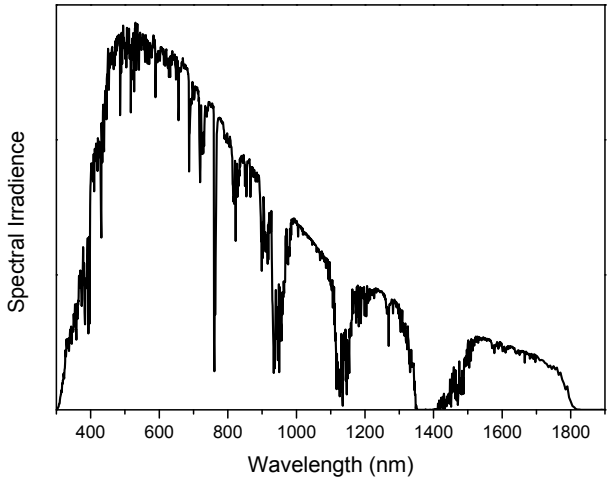

Figure 1.1. The power spectrum of sunlight that reaches the Earth.

In a typical PV, it is at the interface between materials (at least one material is photoactive) where electron hole charge separation can be induced. In a homojunction or heterojunction solar cell, the bandgap, E_g of the absorbing semiconductor determines the minimum threshold of photon energy ($h\nu$) that can be absorbed by the device to excite an electron (only $h\nu > E_g$ will be absorbed). Photons of energy less than E_g, will not be absorbed and thus the device will not produce photocurrent. Photons incident at the junction (of sufficient energy) excite electrons to higher energy levels (conduction band) and thus holes (empty electron state) form within the valence band. Due to the inbuilt potential gradient at the junction between the materials, the electrons and holes move in opposite directions, preventing recombination and thus giving rise to photocurrent.

Several different types of PV have been developed; however, the commercial market remains dominated by silicon based solid state junction devices. Categorised by Green as *first* generation PV,[9] single crystal silicon based devices have power efficiencies approaching 25 %.[10] The commercial expansion of solar powered renewable energy technologies is driven by lower costs and hence a *second* generation PV evolved, fabricated using "thin film" technologies. Thin film modules are similar to first generation PV with respect to device efficiencies, however, due to the significantly thinner photoactive layer and hence reduced materials cost, the solar cells are significantly cheaper to manufacture.

For market expansion of PV technologies, a reduced module cost is often considered the primary goal. There are, however, several other desirable features and characteristics in designing a commercially viable device. These include the production of flexible, lightweight modules by solution processed and low temperature manufacturing. Such motivation has driven the development of *third* generation PV. These combine multiple layers of semiconductors (each layer harvests a different portion of sunlight) and have demonstrated up to 30% efficiencies.[11] However, to date, such cells are not financially viable in the current market (with the exception of their use in space satellites where cost is not a limiting factor).[4] Alternative initiatives for *third* generation PV are currently under consideration. Examples include advanced systems composed of nanomaterials and/or organic materials.[12,13] However, to date, such approaches have achieved relatively low efficiencies, thus these technologies require further research to develop understanding and improve their PV efficiencies. One of the promising third generation PV technologies are "sensitized solar cells", a particular class of which is the focus of the research presented in this thesis. Here a review of the sensitized solar cells is provided with special attention given to the semiconductors that are the focus of this research.

1.3 Sensitized Solar Cells (SSCs)

Sensitized solar cells (SSCs) are composed of three main components; the sensitizer (a material which absorbs photons resulting in the promotion of an electron from its ground state), a large band gap (typically mesoporous titanium dioxide) to which the sensitizer is anchored, and a charge transport electrolyte (typically a redox couple

which regenerates the sensitizer post electron injection). The top contact (photoactive layer side) is electrically connected by a transparent conductor; the back contact is made with an appropriate counter electrode.

1.3.1 Dye Sensitized Solar Cells (DSSCs)

Since first reported in 1991, the dye sensitized solar cell (DSSC) has attracted significant attention from the scientific community, with over 8,800 citations of the original Nature paper (December 2012).[14] This attention is due to a combination of appealing factors which highlight the potential for DSSC commercialisation. Of particular note, DSSCs can be readily manufactured from cheap materials which can be solution processed and printed. In addition to commercialisation of the DSSC, due to a common basis in the fundamental science, DSSCs research is readily transferable to other technologies and applications such as photoelectrochemical cells (PECs)[15] and solar-to-fuel devices[16,17] and thus the field has attracted even wider attention. There are several reviews on DSSCs providing in depth overviews of the device operation,[18-23] optimization of dyes[24] and electron transfer kinetics[25]. Here, a brief overview of the structure and device operation is given.

Architecturally, a DSSC is composed of a photoanode, electrolyte and counter electrode connected externally across an external load (Figure 1.2). Dye molecules (referred to as "sensitizers") anchored to the surface of a wide band-gap semiconducting material such as titanium dioxide (TiO_2) absorb photons exciting an electron from the highest occupied molecular orbital (HOMO) to the lowest unoccupied molecular orbital (LUMO). The photoexcited electron in LUMO is then able to inject into the TiO_2 layer and diffuse through the TiO_2 layer to exit the photoanode through an external circuit. The LUMO energy level must therefore be above the conduction band energy level of the TiO_2 to favour injection of the photoexcited electron. The photoanode is electrochemically connected to the counter electrode by an electrolyte redox couple which acts as an electron shuttle; transporting electrons from the counter electrode to the working electrode of the cell and reacting with the oxidised dye. The general device architecture and kinetics of operation are shown in Figure 1.2 (a) and (b) respectfully.

The open-circuit voltage (V_{OC}) of a DSSC corresponds to the potential difference between the Fermi level of the wide band gap semiconductor (TiO_2) under illumination

and the potential of the redox electrolyte equilibrium (as labelled in Figure 1.2 (b)). Thus alteration of the TiO_2 conduction band to higher potentials is required to enhance the V_{OC} (and minimise losses) of a DSSC.

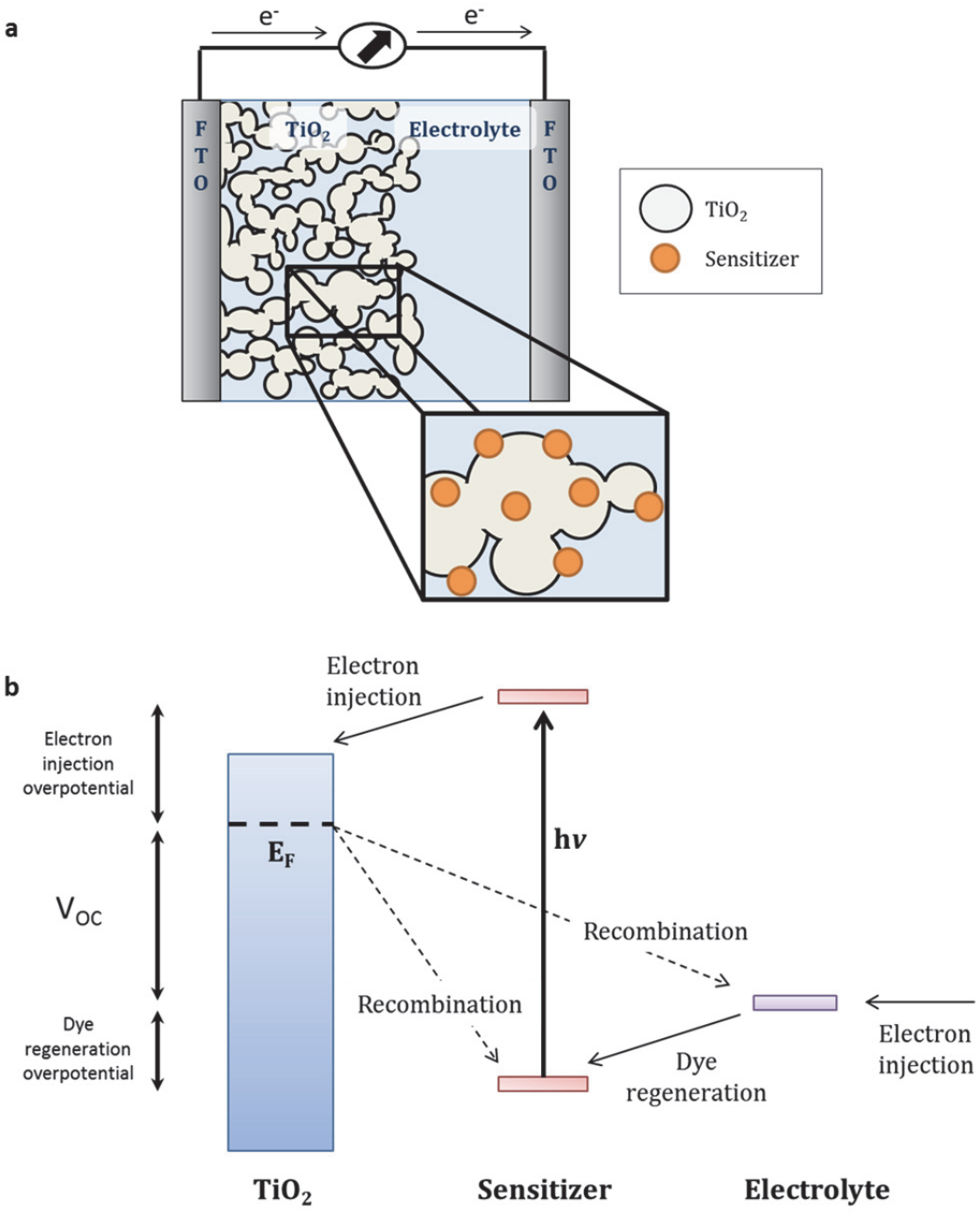

Figure 1.2. (a) Schematic of a DSSC architecture; photoanode, electrolyte and counter electrode. (b) Schematic of the relative energy levels and kinetic routes for electron transfer in a DSSC.

Since the introduction of DSSCs in 1991 with a power efficiency of ~ 7 %,[14] the maximum efficiency of research laboratory DSSC has risen to ~ 12.3 %.[26] In a recent feature article by H. Snaith, an estimate for the maximum attainable efficiency of DSSCs was set at 13.4 %.[27] This upper limit was projected using idealised parameters for light harvesting efficiency, cell fill factor and potential drop (voltage losses) utilizing the materials currently available today. Through a combination of electron transfer and hole regeneration improvements (e.g. reduction of disorder at interfaces, replacing iodide/triiodide redox couple) the paper anticipates that the efficiency limit for DSSCs could be further increased to reach 20 %.

1.3.2 Semiconductor Sensitized Solar Cells (SCSSC)

Semiconductor sensitized solar cells (SCSSC) are, in some respects, analogous to DSSCs. Architecturally, the only difference between SCSSCs and DSSCs is the replacement of the light harvesting dye molecules by a semiconductor sensitizer.

1.3.2.1 Semiconductor Sensitizers

1.3.2.1.1 Quantum Dots

Quantum dots (QDs) are semiconductor nanoparticles spatially confined in three dimensions. They are considered to be "zero dimensional" and are approximately spherical in shape with a typical diameter of 1–20nm.[28] QDs are typically composed of atoms from groups 11 and 17 (such as copper chloride, CuCl), 12 and 16 (such as cadmium sulfide, CdS and cadmium selenide, CdSe) or 13 and 15 (such as indium arsenide, InAs) of the periodic table. There have been several reviews on the properties and synthesis of QDs. [28-32]

Contrary to bulk semiconductors, QDs have size-tuneable mechanical, electrical and optical properties.[33] For example, upon the reduction of the QD diameter, the band gap of a nanocrystal increases.[34] Other size tuneable properties of QDs include the extinction coefficient and melting point.[35,36] Size-tuneable properties of low dimensional crystals (such as QDs) are due to the physical constraints of the particles rather than a difference in crystal structure (which remains consistent across all crystal sizes).[33,37] For any semiconductor, the exciton (an electron-hole pair) has an average distance between the charge carriers (i.e. the hole and electron) termed the Bohr radius.

For a bulk semiconductor, the crystal size is much greater than the exciton Bohr radius and an exciton will exist at its natural size limit. For a nanocrystal, however, as the particle size is reduced it will approach, and then become smaller than the Bohr radius (quantum confinement). Equation (1.1) defines the range over which size tuneable properties are observed where R is the radius, and l is the lattice spacing of the QD. Thus the electrons and holes are closer together than in the bulk crystal.

$$l \ll R \leq a_b \tag{1.1}$$

where a_b, the Bohr radius is:

$$a_b = \frac{4\pi\epsilon_0\hbar^2}{m_e e^2} \tag{1.2}$$

where ε_0 is the permittivity of free space, ħ is Planck's constant divided by 2π, m_e is the electronic mass and e is the electronic charge.

Given the proximity of the electron and hole, Coulombic interactions must be considered between the electron/hole pair and thus the charge carriers have a greater kinetic energy than in the bulk material. Brus *et al.*[30,38,39] demonstrated on the basis of the effective mass approximation that the size dependence change in band gap for cadmium chalcogenide quantum dots can be estimated by the following:

$$\Delta E \approx \frac{\hbar^2\pi^2}{2R^2}\left[\frac{1}{m_e^*}+\frac{1}{m_h^*}\right] - \frac{1.8e^2}{\varepsilon R} \tag{1.3}$$

The Coulombic component therefore shifts the first excited electronic state towards lower energies as R^{-1}. Conversely, the quantum localisation term shifts the excited state towards higher energies as R^{-2}. The net change in band gap is therefore dominated by the quantum localisation term and thus shifts to higher energies with decreasing QD size. This is experimentally observed as a blue shift in absorbance onset with decreasing QD size. It is of note that this estimation is not quantitatively accurate for experimental values and in particular, it is particularly inaccurate for the smallest QD sizes (< 4 nm).

Another factor which determines the size tuneable properties is the dispersity (ratio of surface to total atoms within QD) of QDs. The fraction of composite atoms present at the surface of a QD is >75 % for a <1nm diameter nanoparticle, whereas <0.5% of atoms are present at the surface of a >20nm diameter QD.[40] Thus, in the nanocrystal size range, surface atoms significantly influence the properties of the QD, introducing trap states in the QD band gap (see Section 1.3.2.1.5 for further details).

1.3.2.1.2 Quantum Dot Sensitized Solar Cells (QDSSC)

Electron injection from a semiconductor to TiO_2 was first demonstrated by Serpone *et al*. in 1984 using CdS sensitized TiO_2.[41] Since, driven by the development of DSSCs, there has been extensive research in the field of semiconductor sensitized solar cells primarily focused on QD sensitized solar cells (QDSSC).

The basic architecture of QDSSC is analogous to the DSSC, (Figure 1.2 (a)) whereby the photon harvesting dye molecules are replaced with QDs. Upon absorption of a photon an electron-hole pair is created in the QD which must be separated and extracted from the cell at opposite electrodes. The photoexcited electron in the QD conduction band is injected into the TiO_2 and subsequently diffuses through the TiO_2 network to the conductive glass substrate; the hole that resides in the QD valence band is removed by a reduced species in the redox couple that penetrates into the mesoporous morphology. The oxidised redox species is transported (diffuses) towards the counter electrode where upon the electrons re-enter the cell and thus the circuit is complete. Semiconductor QDs such as CdS,[42-44] CdSe,[45,46] PbS,[43,47] InP[48] and Bi_2S_3[43] have drawn particular attention as sensitizers for QDSSCs. Recently, copper zinc tin sulphur (CZTS) and other nanoparticles have been demonstrated in SSSC photovoltaics.[49,50]

1.3.2.1.3 Routes to Quantum Dot Sensitized Photoanodes

There are an extensive range of methodologies for preparing QDSSCs, demonstrating the versatility of the technology. The primary difference between the existing methodologies is the sensitization route. QD sensitization can generally be categorised into two fundamentally different routes; *ex situ* and *in situ*.

Ex situ routes attach pre-synthesised QDs to the wide band gap semiconductor surface. This has been achieved by both direct QD adsorption and linker assisted

adsorption. Linker assisted sensitization is achieved by a two-step process. Firstly the porous TiO_2 surface is coated with a bifunctional linker molecule such as 3-mercaptopropionic acid (3-MPA).[51] In the case of 3-MPA the carboxylic acid functional group adsorbs to the TiO_2 surface. After removal of excess linker molecule the electrode is introduced into the QD dispersion whereupon the thiol group of 3-MPA adsorbs to the QDs, thus tethering the absorber to the TiO_2 surface. Direct adsorption (DA) (without linker molecule) has also been achieved by submerging TiO_2 mesoporous films into a colloidal solution of QDs for several hours.[52,53] Due to the small driving force of DA the route is very sensitive to experimental conditions such as the solvent.[52]

There are two primary concerns with *ex situ* preparation routes. Firstly the reliance of the technique on QD diffusion into the porous TiO_2 network and hence the long times (days)[51] that are required for complete sensitization. Secondly, the introduction of a linker molecule has been shown to reduce the rate of electron transfer from QD to TiO_2 and hence enhances electron-hole recombination in the photoanode.[54] An alternative *ex situ* route to QD sensitization is through electrophoretic deposition (EPD) which has been shown to offer a reduced time for sensitization of the mesoporous surface.[55]

In situ routes to QD sensitzation combine QD synthesis and sensitization into one experimental step. Examples of *in situ* routes to sensitization include chemical bath deposition (CBD)[56] and successive ionic layer adsorption and reaction (SILAR)[57]. These routes typically lead to high TiO_2 surface coverage (relative to photoanodes prepared by *ex situ* routes) which can be beneficial to cell performance. However if the QDs are close-packed this can lead to higher internal recombination.[52] With respect to crystallinity and monodispersity, QDs in QDSSCs prepared pre-sensitization by *in situ* routes lag behind QDs prepared by *ex situ* routes.

1.3.2.1.4 Quantum Dots as Sensitizers: The Advantages

QDs offer a number of perceived advantages over dyes which provides motivation for their study. In particular, these advantages include higher absorbance,[36] (higher molar exctinction coefficients) as well as greater photostability relative to many organometallic and organic dyes.[58] Additionally, the larger, tunable band-gaps (as a consequence of quantum confinement) readily enable the tuning of the absorption across the visible spectrum to match the solar spectrum. Lead sulfide (PbS) is perhaps one of the most suitable sensitizers with respect to its bandgap which extends the

window for photon harvesting from the ultraviolet to infrared wavelengths. CdSe is certainly the most extensively investigated QD as a sensitizer, primarily due to the range of synthetic routes to this material.

Other advantages of QDs as sensitizers include the possibility of harvesting "multiple exciton generation/collection" (MEG/MEC) [59] and "hot carrier collection"[60]. A hot carrier refers to a photoexcited electron with energy greater than the conduction band minima. Typically, when a hot carrier is generated it will decay to the conduction band minima/valance band maxima releasing thermal energy to the system (Figure 1.3 (A)). A hot carrier can, however, produce further photoexcited electron/hole pairs if the hot carrier has sufficient kinetic energy (higher than the band gap). The excess energy that would otherwise be released as a phonon can instead generate additional charge carrier pairs; a process termed impact ionization (Figure 1.3 (B)). In particular, PbSe and PbS QDs colloids have shown (on average) the conversion of one photon (of energy greater than four times the band gap) to an average of two or three electrons.[61] More recently MEG has been demonstrated in PbS QDSSCs.[59]

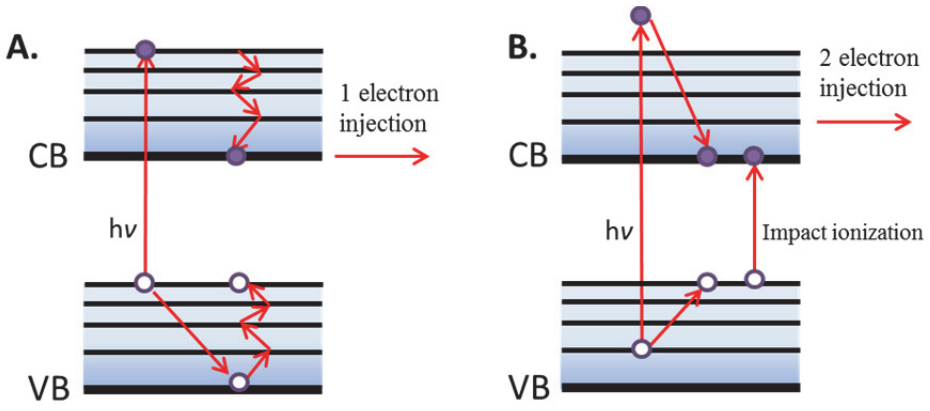

Figure 1.3. Schematic of excitation from valence band (VB) to conduction band (CB). (A) Post excitation the photoexcited electron decays by non-radiative relaxation to the conduction band minima. (B) A photoexcited electron decays *via* impact ionization to the conduction band minima generating a second electron/hole pair.

1.3.2.1.5 Quantum Dot Sensitizers: The Limitations

Despite the recent interest in QDSSC research, the maximum power efficiencies of such devices remains, to date (December 2012) (5.32 % [62]) lower than DSSC efficiencies

(12.3 % [26]). In a recent review by Mora-Sero and Bisquert three areas were highlighted that have, and could further contribute to enhanced QDSSC performance; the sensiziter, surface treatments (both QD and TiO_2) and the electron transport material.[63] With regards to the materials, this refers to the choice of wide band gap semiconductor, electrolyte, counter electrode, and transparent conductive electrode. Recent advances in these fields are discussed below.

With regards to the wide band gap semiconductor both the choice of material and morphology must be considered. Titanium dioxide (TiO_2) dominates the literature with regards to material choice primarily due to its relatively high chemical stability. On the other hand, longer electron lifetimes have been observed in zinc oxide which implies lower charge recombination and thus improved solar cell performance.[64] It can also be readily prepared by a vast range of synthetic routes in a range of morphologies. The surface morphology of the wide band gap material determines the QD adsorbance and charge transport. Nearly close packed layers of CdSe QDs have been observed adsorbed onto TiO_2 single crystals whereas, sensitization of a mesoporous (Degussa P25) TiO_2 surface has been estimated to give a fractional coverage of 0.14.[52] This is thought to be due to physical constraints of pore and QD size. With a view to a more accessible high surface area alternative TiO_2 and ZnO architectures have been developed (for both QD and dye sensitized solar cells) such as nanotubes,[65,66] nanowires[67-69] and inverse opal structures[70-72]. These structures have led to a slight improvement in cell performance.

The most common electrolyte utilized in high efficiency DSSCs is the iodide/triiodide redox couple which is highly corrosive towards QDs. Alternative redox couples have been demonstrated for QDSSCs with reasonable success in terms of cell performance. Examples include cobalt (Co^{2+}/Co^{3+})[45] and polysulfide (S^{2-}/S_n^{2-}) redox couples.[73] The success of Co^{2+}/Co^{3+} in QDSSCs has, however, been limited due to the poor diffusion of the cobalt ions within the porous photoanode, which restricts photocurrent. Conversely, polysulfide redox couples have demonstrated high photocurrents, however they are non-compatible with a platinum counter electrode.[74] Solid state hole conductors have also been considered as offering a solution to long-term stability issues of liquid electrolytes and cell sealing.[75] However, to date, solid state DSSC devices operate at lower efficiencies relative to liquid electrolyte based devices due to faster recombination at the electrolyte/dye interface.[76,77]

Surface treatments are employed to overcome various limitations of both QD and TiO_2 in QDSSCs. For example, a thin amorphous TiO_2 layer employed on top of the QDs was shown to prevent corrosion in iodide/triiodide electrolyte enhancing cell performance (relative to cell operation in polysulfide electrolyte).[78] Alongside protection from corrosion, surface treatments can also assist in the prevention of undesirable electron transfer pathways such as the recombination mechanisms detailed in Figure 1.4. Examples of such blocking layers include the use of zinc sulfide[79,80] (shown to enhanced IPCE 3- fold) and silicon dioxide[81] (shown to almost double the IPCE). If a semiconductor shell is utilized with a conduction band edge higher (relative to the QD) than the QD, the layer will act as a barrier to electron transfer from the QD to electrolyte. Given the often low QD surface coverage, a significantly large area of TiO_2 is in contact with the electrolyte solution and hence recombination mechanisms can dominate. The surface layer increases the physical separation between TiO_2 and electrolyte and thus increases the resistance to one recombination mechanism.

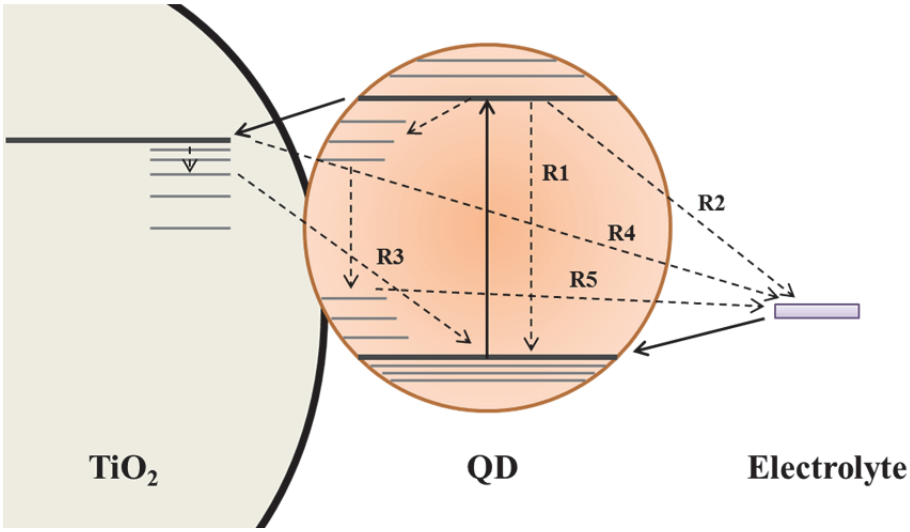

Figure 1.4. Schematic of the possible electron transfer mechanisms for a QDSSC photoanode. Favourable mechanistic routes are represented with solid arrows; routes contributing to unfavourable charge-recombination are represented with dashed arrows. Recombination routes are labelled. R1 is the direct recombination of the photoexcited electron and hole in the QD. R2, R4 and R5 are the unfavourable recombination routes between electron and electrolyte; QD, TiO_2 and QD valance band trap states respectively. R3 is the indirect recombination via trap states in the QD. The figure is adapted from reference 63.

The limitations and recent developments of QDs as photon harvesters in QDSSCs have been recently reviewed by Chang *et al*.[82] From this, an overview of the relevant advances and approaches in the field are now briefly discussed.

Co-sensitization (sensitization with two or more photon absorbers) has been highlighted as a possible route to enhanced QDSSC efficiencies. Independently, CdS and CdSe absorb across different regions of the solar spectrum; CdS is limited to <550nm whereas the smaller band gap of CdSe extends absorbance to <720nm. From the literature, the conduction band of CdS is positioned at a relatively higher energy than CdSe.[15] However, when the two materials are brought into contact electrons equilibrate and there is consequently a redistribution of electrons such that the conduction band of CdS is brought lower than CdSe.[83] For a structure composed of TiO_2/CdS/CdSe the conduction bands are therefore aligned such that CdSe has the highest, TiO_2 has the lowest and CdS is between the other two. This is known as a "cascade" structure as a photoexcited electron in CdSe is able to "cascade" (inject) into the CdS conduction band and subsequently into the TiO_2. In a recent demonstration of this effect a comparative study between TiO_2/CdS/CdSe v TiO_2/CdSe/CdS revealed a 3- fold increase in IPCE for TiO_2/CdS/CdSe.

An alternative route to co-sensitization is the implementation of core/shell QDs in sensitized solar cells. Similarly to co-sensitization, core/shell QDs combine the advantages of two absorbing materials for photon harvesting. Two types of core/shell QDs exist; Type-I and Type-II. As illustrated in Figure 1.5 (a) and (b), type-I structured QDs are structured such that either the core/shell material has a larger band gap relative to the shell/core. The relative band edges are positioned such that the smaller band gap conduction band and valance band are lower and higher respectively. The electrons/holes are therefore mostly located at the surface of the QD in the shell, easing the extraction of electrons relative to core only QDs. Highly efficient QDSSCs (5.32 % under 1 sun illumination) have been achieved using the type-I CdS/CdSe core/shell QDs demonstrating the success of the "cascade" approach.[62] Conversely, type-II QD form a staggered alignment whereby either the conduction and valence bands are (both) higher or lower than the core bands. This facilitates the separation of photoexcited charge carriers (electrons/holes) into the core and shell.[84] In the first example of a type-II QDSSC, ZnSe/CdS core/shell QDs (lower conduction and valence bands in the shell relative to the core) were realised.[85]

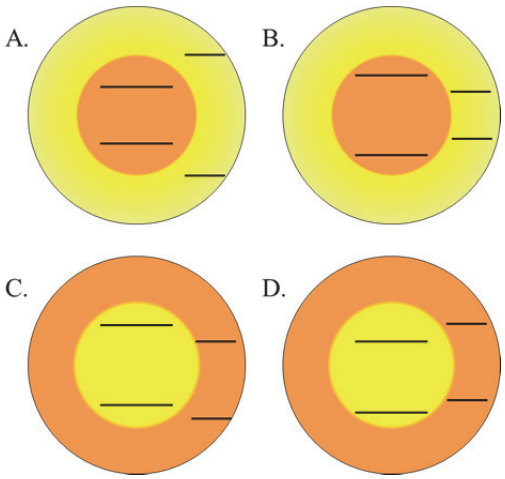

Figure 1.5. Schematic of four types of core/shell QDs. (A) and (B) are Type I; (C) and (D) are Type II.

A further example of co-sensitization is the introduction of both dye molecules and QDs to QDSSCs revealing enhanced device current density.[86] A thin layer of dye molecules are attached at the interface between the QD and electrolyte such that both the QD and dye are able to photoinject into the TiO_2. In addition to the enhanced photoanode absorption of a co-sensitized photoanode, the dye has been shown to regenerate photoexcited QDs thus increasing the physical separation and minimising QD charge recombination losses.

1.3.2.2 Molybdenum Disulfide

Group IV transition metal dichalcogenides (TMDs), MX_2 where M = Mo, W and X = S, Se and Te are semiconducting layered compounds which have been widely studied for over 50 years.[87] Structurally, TMDs are composed of covalently bound X – M – X planes which are held together by weak Van der Waal interactions, as depicted in Figure 1.6. This structure readily enables the isolation of atomically thin monolayers of TMDs via cleavage along these relatively weak planes. Similar to graphene, individual layers of TMDs have been isolated by both the "Scotch tape method" (micromechanical cleavage of bulk crystals)[88] and liquid phase exfoliation.[89-91] Direct growth of a few layers thick MoS_2 sheets was recently achieved via chemical vapour deposition (CVD),[92] thermolysis of thiosalts [93] and sulfurization of molybdenum film.[94]

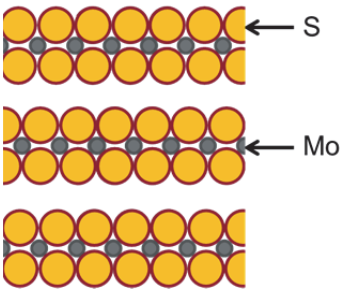

Figure 1.6. Schematic representing the crystal structure of layered TMDs such as MoS_2. Molybdenum atoms are shown in grey; sulphur in yellow.

Atomically thin, two-dimensional (2-D) sheets of TMDs exhibit intriguing physical properties, absent in the bulk form due to quantum confinement effects and changes in symmetry. Recently, the observation of photoluminescence in monolayer MoS_2 has attracted particular interest.[95,96] The development of photoluminescence with reduced dimension has been attributed to the evolution of the material from an indirect semiconductor with a band gap of 1.29 eV in bulk form to a direct semiconductor with a band gap of 1.90 eV when a monolayer sheet.[96] Recent studies have also shown that single layer MoS_2 exhibits excellent field effect transistor characteristics with high electron mobility, on/off ratio, and minimal sub-threshold swing, triggering a number of subsequent studies on its use in electronic devices. [97-99] Unusual mechanical stability of single layer MoS_2 against bending and stretching has also been highlighted. [99,100] As a direct semiconductor with unusual properties associated with the 2-D structure MoS_2 nanosheets have been receiving increasing attention as a new opto-electronic material.[101]

1.3.2.2.1 Molybdenum Disulfide Photoanodes

Bulk single crystals of MoS_2 have been studied as photoanodes for photoelectrochemical (PEC) cells since the 1970s.[102-105] Due to both its suitable band gap for solar spectrum absorption and excellent photocatalytic stability against photocorrosion,[106,107] MoS_2 has been considered as an ideal material for photocatalysis and PEC solar cells.[107-109] Early work demonstrated a promising solar energy conversion efficiency of approximately 6 %.[105] While previous studies focused mainly on bulk single crystals and sputter deposited thin films, the PEC properties of emerging MoS_2 2-D crystals remain elusive. The larger band gap of 2-D MoS_2 in contrast to that of the bulk implies substantially different orbital energy levels, which determine the

charge transfer between the electrolyte, electrode and adjacent semiconducting surfaces.

1.3.2.2.2 Molybdenum Disulfide Sensitized Solar Cell

In photocatalysis, MoS_2 nanocrystals grown on wider band gap semiconductors such as TiO_2 have been show to serve as an effective sensitizer. Synergistic effects on photocatalytic activities such as enhanced production of hydrogen[110] and degradation of organic molecules have been realised under visible light.[111-113] Analogous to other SSSCs (Chapter 1.3), in MoS_2 sensitized TiO_2, photoexcited electrons in MoS_2 must inject into the TiO_2. This requires the conduction band minimum of MoS_2 (or QDs) to lie above that of TiO_2. In previous studies,[114,115] such band alignment was achieved with MoS_2 nanoparticles where, as a consequence of quantum confinement, the band gap is significantly increased and the conduction minimum is increased (relative to that of the bulk). It is expected that similar energy level changes are achieved with 2-D sheets of MoS_2. Preliminary studies on both MoS_2 and WS_2 have suggested that electron injection is indeed possible for mono/few-layer MoS_2-TiO_2 systems.[116,117]

1.3.2.3 Alternative Semiconductor Sensitizers

In an endeavour to reach higher SSSC efficiencies, recent significant advances in the field have included investigations of alternative materials for sensitizers. For example, copper indium sulfide ($CuInS_2$) sensitized TiO_2 where $CuInS_2$ is both the sensitizer and hole transporting material.[118] Other examples of alternative semiconductors considered appropriate for solar harvesting include In_2S_3 and Sb_2S_3.[119-121] In particular these materials have been explored for extremely thin absorber cells – an alternative cell architecture to SSCs whereby an extremely thin absorber layer (up to 10nm) is sandwiched between penetrating electron and hole conductors. ETA solar cells have achieved power efficiencies of up to 6.3 %. More recently, a "meso-superstructured solar cell" has been demonstrated with 10.9 % power efficiency whereby the TiO_2 is replaced with a similarly porous, but insulting alumina layer.[122] The high device performance is accredited to the sensitizing perovskite layer which both harvests incident photons and transports the electron, thus removing any loss mechanisms due to traps in the TiO_2.

1.4 Thesis Outline

Looking towards the future of nanomaterials for solar cell application, expansion of the catalogue of materials utilized is crucial for the successful development of QDSSCs. Through a combination of alternative QD sizes, types, chemical composition, surface passivation, alongside enhanced surface sensitization with monodisperse QDs, development of an optimized electrolyte will lead to enhanced device performance.

The work prepared in this thesis was conducted with a view to expansion of scientific understanding in this vast and expanding field. The focus of each chapter addresses a separate topic within the semiconductor sensitized solar cell field. The first chapter investigates the influence of the QD purification procedure determining the implications this has on QD adsorbance and the performance of sensitized photoanodes. An investigation into the influence of polysulfide electrolyte on CdSe QDs is given in the second chapter. In the final experimental chapter two dimensional sheets of molybdenum disulphide are realised as an alternative sensitizer in a SSSC. Characterisation of the MoS_2 sheets and MoS_2-TiO_2 structures reveal favourable band gap alignment enabling MoS_2 sensitized TiO_2.

1.5 References

(1) Union, E. *Energy Roadmap 2050* Belgium, 2012.

(2) Change, I. P. o. C.; Cambridge University Press: 2012.

(3) Kamat, P. V. *Journal of Physical Chemistry C* **2007**, *111*, 2834.

(4) Barnham, K. W. J.; Mazzer, M.; Clive, B. *Nat. Mater.* **2006**, *5*, 161.

(5) Arvizu, D. E. *IPCC Scoping Meeting on Renewable Energy Sources* **2008**, 33.

(6) Lanzani, G. *The Photophysics behind Photovoltaics and Photonics*; Wiley-VCH: Weinheim, Germany, 2012.

(7) Becquerel, A. E. *Comptes Rendus de L´Academie des Sciences* **1839**, *9*, 145.

(8) Shockley, W., Queisser, H. J., *J. Appl. Phys.* **1961**, *32*, 510.

(9) Green, M. A. *Prog. Photovoltaics* **2001**, *9*, 123.

(10) Green, M. A. *Prog. Photovoltaics* **2009**, *17*, 183.

(11) Green, M. A.; Emery, K.; Hishikawa, Y.; Warta, W.; Dunlop, E. D. *Prog. Photovoltaics* **2012**, *20*, 12.

(12) Gunes, S.; Neugebauer, H.; Sariciftci, N. S. *Chem. Rev.* **2007**, *107*, 1324.

(13) Kamat, P. V.; Tvrdy, K.; Baker, D. R.; Radich, J. G. *Chem. Rev.* **2010**, *110*, 6664.

(14) Oregan, B.; Gratzel, M. *Nature* **1991**, *353*, 737.

(15) Gratzel, M. *Nature* **2001**, *414*, 338.

(16) Walter, M. G.; Warren, E. L.; McKone, J. R.; Boettcher, S. W.; Mi, Q. X.; Santori, E. A.; Lewis, N. S. *Chem. Rev.* **2010**, *110*, 6446.

(17) Gust, D.; Moore, T. A.; Moore, A. L. *Accounts Chem. Res.* **2009**, *42*, 1890.

(18) Hagfeldt, A.; Gratzel, M. *Accounts Chem. Res.* **2000**, *33*, 269.

(19) Gratzel, M. *J. Photochem. Photobiol. C-Photochem. Rev.* **2003**, *4*, 145.

(20) Gratzel, M. *J. Photochem. Photobiol. A-Chem.* **2004**, *164*, 3.

(21) Gratzel, M. *Inorg. Chem.* **2005**, *44*, 6841.

(22) Gratzel, M. *Accounts Chem. Res.* **2009**, *42*, 1788.

(23) Hagfeldt, A.; Boschloo, G.; Sun, L. C.; Kloo, L.; Pettersson, H. *Chem. Rev.* **2010**, *110*, 6595.

(24) Robertson, N. *Angew. Chem.-Int. Edit.* **2006**, *45*, 2338.

(25) Listorti, A.; O'Regan, B.; Durrant, J. R. *Chemistry of Materials* **2011**, *23*, 3381.

(26) Yella, A.; Lee, H. W.; Tsao, H. N.; Yi, C. Y.; Chandiran, A. K.; Nazeeruddin, M. K.; Diau, E. W. G.; Yeh, C. Y.; Zakeeruddin, S. M.; Gratzel, M. *Science* **2011**, *334*, 629.

(27) Snaith, H. J. *Adv. Funct. Mater.* **2010**, *20*, 13.

(28) Trindade, T.; O'Brien, P.; Pickett, N. L. *Chemistry of Materials* **2001**, *13*, 3843.

(29) Brus, L. *J. Phys. Chem.* **1986**, *90*, 2555.

(30) Bawendi, M. G.; Steigerwald, M. L.; Brus, L. E. *Annu. Rev. Phys. Chem.* **1990**, *41*, 477.

(31) Weller, H. *Angew. Chem.-Int. Edit. Engl.* **1993**, *32*, 41.

(32) Reimann, S. M.; Manninen, M. *Rev. Mod. Phys.* **2002**, *74*, 1283.

(33) Alivisatos, A. P. *Science* **1996**, *271*, 933.

(34) Norris, D. J.; Bawendi, M. G. *Phys. Rev. B* **1996**, *53*, 16338.

(35) Goldstein, A. N.; Echer, C. M.; Alivisatos, A. P. *Science* **1992**, *256*, 1425.

(36) Yu, W. W.; Qu, L. H.; Guo, W. Z.; Peng, X. G. *Chemistry of Materials* **2003**, *15*, 2854.

(37) Alivisatos, A. P. *J. Phys. Chem.* **1996**, *100*, 13226.

(38) Brus, L. E. *J. Chem. Phys.* **1983**, *79*, 5566.

(39) Brus, L. E. *J. Chem. Phys.* **1984**, *80*, 4403.

(40) Murray, C. B.; Kagan, C. R.; Bawendi, M. G. *Annu. Rev. Mater. Sci.* **2000**, *30*, 545.

(41) Serpone, N.; Borgarello, E.; Gratzel, M. *Journal of the Chemical Society-Chemical Communications* **1984**, 342.

(42) Gerischer, H.; Lubke, M. *J. Electroanal. Chem.* **1986**, *204*, 225.

(43) Vogel, R.; Hoyer, P.; Weller, H. *J. Phys. Chem.* **1994**, *98*, 3183.

(44) Vogel, R.; Pohl, K.; Weller, H. *Chem. Phys. Lett.* **1990**, *174*, 241.

(45) Lee, H. J.; Yum, J. H.; Leventis, H. C.; Zakeeruddin, S. M.; Haque, S. A.; Chen, P.; Seok, S. I.; Grazel, M.; Nazeeruddin, M. K. *J. Phys. Chem. C* **2008**, *112*, 11600.

(46) Liu, D.; Kamat, P. V. *J. Phys. Chem.* **1993**, *97*, 10769.

(47) Lee, H.; Leventis, H. C.; Moon, S. J.; Chen, P.; Ito, S.; Haque, S. A.; Torres, T.; Nuesch, F.; Geiger, T.; Zakeeruddin, S. M.; Gratzel, M.; Nazeeruddin, M. K. *Adv. Funct. Mater.* **2009**, *19*, 2735.

(48) Zaban, A.; Micic, O. I.; Gregg, B. A.; Nozik, A. J. *Langmuir* **1998**, *14*, 3153.

(49) Guo, Q. J.; Hillhouse, H. W.; Agrawal, R. *Journal of the American Chemical Society* **2009**, *131*, 11672.

(50) Steinhagen, C.; Panthani, M. G.; Akhavan, V.; Goodfellow, B.; Koo, B.; Korgel, B. A. *Journal of the American Chemical Society* **2009**, *131*, 12554.

(51) Robel, I.; Subramanian, V.; Kuno, M.; Kamat, P. V. *Journal of the American Chemical Society* **2006**, *128*, 2385.

(52) Guijarro, N.; Lana-Villarreal, T.; Mora-Sero, I.; Bisquert, J.; Gomez, R. *Journal of Physical Chemistry C* **2009**, *113*, 4208.

(53) Frindt, R. F. *Physical Review* **1965**, *140*, 536.

(54) Pernik, D. R.; Tvrdy, K.; Radich, J. G.; Kamat, P. V. *Journal of Physical Chemistry C* **2011**, *115*, 13511.

(55) Salant, A.; Shalom, M.; Hod, I.; Faust, A.; Zaban, A.; Banin, U. *Acs Nano* **2010**, *4*, 5962.

(56) Gorer, S.; Hodes, G. *J. Phys. Chem.* **1994**, *98*, 5338.

(57) Lee, H.; Wang, M. K.; Chen, P.; Gamelin, D. R.; Zakeeruddin, S. M.; Gratzel, M.; Nazeeruddin, M. K. *Nano Lett.* **2009**, *9*, 4221.

(58) Hodes, G. *Journal of Physical Chemistry C* **2008**, *112*, 17778.

(59) Sambur, J. B.; Novet, T.; Parkinson, B. A. *Science* **2010**, *330*, 63.

(60) Tisdale, W. A.; Williams, K. J.; Timp, B. A.; Norris, D. J.; Aydil, E. S.; Zhu, X. Y. *Science* **2010**, *328*, 1543.

(61) Ellingson, R. J.; Beard, M. C.; Johnson, J. C.; Yu, P. R.; Micic, O. I.; Nozik, A. J.; Shabaev, A.; Efros, A. L. *Nano Lett.* **2005**, *5*, 865.

(62) Pan, Z. X.; Zhang, H.; Cheng, K.; Hou, Y. M.; Hua, J. L.; Zhong, X. H. *Acs Nano* **2012**, *6*, 3982.

(63) Mora-Sero, I.; Bisquert, J. *J. Phys. Chem. Lett.* **2010**, *1*, 3046.

(64) Gonzalez-Valls, I.; Lira-Cantu, M. *Energy Environ. Sci.* **2009**, *2*, 19.

(65) Kongkanand, A.; Tvrdy, K.; Takechi, K.; Kuno, M.; Kamat, P. V. *Journal of the American Chemical Society* **2008**, *130*, 4007.

(66) Baker, D. R.; Kamat, P. V. *Adv. Funct. Mater.* **2009**, *19*, 805.

(67) Law, M.; Greene, L. E.; Johnson, J. C.; Saykally, R.; Yang, P. D. *Nat. Mater.* **2005**, *4*, 455.

(68) Leschkies, K. S.; Divakar, R.; Basu, J.; Enache-Pommer, E.; Boercker, J. E.; Carter, C. B.; Kortshagen, U. R.; Norris, D. J.; Aydil, E. S. *Nano Lett.* **2007**, *7*, 1793.

(69) Bang, J. H.; Kamat, P. V. *Adv. Funct. Mater.* **2010**, *20*, 1970.

(70) Diguna, L. J.; Shen, Q.; Kobayashi, J.; Toyoda, T. *Appl. Phys. Lett.* **2007**, *91*, 3.

(71) Cheng, C. W.; Karuturi, S. K.; Liu, L. J.; Liu, J. P.; Li, H. X.; Su, L. T.; Tok, A. I. Y.; Fan, H. J. *Small* **2012**, *8*, 37.

(72) Toyoda, T.; Shen, Q. *J. Phys. Chem. Lett.* **2012**, *3*, 1885.

(73) Chakrapani, V.; Baker, D.; Kamat, P. V. *Journal of the American Chemical Society* **2011**, *133*, 9607.

(74) Hodes, G.; Manassen, J.; Cahen, D. *J. Electrochem. Soc.* **1980**, *127*, 544.

(75) Brennan, T. P.; Ardalan, P.; Lee, H. B. R.; Bakke, J. R.; Ding, I. K.; McGehee, M. D.; Bent, S. F. *Advanced Energy Materials* **2011**, *1*, 1169.

(76) Snaith, H. J.; Schmidt-Mende, L. *Adv. Mater.* **2007**, *19*.

(77) Snaith, H. J.; Humphry-Baker, R.; Chen, P.; Cesar, I.; Zakeeruddin, S. M.; Graetzel, M. *Nanotechnology* **2008**, *19*.

(78) Shalom, M.; Dor, S.; Ruhle, S.; Grinis, L.; Zaban, A. *Journal of Physical Chemistry C* **2009**, *113*, 3895.

(79) Shen, Q.; Kobayashi, J.; Diguna, L. J.; Toyoda, T. *J. Appl. Phys.* **2008**, *103*.

(80) Hachiya, S.; Shen, Q.; Toyoda, T. *J. Appl. Phys.* **2012**, *111*.

(81) Liu, Z. F.; Miyauchi, M.; Uemura, Y.; Cui, Y.; Hara, K.; Zhao, Z. G.; Sunahara, K.; Furube, A. *Appl. Phys. Lett.* **2010**, *96*.

(82) Yang, Z. S.; Chen, C. Y.; Roy, P.; Chang, H. T. *Chem. Commun.* **2011**, *47*, 9561.

(83) Lee, Y. L.; Huang, B. M.; Chien, H. T. *Chemistry of Materials* **2008**, *20*, 6903.

(84) Lo, S. S.; Mirkovic, T.; Chuang, C. H.; Burda, C.; Scholes, G. D. *Adv. Mater.* **2011**, *23*, 180.

(85) Ning, Z. J.; Tian, H. N.; Yuan, C. Z.; Fu, Y.; Qin, H. Y.; Sun, L. C.; Agren, H. *Chem. Commun.* **2011**, *47*, 1536.

(86) Leventis, H. C.; Haque, S. A. *Energy Environ. Sci.* **2009**, *2*, 1176.

(87) WIlson, J. A.; Yoffe, A. D. *Advances in Physics* **1969**, *18*, 193.

(88) Novoselov, K. S.; Jiang, D.; Schedin, F.; Booth, T. J.; Khotkevich, V. V.; Morozov, S. V.; Geim, A. K. *Proc. Natl. Acad. Sci. U. S. A.* **2005**, *102*, 10451.

(89) Matte, H.; Gomathi, A.; Manna, A. K.; Late, D. J.; Datta, R.; Pati, S. K.; Rao, C. N. R. *Angew. Chem.-Int. Edit.* **2010**, *49*, 4059.

(90) Eda, G.; Yamaguchi, H.; Voiry, D.; Fujita, T.; Chen, M. W.; Chhowalla, M. *Nano Lett.* **2011**, *11*, 5111.

(91) Coleman, J. N.; Lotya, M.; O'Neill, A.; Bergin, S. D.; King, P. J.; Khan, U.; Young, K.; Gaucher, A.; De, S.; Smith, R. J.; Shvets, I. V.; Arora, S. K.; Stanton, G.; Kim, H. Y.; Lee, K.; Kim, G. T.; Duesberg, G. S.; Hallam, T.; Boland, J. J.; Wang, J. J.; Donegan, J. F.; Grunlan, J. C.; Moriarty, G.; Shmeliov, A.; Nicholls, R. J.; Perkins, J. M.; Grieveson, E. M.; Theuwissen, K.; McComb, D. W.; Nellist, P. D.; Nicolosi, V. *Science* **2011**, *331*, 568.

(92) Lee, Y. H.; Zhang, X. Q.; Zhang, W. J.; Chang, M. T.; Lin, C. T.; Chang, K. D.; Yu, Y. C.; Wang, J. T. W.; Chang, C. S.; Li, L. J.; Lin, T. W. *Adv. Mater.* **2012**, *24*, 2320.

(93) Liu, K. K.; Zhang, W. J.; Lee, Y. H.; Lin, Y. C.; Chang, M. T.; Su, C.; Chang, C. S.; Li, H.; Shi, Y. M.; Zhang, H.; Lai, C. S.; Li, L. J. *Nano Lett.* **2012**, *12*, 1538.

(94) Zhan, Y. J.; Liu, Z.; Najmaei, S.; Ajayan, P. M.; Lou, J. *Small* **2012**, *8*, 966.

(95) Splendiani, A.; Sun, L.; Zhang, Y. B.; Li, T. S.; Kim, J.; Chim, C. Y.; Galli, G.; Wang, F. *Nano Lett.* **2010**, *10*, 1271.

(96) Mak, K. F.; Lee, C.; Hone, J.; Shan, J.; Heinz, T. F. *Phys. Rev. Lett.* **2010**, *105*, 4.

(97) Radisavljevic, B.; Radenovic, A.; Brivio, J.; Giacometti, V.; Kis, A. *Nature Nanotechnology* **2011**, *6*, 147.

(98) Lee, H. S.; Min, S. W.; Chang, Y. G.; Park, M. K.; Nam, T.; Kim, H.; Kim, J. H.; Ryu, S.; Im, S. *Nano Lett.* **2012**, *12*, 3695.

(99) Pu, J.; Yomogida, Y.; Liu, K.; Li, L.; Iwasa, Y.; Takenobu, T. *Nano Lett.* **2012**, *12*, 4013.

(100) Bertolazzi, S.; Brivio, J.; Kis, A. *Acs Nano* **2011**, *5*, 9703.

(101) Yin, Z. Y.; Li, H.; Jiang, L.; Shi, Y. M.; Sun, Y. H.; Lu, G.; Zhang, Q.; Chen, X. D.; Zhang, H. *Acs Nano* **2012**, *6*, 74.

(102) Kam, K. K.; Parkinson, B. A. *J. Phys. Chem.* **1982**, *86*, 463.

(103) Kline, G.; Kam, K. K.; Ziegler, R.; Parkinson, B. A. *Solar Energy Materials* **1982**, *6*, 337.

(104) Tributsch, H. *Faraday Discussions* **1980**, *70*, 189.

(105) Djemal, G.; Muller, N.; Lachish, U.; Cahen, D. *Solar Energy Materials* **1981**, *5*, 403.

(106) Tributsch, H. *Solar Energy Materials* **1979**, *1*, 257.

(107) Kline, G.; Kam, K.; Canfield, D.; Parkinson, B. A. *Solar Energy Materials* **1981**, *4*, 301.

(108) Tributsch, H.; Bennett, J. C. *J. Electroanal. Chem.* **1977**, *81*, 97.

(109) Tributsch, H. *Berichte Der Bunsen-Gesellschaft-Physical Chemistry Chemical Physics* **1977**, *81*, 361.

(110) Kanda, S.; Akita, T.; Fujishima, M.; Tada, H. *Journal of Colloid and Interface Science* **2011**, *354*, 607.

(111) Tacchini, I.; Terrado, E.; Anson, A.; Martinez, M. T. *Micro & Nano Letters* **2011**, *6*, 932.

(112) Hu, K. H.; Hu, X. G.; Xu, Y. F.; Sun, J. D. *J. Mater. Sci.* **2010**, *45*, 2640.

(113) Ho, W. K.; Yu, J. C.; Lin, J.; Yu, J. G.; Li, P. S. *Langmuir* **2004**, *20*, 5865.

(114) Thurston, T. R.; Wilcoxon, J. P. *Journal of Physical Chemistry B* **1999**, *103*, 11.

(115) Wilcoxon, J. P.; Newcomer, P. P.; Samara, G. A. *J. Appl. Phys.* **1997**, *81*, 7934.

(116) Xiang, Q. J.; Yu, J. G.; Jaroniec, M. *Journal of the American Chemical Society* **2012**, *134*, 6575.

(117) Thomalla, M.; Tributsch, H. *Journal of Physical Chemistry B* **2006**, *110*, 12167.

(118) Grasso, C.; Nanu, M.; Goossens, A.; Burgelman, M. *Thin Solid Films* **2005**, *480*, 87.

(119) Moon, S. J.; Itzhaik, Y.; Yum, J. H.; Zakeeruddin, S. M.; Hodes, G.; Gratzel, M. *J. Phys. Chem. Lett.* **2010**, *1*, 1524.

(120) Itzhaik, Y.; Niitsoo, O.; Page, M.; Hodes, G. *Journal of Physical Chemistry C* **2009**, *113*, 4254.

(121) Tsujimoto, K.; Nguyen, D. C.; Ito, S.; Nishino, H.; Matsuyoshi, H.; Konno, A.; Kumara, G. R. A.; Tennakone, K. *Journal of Physical Chemistry C* **2012**, *116*, 13465.

(122) Lee, M. M., Teuscher, J., Miyasaka, T., Murakami, T. N., Snaith. H. J., *Science* **2012**.

Chapter 2. Fabrication, Instrumentation and Characterisation

The overarching theme of the research reported in this thesis is the preparation and characterisation of photoanodes for utilization in sensitized solar cells. The first two sections here detail the sensitizers and sensitizer substrates used throughout this work. The following section describes the characterisation techniques, instrumentation and materials used in the work, providing specific details where necessary of the sensitizer and sensitizer substrate materials. Some areas detailed in this chapter will be simply introduced and, in some cases are discussed in greater detail in the subsequent results chapters.

2.1 The Sensitizers

Two different photoactive materials were used as sensitizers; cadmium selenide (CdSe) quantum dots (QD) and molybdenum disulfide (MoS_2), the synthesis and properties of both are detailed in this section.

2.1.1 Cadmium Selenide Quantum Dots

There are many established methodologies for the synthesis of quantum dots (QDs), for example, synthesis in a structured medium (e.g. polymers,[1-4] micelles,[5-7] or zeolites[8]), arrested synthesis in solution,[9] chemical bath deposition[10] (CBD), successive ionic layer adsorption and reaction (SILAR)[11] and arrested precipitation, known as "hot injection". Alternative "flow-based" (e.g. microfluidic) synthetic routes have also been investigated and offer a more industrially appropriate scalable, controlled and reproducible synthesis to QDs.[12] The methodologies for the synthesis of QDs have been reviewed in the literature.[13]

It is essential for many of the applications of QDs that the synthesis prepares highly pure and monodisperse QDs. Monodispersity refers to identical and indistinguishable chemical species. However, in applications to experimentally prepared QDs a more appropriate definition of "monodisperse" is "narrow" size distribution, typically where the standard deviation of the colloidal diameter, $\sigma \leq 5$ % is

satisfied.[13-15] The shape, chemical and crystalline structure and surface chemistry are also consistent in a monodisperse suspension of a colloid.

2.1.1.1 Hot Injection

"Hot injection" is the synthetic technique used for the preparation of CdSe quantum dots in this thesis. The technique was pioneered in the preparation of "nearly monodisperse" CdSe, CdS and CdTe QDs by Murray *et al.* in 1993.[14] The size distribution of the synthesised QDs is controlled by temperature. Relative to the other synthetic routes, hot injection yields the highest quality (most monodisperse) particles.

In brief, hot injection is the rapid injection of molecular precursors into hot solvent under vigorous stirring. For the preparation of CdSe nanoparticles, the synthesis commences with the rapid injection of the organometallic precursors tri-*n*-octylphosphine selenide (TOPSe) and dimethylcadmium ($CdMe_2$) into a hot (250 – 300 ˚C) flask of the coordinating, high boiling point solvent tri-*n*-octylphosphine oxide (TOPO) under vigorous stirring. Upon injection of room temperature precursors into the reaction solution, the temperature of the flask is reduced to ~180 ˚C. A colour change to yellow/ orange is observed due to the nucleation and growth of QDs. The reaction is re-heated and the temperature increased to 230 – 260 ˚C. Once the required QD size is attained, (dependent on the growth time) the reaction is quenched in room temperature toluene. The nanocrystals produced by this technique are size tuneable across the range 1.2 – 11.5 nm diameter. The advantages of this technique include the high purity and the monodispersity of the synthesised QDs.

There are, however, limitations of the "hot injection" technique, as reported by Murray *et al.*[14] For example, the technique requires the use of the highly toxic, pyroforic, air sensitive and expensive reagent dimethylcadmium ($CdMe_2$). Research towards a "greener" synthesis involving a less harmful cadmium source was therefore undertaken. Replacements include cadmium carbonate,[16] cadmium oxide[16-19] and cadmium acetate.[16,20] It was found that addition of the reagents TOPO-HDA-TOP (HDA, 1-hexadecylamine; TOP, tri-*n*-octylphosphine) to the "greener" reaction synthesis leads to the synthesis of CdSe QDs with up to 85% room temperature photoluminescence quantum efficiency.[18,21]

The work presented here follows the synthesis of CdSe published by Talapin *et al.*[22] using cadmium acetate ($CdAc_2$) as the cadmium source and incorporating TDPA (*1*-

tetradecylphosphonoic acid) into the hot, co-ordinating solvent solution. The synthesis requires a mixture of TOPO-HDA-TOP-TDPA, which acts as a stabilizing mixture, slowing QD growth. An excess of the selenium precursor is also important for the reaction, enabling controlled growth and narrow particle size distribution. TDPA is thought to enhance size dispersion particularly toward the later stages of the colloidal growth.[19] It is postulated that the TDPA forms a relatively stable (1:1 stoichiometry) complex with the Cd as well as behaving as a monomer during the Ostwald ripening (once free $Cd(Ac)_2$ has been consumed).

2.1.1.2 Theory of the Hot Injection

The mechanism for the preparation of monodisperse colloidal dispersions was first described by Le Mer and Dinegar in 1950.[23] Such syntheses require a two-step precipitation reaction: rapid nucleation, followed by arrested nucleation and growth of the nuclei. *Monodisperse* colloidal growth is determined by the balance between the rates of nucleation and the rate of growth of crystallites. The ratio of these two rates determines both the size and concentration of crystallites within a colloidal dispersion.

The hot injection synthesis achieves monodispersity through the combination of temperature control (control of the rates of nucleation and particle growth) and the presence of coordinating solvents and surfactants.[14] Fast nucleation of the crystallites by the use of the rapid reagent injection enhances monodispersity. Upon injection nucleation of the QDs is initiated resulting in a reduction in the concentration of precursors. The precursor concentration in the reaction solution is thus reduced and hence there now exist two competing reactions (nucleation and the growth) that both require cadmium and selenide ions. On initial nucleation, depletion of the reagent and the inherent temperature drop upon injection of room temperature reagents (TOPSe), prevents further nucleation. The synthesis is then stabilised at a temperature which provides sufficient energy to promote the slow and controlled growth of the small crystallites. This growth is consistent with "Ostwald ripening".[24] During this stage smaller, less stable crystallites (due to higher surface free energy) dissolve into the solvent. As a consequence of Ostwald ripening the QDs diffuse from smaller to larger crystallites. The size distribution of the colloidal suspension is therefore narrowed and hence the monodispersity increased.

2.1.1.3 Cadmium Selenide (CdSe) QD Synthesis

2.1.1.3.1 QD Materials

Cadmium acetate ($Cd(Ac)_2$, 99.99 +%, ChemPur), trioctylphosphine (TOP, Fluka, 90 %, technical grade.), 1-hexadecylamine (HDA, 90 %, Aldrich, technical grade), trioctylphosphine oxide (TOPO, 90 %, Aldrich, technical grade 1-tetra-decylphosphonic acid (TDPA, 98 %, Alfa Aesar), selenium powder (Se, 99.99 %, Aldrich), toluene (99.9 %, VWR International) were used as supplied.

All glassware was cleaned by immersion in an ethanolic base bath (1 kg sodium hydroxide dissolved in 15 L ethanol), rinsed with distilled water, and placed into a nitric acid bath (2.5 L concentrated nitric acid made up to 10 L in water). Glassware was subsequently rinsed with distilled water. All water used was purified using a Barnstead NANOpure Diamond filtering system.

2.1.1.3.2 QD Synthetic Methodology

TOPSe and TOPCd precursor solutions were prepared >12 h prior to the synthesis under a dry atmosphere (argon). TOPSe was prepared by dissolving selenium (0.158 g) into TOP (2 ml). The cadmium stock solution, TOPCd was prepared by dissolving cadmium acetate (0.13 g) into TOP (3 ml).

A one-pot hot injection synthesis was used to prepare the CdSe QDs.[22] TOPO (8.0 g), HDA (5.0 g) and TDPA (0.15 g) were dried, degassed under vacuum and refluxed at 120 ˚C for 1.5 h. TOPSe was then added to the reaction mixture and the temperature increased to 300 ˚C. TOPCd was then rapidly injected under vigorous stirring resulting in the nucleation of CdSe QDs. The reaction temperature was reduced to 280 ˚C for particle growth. Once the desired QD size was reached (determined using UV-Vis absorption spectroscopy)[25] the reaction was quenched in 40 ml of toluene at room temperature. The apparatus for the hot injection synthesis is shown in Figure 2.1.

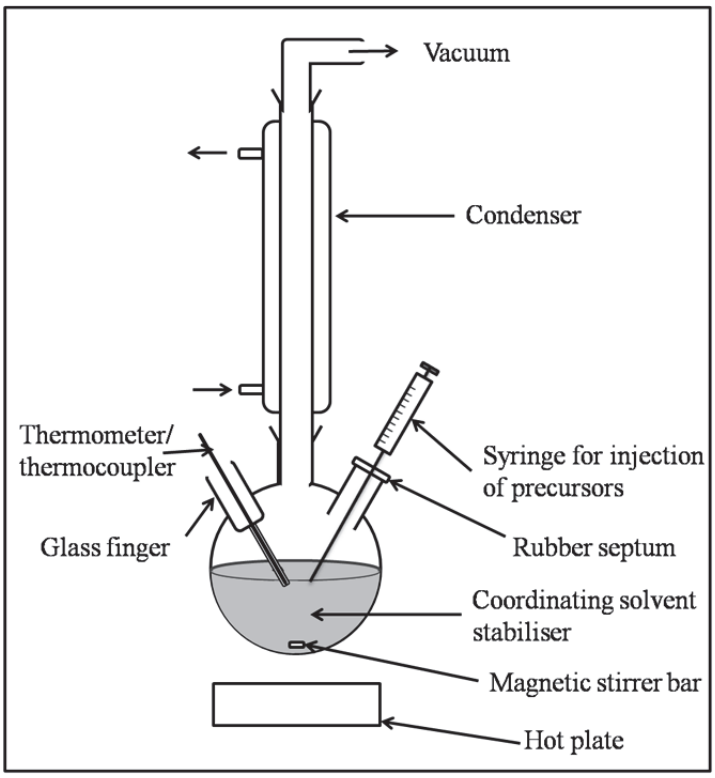

Figure 2.1. A schematic of the apparatus used in the hot injection synthesis of CdSe QDs.

2.1.1.3.3 The QD Washing Procedure

The washing procedure of the synthesised QDs prior to sensitization of the photoanode is illustrated in the schematic shown in Figure 2.2.

Figure 2.2. Schematic of washing procedure. 1. Quench reaction in room temperature toluene, 2. Precipitate QDs by addition of methanol, centrifuge to separate, 3. Decant colourless solution, 4. Re-disperse QDs in toluene. Repeat steps 2-4 for every subsequent washing "cycle" twice.

Initially, the growing hot QDs solution is quenched in 40 ml of room temperature toluene. In the ratio of 20 ml methanol: 15 ml quenched CdSe solution the QDs were precipitated and isolated by centrifugation (5500 rpm for 6 min). The colourless supernatant was then decanted, and the resultant orange pellet re-dispersed in 10 ml toluene. This was considered one washing "cycle". Further "cycles" involved the further precipitation (ratio of 10 ml of QD: 12 ml methanol), separation (centrifugation at 5500 rpm for 6 min) and then re-dispersion of the QDs (10 ml toluene). This stage was repeated desired number of "washes". The final orange pellet was dried, transferred into the dry box, and re-dispersed in the required volume of dry toluene solution to prepare an ~10 μM QD solution (as determined by UV-Vis spectroscopy – see section 2.3.1.1.1.2).

2.1.2 Molybdenum Disulfide (MoS_2)

MoS_2 nanosheet (colloidal solution and thin film) samples were prepared by Dr. Goki Eda. An outline of the procedure used to prepare the colloidal nanosheet dispersion of MoS_2 is given below. For full experimental details please see reference 26.

2.1.2.1 Preparation of MoS_2 Nanosheets

MoS_2 nanosheets and films were prepared by forced hydration exfoliation of Li_xMoS_2 following the method described in reference [26]. All MoS_2 films were prepared by Goki Eda. In brief, 3 g of natural MoS_2 crystals was immersed in 3 ml of 1.6 M butyllithium solution (hexane) for 2 days in an argon atmosphere followed by immediate exfoliation by sonicating in water for 1 hr. The solution was subsequently purified with excess hexane and the Li_xMoS_2 was isolated by repeated centrifugation. Thin films were prepared by suction filtration of the dilute suspensions 0.01 – 0.1 mg/ml) through a mixed cellulose ester membrane (25 nm pore, Millipore). The films were delaminated by slow insertion of the membrane/film into water, resulting in a free floating film at the surface. The film was then removed from the surface of the water and deposited onto FTO substrate which was then annealed at 300 ˚C in an argon atmosphere (glove box) with low oxygen and water levels (~1 ppm). Thin films with thicknesses spanning 1.7 – 18.9 nm (thickness determined by suspension concentration) were prepared.

2.1.2.2 MoS_2 Materials

Natural MoS_2 crystals (Sigma-Aldrich, 99 %), 1.6 M *n*-butyllithium solution in hexanes (Aldrich, 2.5 M), hexane (Sigma-Aldrich, 95 %) were used without purification.

2.2 Sensitizer substrate – Titanium Dioxide, TiO_2

Two sources of TiO_2 were used in this work as the mesoporous support on which the photoactive sensitizer was attached. Two sources of TiO_2 were utilized; commercially available (Dyesol) TiO_2 paste and Degussa P25 TiO_2. Rationalization and explanation for the two TiO_2 sources are detailed in the relevant chapters.

2.3 Characterisation Techniques

2.3.1 Optical Techniques

2.3.1.1 UV-Visible spectroscopy

UV-Visible (UV-Vis) spectroscopy is a technique used to measure the absorbance of a sample across the visible and ultraviolet regions of the electromagnetic spectrum. A monochromator selects and scans the wavelengths of the light incident on the sample. When the light passes through the sample some of the light is absorbed (and/or scattered), whilst the remainder is transmitted. The ratio of light absorbed (I) relative to the incident light (I_o) is termed transmission (%T) which is often expressed as a percentage, %T, defined by

$$\%T = \frac{I_0}{I} \times 100 \qquad (2.1)$$

Which can be expressed as absorbance, A

$$A = -\log\frac{I}{I_0} \qquad (2.2)$$

The dimensionless expression –log $[I/I_0]$ is known as the absorbance of the sample, *A*. Hence the expression becomes;

$$A = \varepsilon c l \qquad (2.3)$$

Which can be rearranged to become:

$$c = \frac{A}{\varepsilon l} \tag{2.4}$$

here ε ($dm^3\,mol^{-1}\,cm^{-1}$) is the molar absorption coefficient, c (mol dm^{-3}) is the solution concentration, and l (cm) is the path length of the beam through the sample.

2.3.1.1.1 UV-Visible Spectroscopy of QD Solutions

UV-Vis spectroscopy was used to monitor the QD sols throughout this thesis. In particular, the first excitonic peak position and width were utilized to monitor the solution stability, optical activity and QD size. The first exciton peak corresponds to the excitation of an electron from the ground state, E_0 to the first excited state, E_1 of the QD as shown in Figure 2.3.A. This is where the energy of the incident light (hv) corresponds to this energy gap ($E_1 - E_0$). A typical UV-Vis absorbance spectrum is shown in Figure 2.3.B.

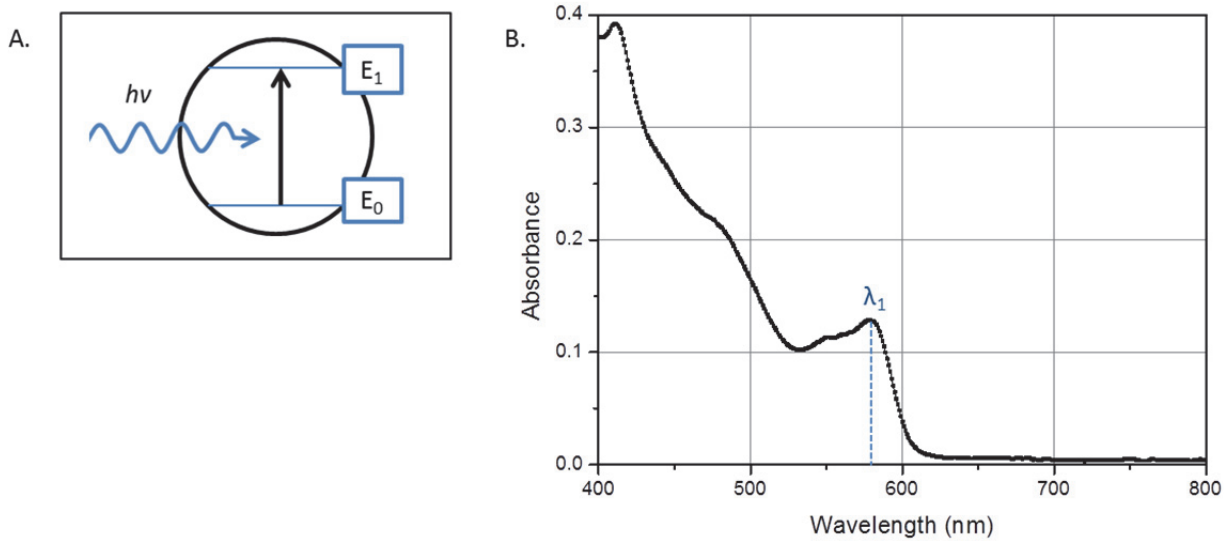

Figure 2.3. A. Schematic of the electron transfer (upon the absorbance of a photon, the excitation of an electron from the ground state, E_0 to the first excited state, E_1). B. The UV-Vis absorbance spectrum of a QD sol. λ_1 is the wavelength of the first excitonic peak.

2.3.1.1.2 Estimating the Size and Concentration of QDs

In 2003, Peng *et al.*[25] demonstrated that the extinction coefficient per mole of CdSe, CdS and CdTe QDs at the first excitonic absorption peak is strongly dependent on QD size. Equation (2. 5) is the empirical fit for CdSe QDs of a plot of λ (nm), the wavelength at the first excitonic absorption peak determined by UV-Vis spectroscopy (λ_1 on Figure 2.3), against D, the size (diameter, nm) of the QDs.

$$D = (1.6122 \times 10^{-9})\lambda^4 - (2.6575 \times 10^{-6})\lambda^3 + (1.6242 \times 10^{-3})\lambda^2 - (0.4277)\lambda + (41.57) \quad (2.5)$$

This dependence allows UV-Vis spectroscopy to be used as a tool to determine particle size. The empirical relationship between the experimental extinction coefficient per mole of particles and size of QDs was also determined using:

$$\varepsilon = 5857(D)^{2.65} \quad (2.6)$$

The quantum dot size can be determined and subsequently used to determine the absorption coefficient for that quantum dot size. The concentration of a CdSe QD solution can then be calculated using the absorption coefficient and Beer Lambert (Equation (2. 3)).

2.3.1.1.3 UV-Visible Spectroscopy of MoS_2

The concentration of colloidal dispersions of MoS_2 was estimated using the absorbance coefficient (ε_{672nm} = 3400 ml/mg/m), the determination of which is detailed in reference 27.

MoS_2 film thickness was estimated from the UV-Vis absorbance spectra of thin film MoS_2 in reference to the empirical data of reference 26.

$$T = \frac{A_{400nm} + 0.027}{0.055} \quad (2.7)$$

Where T is the film thickness (nm) and A_{400nm} is the absorbance at 400 nm.

2.3.1.1.4 UV-Visible Spectroscopy Instrumentation

UV-Vis spectroscopy was conducted on a Perkin Elmer, LambdaBIo10 spectrophotometer, with a spectral resolution of 2 nm using 1 cm path length quartz cuvettes.

2.3.1.1.5 Absorbance From a Light Scattering Sample

As described previously, absorption is calculated from the fraction of light transmitted by a sample relative to light incident on the sample as defined by Beer Lambert's law (Equation (2. 3)). If, however, a sample reflects (I_R) or scatters light (diffuse transmission), absorbance measurements in a linear (incident beam – sample – detector orientation) spectrophotometer, the absolute absorbance of a sample will not be measured. Reflectance and transmission have both specular and diffuse components as illustrated in Figure 2.4.

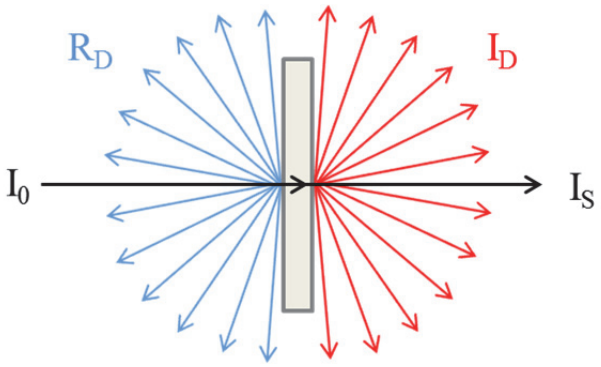

Figure 2.4. Schematic of light propagation through a sample that scatters. Upon reaching the sample, incident light (I_0) can be reflected (specular – here non measureable as it is coincident with incident beam; and diffuse R_D (blue)), or transmitted (specular (I_s) or diffuse (I_D) (red)).

Using an integrating sphere, the specular (I_S) and diffuse (I_D) components of transmission and the diffuse component of reflection (R_D) can be measured. A superior estimation for light absorbance from a sample that reflects/scatters light can be derived from Beer Lambert as detailed below. For a solid, non-scattering sample, Beer-Lambert is;

$$I_T = I_0 e^{-a.x} \qquad (2.\ 8)$$

Where I_T is the transmitted light, I_0 is the incident light, a is the absorption coefficient and x is the sample thickness. However, if the sample scatters light both I_T and I_0 will not be as measured in a linear spectrophotometer. The light transmitted by the sample is the sum of I_D and I_S;

$$I_T = I_D + I_S \tag{2. 9}$$

Given that the sample reflects a proportion of the incident light, R, the incident light on the sample available for absorbance is reduced to (1 – R)*I_0. Thus, a superior, absolute estimation of sample absorbance can be calculated from the following;

$$I_T = I_0(1 - R)e^{-ax} \tag{2. 10}$$

Where I_0 is the transmitted light measured with a reference and R is the fraction of light reflected from the sample relative to 100 % reflective reference. Hence e^{-ax} can be calculated and thus absorbance, A is estimated from the following calculations;

$$e^{-ax} = \frac{I_T}{I_0(1 - R)} \tag{2. 11}$$

$$T = \frac{I}{I_0} = e^{-ax} \tag{2. 12}$$

$$A = -\log_{10}(\frac{I}{I_0}) \tag{2. 13}$$

2.3.1.2 Steady State Photoluminescence Spectroscopy

Steady state photoluminescence spectroscopy (PL) (emission spectroscopy) is a complimentary technique to UV-Vis spectroscopy. In PL spectroscopy, the sample is excited by a wavelength of light of energy greater or equal to the first excitonic peak (λ_1). The wavelengths of emitted photons are monitored as the excited state returns to the ground state.

2.3.1.2.1 Steady State Photoluminescence Spectroscopy of CdSe QDs

Photoluminescence from a QD occurs when the quantum dot absorbs light of energy greater or equal to the first excitonic peak (λ_1) and subsequently, upon relaxation to the ground state, a photon is emitted (Figure 2.5 (A)).

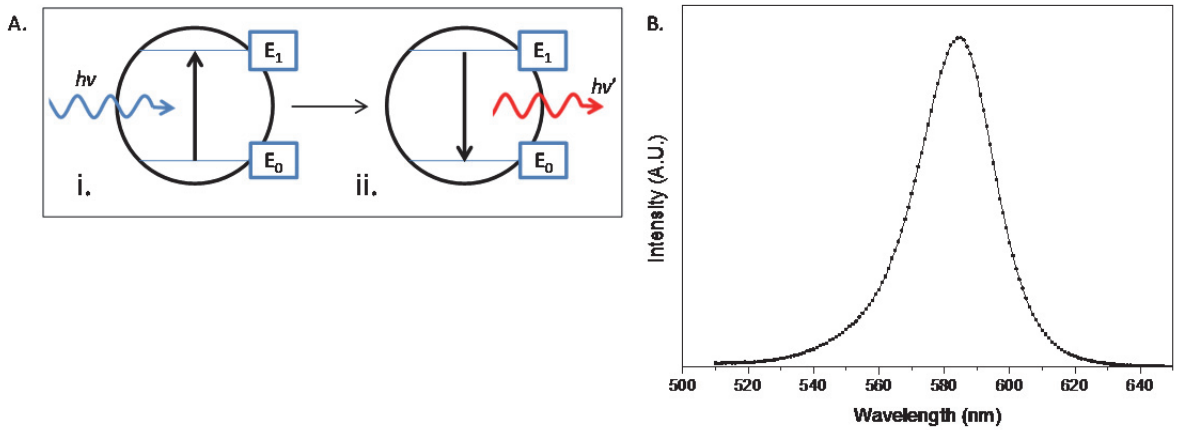

Figure 2.5. A. A schematic detailing the two steps of photoluminescence; (i) absorbance and (ii) emission. B. A typical Photoluminescence spectrum of CdSe QDs (the data corresponds to the same QD sol as in the absorbance spectrum in Figure 2.3).

Photoluminescence (PL) spectra were recorded with a view to estimating the size distribution of QD sols. Given the dependence of the band gap energies on QD size, the smaller the PL peak width (full width half maximum, fwhm), the smaller the QD size distribution.

2.3.1.2.2 Steady State Photoluminescence Instrumentation

PL measurements were conducted in 1 cm quartz cuvettes. The samples were illuminated by a 75W USHIO Xe short arc lamp bulb in conjunction LPS-220B Photon Technology International (PTi) lamp power supply. Light passed through a PTi monochromator with 3 nm resolution. Emission from the sample was collected at 90° to the incident light beam by a Dolan Jenner Optical Fibre to a 25 μm slit, passed through a second monochromator (also PTi with 3 nm resolution) and detected by a PTi 814 Photomultiplier detection system.

The full-width-half-maximum (FWHM) was estimated for PL spectra using Origin Gaussian fit.

2.3.1.3 Time Resolved Fluorescence

Time resolved fluorescence measurements probe the evolution of fluorescence signal with respect to time. In this work, pulse fluorometry is utilized whereby the sample is excited by a short laser pulse and the resultant fluorescence signal is monitored with respect to time. To interpret the data, the recorded fluorescence signal has to be deconvoluted from the incident laser pulse.

Time resolved fluorescence measurements were performed by Dr. Lefteris Danos.

2.3.1.3.1 Time Resolved Fluorescence Instrumentation

Time-correlated single photon counting (TCSPC) was used to measure Picosecond time-resolved emission spectra (TRES) and fluorescence decays using a FluoTime200 spectrometer (PicoQuant) equipped with a TimeHarp300 TCSPC board (PicoQuant) and a Hamamatsu photomultiplier (PMA-185). The excitation source was a 440 nm picosecond pulsed diode laser (PicoQuant, LDH440) driven by a PDL800-D driver (PicoQuant) operated at a variable pulse repetition rate (10-40 MHz). The emission from the QD films on FTO was collected perpendicular to the excitation laser beam. The emission arm was fitted with a long pass filter (HQ460LP, Chroma) before the monochromator (Scientech 9030). The full width half maximum (FWHM) of the system's instrument response function (IRF) was 200 ps.

The fluorescence decay curves were analysed using the FLUOFIT software (PicoQuant, version 4.2.1) based on multi-exponential models involving an iterative reconvolution process. The appropriateness of the fits was assessed by the reduced chi2 value (less than 1.20 accepted) and a visual inspection of the fit and data match.

TRES measurements and data fitting were performed by Dr. Lefteris Danos at the University of Southampton.

2.3.2 Morphology

2.3.2.1 Scanning Electron Microscope (SEM)

Scanning electron microscopy (SEM) is a technique used to image the surface of samples. In brief, the technique scans the surface with a beam of focussed, high energy electrons which interact with the surface being scanned producing a combination of secondary electrons, back-scattered electrons and X-rays. Detection of these can reveal details of the surface morphology and chemical composition.

2.3.2.1.1 SEM Instrumentation

A high resolution field emission gun scanning electron microscope (FEG-SEM) (LEO Gemini 1525) was used for all SEM imaging.

2.3.2.1.2 SEM Imaging of TiO_2

SEM imaging was also conducted to estimate crystallite size (Figure 2.6). The Dyesol crystallite size is ~50 – 100 nm. Crystallites in the Degussa P25 TiO_2 are slightly smaller on average, ~20 – 100 nm.

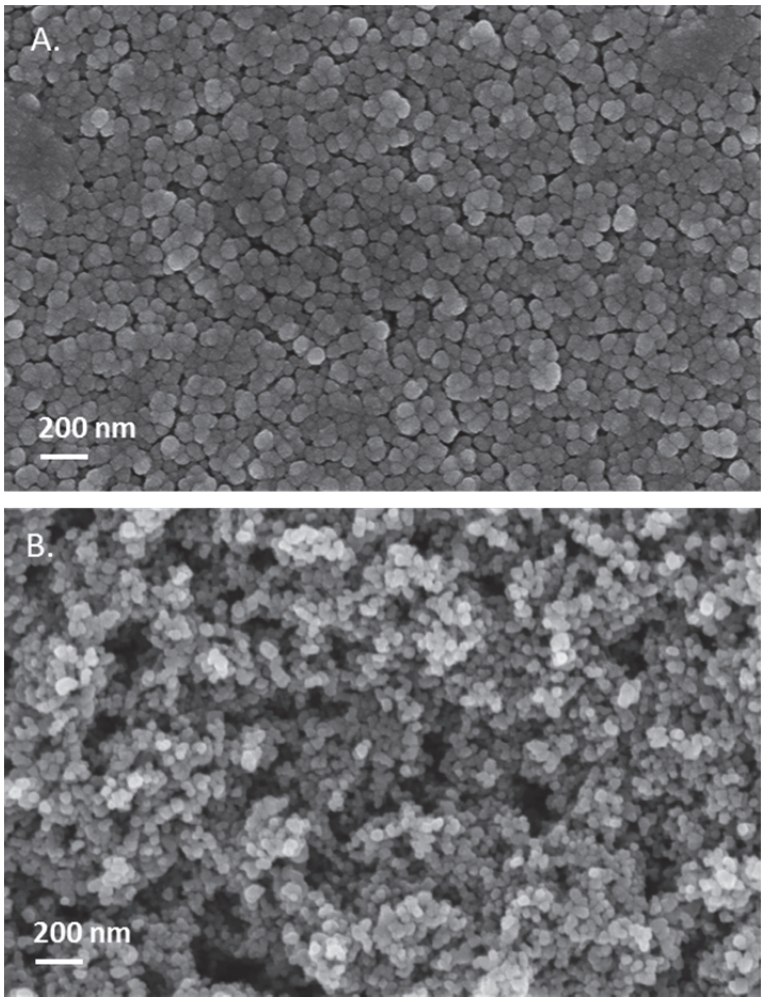

Figure 2.6. SEM images of TiO_2 films prepared from A. Dyesol TiO_2 paste and; B. P25 suspension.

2.3.2.1.3 Scanning Electron Microscopy – Energy Dispersive X-ray (SEM-EDX)

Scanning Electron Microscopy – Energy Dispersive X-ray (SEM-EDX) is a technique utilized to identify the elemental contents of a sample. Under incident electron radiation, ionised atoms in the sample relax by shell-to-shell transitions resulting in the emission of both electrons and X-ray radiation. The wavelength of the emitted X-ray radiation is characteristic of their atomic structure thus enabling elemental identification.

2.3.2.1.4 SEM-EDX Instrumentation

SEM-EDX was performed on the LEO Gemini 1525 SEM which is fitted with Oxford Instruments INCA energy dispersive and wavelength dispersive x-ray spectrometers (EDX) for elemental analysis.

2.3.2.1.5 TiO_2 SEM Cross Section Imaging

SEM imaging of the cross section of TiO_2 films was also used to determine crystallite size and film thickness. Samples were prepared for cross-sectional analysis using a diamond cutter (FTO side) and subsequently snapping the glass. Thus the technique is crude and in some areas the film was not visible. However, areas where the SEM image remains in focus across the cross-sectional profile enable an approximation of film thickness. Figure 2.7 shows an example of a TiO_2 film cross section, the film thickness was shown to be ~4.5 ± 0.5 μm.

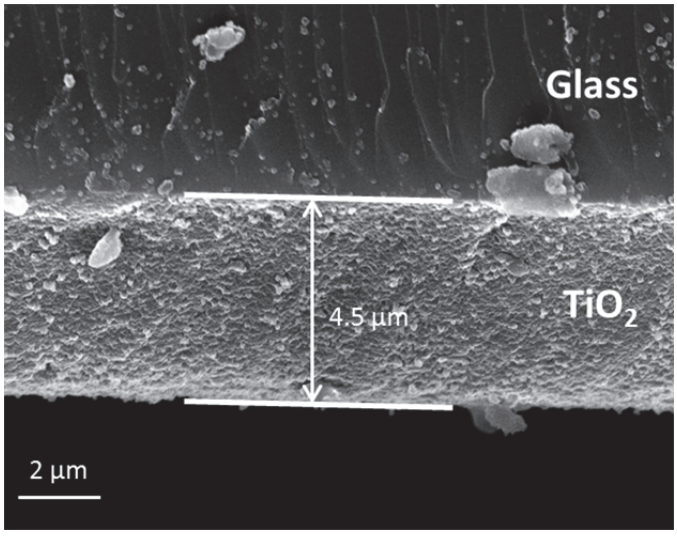

Figure 2.7. Cross section of TiO_2 film on glass.

2.3.2.2 Atomic Force Microscope (AFM)

Contrary to the electron microscopy techniques AFM enables insight into the surface topography of a sample. The technique uses a cantilever which is used to scan the surface. As the probe is brought in proximity to the sample surface the tip is deflected due to forces of interaction between the cantilever and material. The cantilever position (height) is determined using a laser beam and hence enables mapping of the topography of the surface.

2.3.2.2.1 AFM Instrumentation

Atomic force microscopy (AFM) was performed using a VeeCo Nanoscopy 4 controller, in multimode SPM tapping-mode with silicon tips. AFM was conducted by Dr. Richard Thorogate in the London Centre for Nanotechnology, University College London.

2.3.2.3 Focused Ion Beam- Scanning Electron Microscope (FIB-SEM)

FIB-SEM contains both a focused ion beam and scanning electron microscopy. Here the dual beam was used to prepare samples (lamella) for TEM microscopy. The FIB uses a gallium (Ga^+) ion beam to image and mill small trenches at localised sites across the sample surface. The gas injection system (GIS) is used to pattern platinum at the surface thus enables the lift out of the as prepared lamella with an omniprobe. Both FIB and SEM imaging are used to monitor the lamella preparation, lift-out and surface cleaning.

2.3.2.3.1 FIB-SEM Instrumentation

A Helios NanoLab™ DualBeam™ Focused Ion Beam (FIB) SEM was used to prepare and lift-out samples for transmission electron microscope (TEM).

2.3.2.4 Transmission Electron Microscope (TEM)

In transition electron microscopy the incident electron beam passes through and therefore interacts with the sample. The electron beam interacts with the sample material and an image is constructed from transmitted electrons.

2.3.2.4.1 TEM Instrumentation

Two transmission electron microscopes (TEM) were utilized in this thesis. All samples were prepared using the FIB-SEM detailed above. Unless otherwise stated, the high resolution JEOL 2012 TEM fitted with a Gatan Multiscan CCD camera was used.

The FEI TITAN 80/300 TEM/STEM was also used to image a sample. Prior to imaging, the sample was plasma cleaned. Titan TEM microscopy was conducted by Dr. Mahmoud Ardakani.

2.3.3 Chemical Analysis

2.3.3.1 Inductively Coupled Plasma – Optical Emission Spectroscopy (ICP-OES)

Inductively coupled plasma – optical emission spectroscopy (ICP-OES) is a technique that enables the analytical detection of trace elemental concentrations. In brief, the sample is dissolved in an appropriate solvent and injected through a nebulizer into plasma. The ions and electrons in the plasma continually recombine/re-ionize and thus emit light at wavelengths characteristic to their atomic structure, i.e. elemental specific. The light is collected and focused onto an optical emission spectrometer which measures the light intensity with respect to wavelength. A calibration curve for light intensity is prepared from four samples of the relevant elements at known concentrations. The samples are subsequently introduced into the ICP and the elemental solution concentration is calculated.

2.3.3.1.1 ICP-OES Instrumentation

Data was collected with an iCAP 6300 Duo View ICP Spectrometer with automated sampler, Thermo Fisher Scientific. The data was analysed and thus concentrations determined using Thermo Fisher Scientific iCAP 6300 iTEVA software.

Elemental concentrations were determined at the most intense atomic emission for each of the elements analysed (titanium (Ti) 323.452 nm, cadmium (Cd) 228.802 nm, phosphor (P) 177.495 nm, selenium (Se) 196.026 nm and sulfur (S) 166.669 nm. Calibration was conducted against a set of four standard solutions each at 0, 1, 5 and 20 ppm concentration of each element of interest.

2.3.3.2 Nuclear Magnetic Resonance (NMR)

Nuclear magnetic resonance (NMR) is the phenomenon which occurs when nuclei of non-integer spin are exposed to a static magnetic field and are subject to a second oscillating magnetic field. For proton (^{1}H) NMR hydrogen nuclei has a spin of ½ and thus have two energy levels which can be either aligned with or against an applied magnetic field. The oscillating electromagnetic radiation is applied at a frequency which causes the nuclei to flip from the lowest energy level to the upper level. At a given magnetic strength, the energy gap between the two levels is primarily dependent on the identity of the nucleide. The energy gap is however also dependent on the distribution of electrons around the nucleus due to neighbouring atoms in the molecule, local magnetic fields and the nucleus resonate frequency. This shifts the frequency of the NMR signal and is known as chemical shift. The orientation of surrounding nuclei (the effect is known as spin-spin coupling and results in the splitting of the signal for each type of nucleus).

2.3.3.2.1 NMR Instrumentation

A Bruker AvanceIII 600 MHz spectrometer equipped with a TCI triple-resonance cryoprobe was used for NMR spectroscopy. NMR spectroscopy was conducted by Dr. Pete Simpson, Imperial College London.

2.3.3.3 Fourier Transfer Infrared (FT-IR) Spectroscopy

Fourier Transfer Infrared Spectroscopy (FT-IR) spectroscopy utilizes the infrared region of the electromagnetic spectrum to excite samples. In principle, similar to UV-Vis absorbance spectroscopy the absorbance/transmission of a sample under infrared illumination is recorded. The position, strength and width of an absorbance peak in IR spectrum is used to identify chemical species and reveals information such as the reduced mass of the atoms, bond strengths, dipole moment as well as chemical environment of a chemical bond.

2.3.3.3.1 FT-IR Instrumentation

A Bruker Hyperion 2000 in reflectance mode was used to measure FT-IR spectra of the samples.

2.3.3.4 Secondary Ion Mass Spectroscopy (SIMS)

Secondary Ion Mass Spectroscopy (SIMS) is technique used to determine the surface composition of a material. In brief, the surface is bombarded with ions resulting in the ejection of secondary particles, consisting of both charged (ionic) and neutral species. Charged species, known as secondary ions, can be collected using a mass spectrometer allowing the identification of the depth dependent elemental and isotopic composition.

2.3.3.4.1 Secondary Ion Mass Spectroscopy Instrumentation

SIMS analysis was performed on a TOFSIMS^5 instrument (ION-TOF GmbH, Münster, Germany). SIMS was performed by Dr Helena Tellez Lozano, Imperial College London.

2.3.4 Photoelectrochemical Techniques

2.3.4.1 Photocurrent Spectroscopy

Photocurrent spectroscopy is the measurement of the current response of a photoelectrode under monochromatic illumination. Unlike UV-Vis absorbance where the ability of the material to absorb light is monitored, here the ability of the material to convert light of known wavelength into current is monitored.

Two types of photocurrent measurements were conducted; incident photons-to-current efficiency (IPCE) and absorbed photon-to-current efficiency (APCE). Both measurements utilize the same photocurrent measurement setup.

2.3.4.1.1 Photocurrent Spectroscopy Instrumentation

For photocurrent measurements where the signal could not be distinguished from experimental noise, phase sensitive detection (a lock-in amplifier) was used to measure the photocurrent data. Here the data were recorded using an in-house program (developed by Dr. D. J. Riley). A schematic of the in-house assembled experimental setup is shown in Figure 2.8. Under chopped monochromatic incident light the photocurrent response of samples held at a pre-determined potential controlled by the potentiostat is monitored with a three-electrode cell configuration as a function of the incident wavelength. For samples where photocurrent signal was distinguishable from experimental noise, the same setup was utilized without the lock-in amplifier and optical chopper. For these samples the photocurrent data was collected using the GPES (Autolab) software.

A computer controlled Autolab potentiostat (μAutolabI) was used to control the electrochemistry in the cell. A 50 W xeon lamp powered by a LPS-220B power supply (Photon Technology International (PTi)) illuminated the sample through a PTi SID-101 monochromator. A Stanford Research Systems (SRS) SR830 DSP lock-in amplifier was used with a PTi Optical Chopper System (OC-4000).

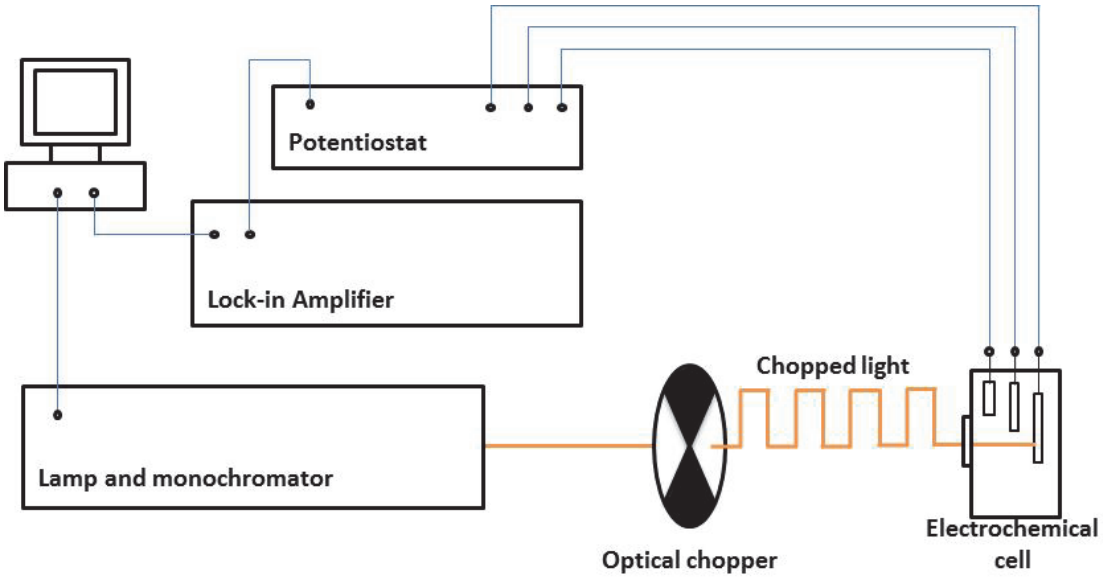

Figure 2.8. The experimental setup for photocurrent measurement where a lock-in amplifier is necessary to distinguish the signal from background experimental noise.

2.3.4.1.2 The Electrochemical Cell

For all electrochemical methods (voltammetry and photocurrent measurements) a standard three-electrode setup was utilized. The cell block was designed in house with assistance from TgK Scientific Ltd. The three-electrode cell was fitted with fused silica windows for illumination. A platinum gauze/wire was used as the counter electrode for all measurements. Silver/silver chloride/1 M potassium chloride (Ag/AgCl/1M KCl) reference electrodes were used for all measurements (unless otherwise stated).

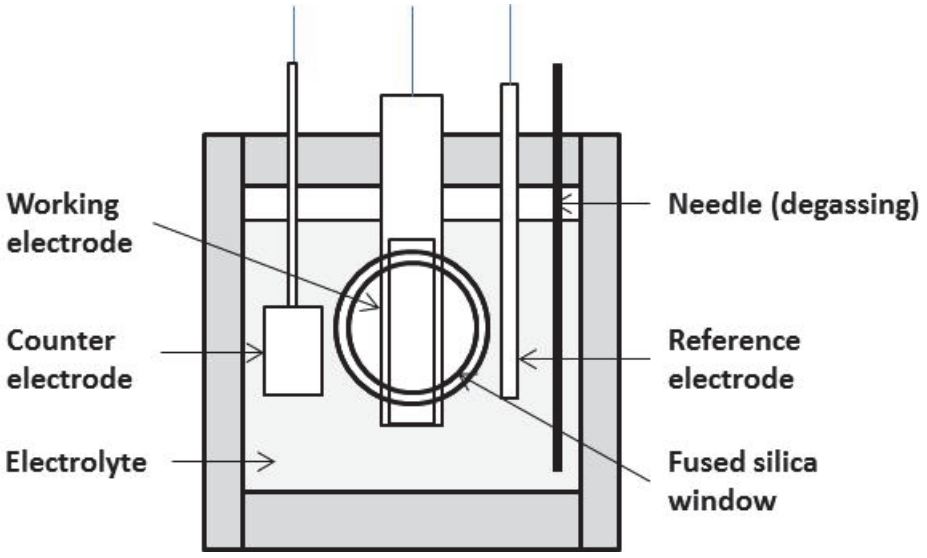

Figure 2.9. The electrochemical cell used in all photocurrent and voltammetry measurements.

2.3.4.1.3 The Electrochemical Cell Technical Drawings

An exploded view and the technical drawings detailing the dimensions of the electrochemical cell are shown in Figure 2.11 - 13. The drawings were provided by TgK Scientific with assistance from Miss A. King.

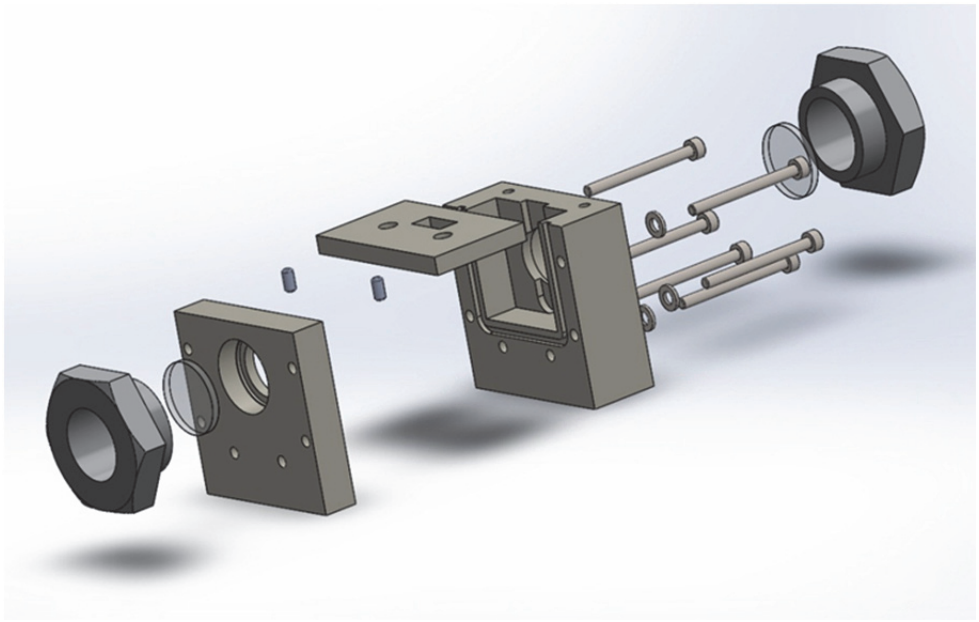

Figure 2.10. An exploded view of the electrochemical cell.

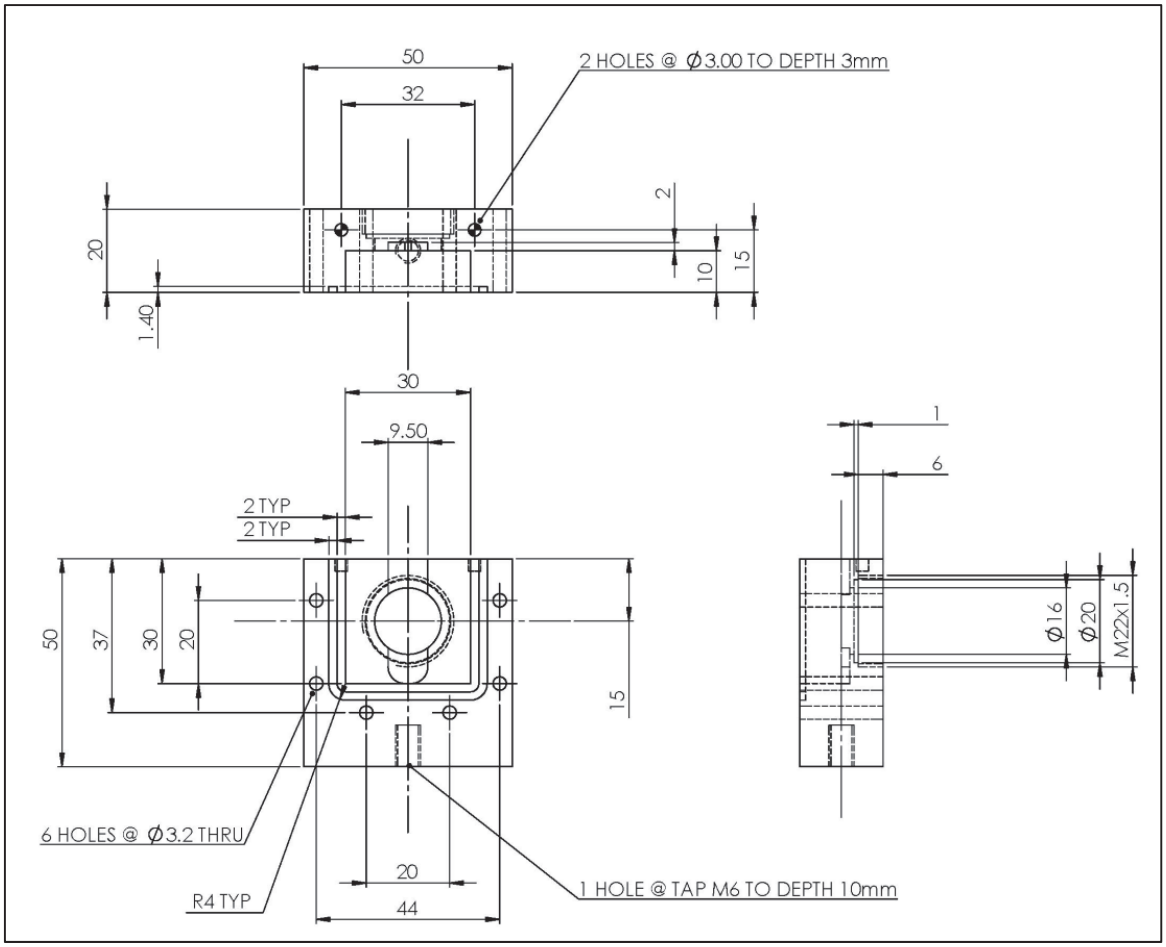

Figure 2.11. Technical drawing of the main cell body.

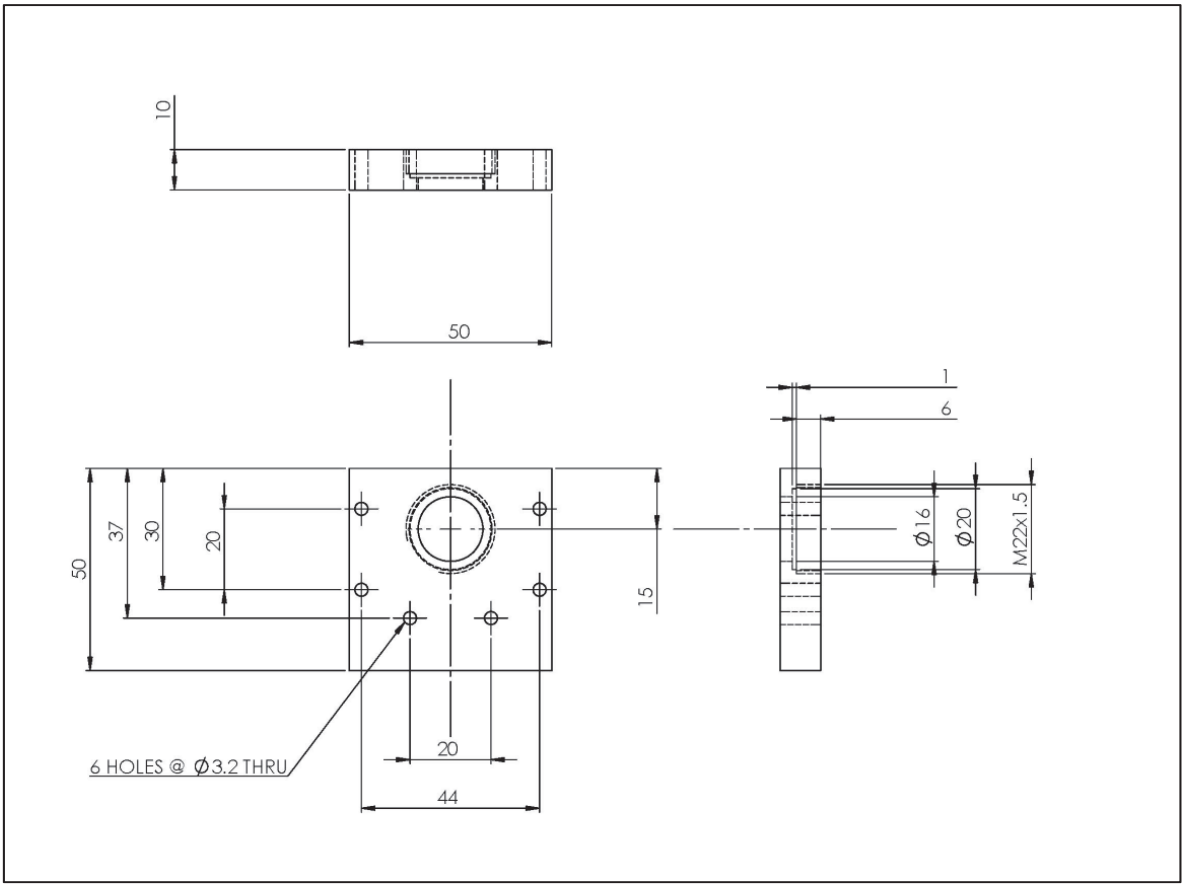

Figure 2.12. Technical drawing of the cell closure plate.

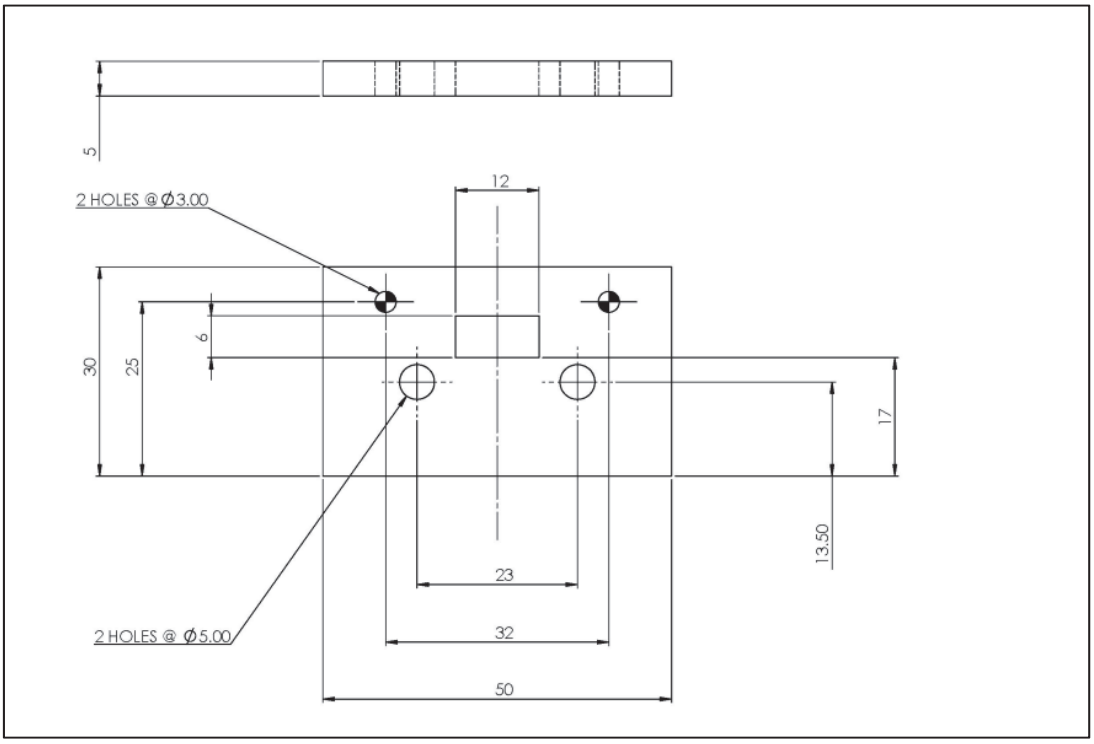

Figure 2.13. Technical drawing of the cell lid.

2.3.4.1.4 Incident Photons to Current Efficiency (IPCE)

Photocurrent signals recorded using the equipment shown in Figure 2.8 must be calibrated against the incident lamp power to provide data correlating to the sample. Photocurrent data is often presented as the "incident photon to current efficiency" (IPCE). IPCE, Φ is the ratio of the number of photons incident on the sample, n_p to the number of electrons recorded as current.

$$\emptyset = \frac{n_e}{n_p} \times 100 \tag{2. 14}$$

The number of incident photons can be calculated if the power of the light incident on the sample is known. Lamp power is measured in Watts (W), or energy (joules) per unit time (s) per area (cm^2). The energy of a photon (E_P) is dependent on the wavelength, λ as detailed in Equation (2. 15).

$$E_p = \frac{hc}{\lambda} \tag{2. 15}$$

The power (P_λ) of monochromatic light is measured using a power meter. The number of photons, n_p can be calculated

$$n_p = \frac{P_\lambda}{E_p} \tag{2. 16}$$

$$n_p = \frac{P}{hc/\lambda} \tag{2. 17}$$

To calculate the number of electrons the change in electrical current under illumination (photocurrent), I_s is measured. Current, measured in amperes is the measurement of electric charge passing through a point per unit of time (s). The number of electrons, n_e can therefore be calculated

$$n_e = \frac{I_s}{e} \tag{3. 18}$$

where e is the magnitude of the charge carried by an electron (elementary charge).

Hence, IPCE can be calculated;

$$\phi = \frac{\left(\frac{I_S}{e}\right)}{\left(\frac{P_\lambda}{hc/\lambda}\right)} \times 100 \qquad (2.19)$$

2.3.4.1.5 Absorbed Photon-to-Current-Efficiency (APCE)

A further interpretation of photocurrent data is the absorbed photon to current efficiency (APCE) whereby the ratio of photons absorbed by the material and converted into current is calculated as below.

$$\text{APCE} = \text{IPCE}/(1 - T(\lambda)) \qquad (2.20)$$

where $T(\lambda)$ is the transmittance and thus the denominator is the fraction of incident photons absorbed by the sample.

2.3.4.2 Voltammetry

Voltammetric scans were setup using the same configuration as described for photocurrent measurements. A potential is applied to the working electrode in a three-electrode cell configuration (with respect to a reference electrode potential). The potential is then scanned across a predetermined range and the working electrode current response of the working electrode is measured.

2.3.1.4.2.1 Voltammetry Instrumentation

The supplied GPES (Autolab) software was used to control the Autolab potentiostat (μAutolabI) and collect data.

2.4 Further Experimental Details

The purpose of this chapter is to provide brief overviews and details of common experimental techniques and procedures used throughout this thesis. Where necessary, further details of experimental procedures and techniques are given in the subsequent and relevant chapters.

2.5 References

(1) Wang, Y.; Suna, A.; Mahler, W.; Kasowski, R. *J. Chem. Phys.* **1987**, *87*, 7315.

(2) Gao, M. Y.; Yang, Y.; Yang, B.; Bian, F. L.; Shen, J. C. *Journal of the Chemical Society-Chemical Communications* **1994**, 2779.

(3) Moffitt, M.; Eisenberg, A. *Chemistry of Materials* **1995**, *7*, 1178.

(4) Moffitt, M.; McMahon, L.; Pessel, V.; Eisenberg, A. *Chemistry of Materials* **1995**, *7*, 1185.

(5) Petit, C.; Jain, T. K.; Billoudet, F.; Pileni, M. P. *Langmuir* **1994**, *10*, 4446.

(6) Watzke, H. J.; Fendler, J. H. *J. Phys. Chem.* **1987**, *91*, 854.

(7) Towey, T. F.; Khanlodhi, A.; Robinson, B. H. *J. Chem. Soc.-Faraday Trans.* **1990**, *86*, 3757.

(8) Wang, Y.; Herron, N. *J. Phys. Chem.* **1987**, *91*, 257.

(9) Wilhelmy, D. M.; Matijevic, E. *Journal of the Chemical Society-Faraday Transactions I* **1984**, *80*, 563.

(10) Niitsoo, O.; Sarkar, S. K.; Pejoux, C.; Ruhle, S.; Cahen, D.; Hodes, G. *J. Photochem. Photobiol. A-Chem.* **2006**, *181*, 306.

(11) Lee, H.; Wang, M. K.; Chen, P.; Gamelin, D. R.; Zakeeruddin, S. M.; Gratzel, M.; Nazeeruddin, M. K. *Nano Lett.* **2009**, *9*, 4221.

(12) Nightingale, A. M., deMello, J. C., *Adv. Mater.* **2012**.

(13) Murray, C. B.; Kagan, C. R.; Bawendi, M. G. *Annu. Rev. Mater. Sci.* **2000**, *30*, 545.

(14) Murray, C. B.; Norris, D. J.; Bawendi, M. G. *Journal of the American Chemical Society* **1993**, *115*, 8706.

(15) Trindade, T.; O'Brien, P.; Pickett, N. L. *Chemistry of Materials* **2001**, *13*, 3843.

(16) Qu, L. H.; Peng, Z. A.; Peng, X. G. *Nano Lett.* **2001**, *1*, 333.

(17) Peng, Z. A.; Peng, X. G. *Journal of the American Chemical Society* **2001**, *123*, 183.

(18) Qu, L. H.; Peng, X. G. *Journal of the American Chemical Society* **2002**, *124*, 2049.

(19) Peng, Z. A.; Peng, X. G. *Journal of the American Chemical Society* **2002**, *124*, 3343.

(20) Aldana, J.; Wang, Y. A.; Peng, X. G. *Journal of the American Chemical Society* **2001**, *123*, 8844.

(21) Talapin, D. V.; Rogach, A. L.; Kornowski, A.; Haase, M.; Weller, H. *Nano Lett.* **2001**, *1*, 207.

(22) Mekis, I.; Talapin, D. V.; Kornowski, A.; Haase, M.; Weller, H. *Journal of Physical Chemistry B* **2003**, *107*, 7454.

(23) LeMer, V.; Dinegar, R. H. *J. Am. Chem. Soc.* **1950**, *72*, 4847.

(24) Voorhees, P. W. *J. Stat. Phys.* **1985**, *38*, 231.

(25) Yu, W. W.; Qu, L. H.; Guo, W. Z.; Peng, X. G. *Chemistry of Materials* **2003**, *15*, 2854.

(26) Eda, G.; Yamaguchi, H.; Voiry, D.; Fujita, T.; Chen, M. W.; Chhowalla, M. *Nano Lett.* **2011**, *11*, 5111.

(27) Coleman, J. N.; Lotya, M.; O'Neill, A.; Bergin, S. D.; King, P. J.; Khan, U.; Young, K.; Gaucher, A.; De, S.; Smith, R. J.; Shvets, I. V.; Arora, S. K.; Stanton, G.; Kim, H. Y.; Lee, K.; Kim, G. T.; Duesberg, G. S.; Hallam, T.; Boland, J. J.; Wang, J. J.; Donegan, J. F.; Grunlan, J. C.; Moriarty, G.; Shmeliov, A.; Nicholls, R. J.; Perkins, J. M.; Grieveson, E. M.; Theuwissen, K.; McComb, D. W.; Nellist, P. D.; Nicolosi, V. *Science* **2011**, *331*, 568.

Chapter 3. The Influence of Purification on QD Sensitization

3.1 Introduction

Many applications of QDs, most utilize QDs require their attachment to a surface. The work presented in this chapter concerns the attachment of QDs to a mesoporous TiO_2 surface and hence specifically relates to QD sensitized solar cells (QDSSC).[1]

QDs synthesized using the hot injection technique detailed in Chapter 2 were used in the following experiments. Prior to the employment of synthesized "TOPO" CdSe QDs, the solution is subject to purification. The common purification entails the successive precipitation of QDs via centrifugation with a solvent/non-solvent followed by re-dispersion in solvent. When the QDs are dispersed in the non-solvent (e.g. methanol) the QDs are non-soluble. Conversely, any unbound surface ligand (TOPO/TOPSe) is soluble and thus can be removed from the system by separation. Throughout much of the literature, details of QD purification procedure are frequently partially, and in some cases completely, omitted. There have, however, been a few studies which have established the importance of the purification with respect to the number and nature of surface bound ligands.[2,3] Alongside the removal of excess ligands, the number and nature of surface bound ligands was shown to evolve. Impurities present in technical-grade TOPO and TOP have also recently been recognized as surface bound species.[4,5] Specifically, TOPO is not the only surface bound chemical in "TOPO" QDs, rather, the common impurities sourced in technical grade TOPO and TOP (amongst others) are also present (e.g. *n*-octylphosphonate, and P'-P'-(di-*n*-octyl) pyrophosphonate). The ratio between surfactants and these impurities has also been shown to evolve with purification.

In inorganic chemistry ligands are categorized into two types; X- and L-type. X-type have a negatively charged headgroup. L-type (such as TOPO) are neutral with respect to charge and coordinate to the QD with an electron lone pair interaction. Due to the stronger electrostatic interaction, X-type ligands are known to bind more favorably to the QD relative to L-type. Normally L-type ligands are reversibly bound to the surface

whereas X-type are irreversibly bound. Owen *et al.* investigated the type of bound species present at the surface of the "TOPO" QDs through cleavage of bound ligands and spectroscopic analysis.[6] It was concluded that post purification X-type ligands (sourced from the impurities of TOPO) populate the majority of the QD surface post purification. It is of note that the majority of the QD ligands (impurities and intentional) contain phosphorous. More recently, Weiss *et al.* used a combination of X-ray photoelectron spectroscopy (XPS), inductively coupled plasma-atomic emission spectroscopy (ICP-AES) and phosphorous NMR spectroscopy to identify and quantify different types of ligands at the surface of the QD at different stages in the washing procedure.[5] These surface bound ligands and the ligand type are listed below in Table 3.1.

Ligand name	**Ligand chemical structure**	**Ligand type**
trioctylphosphine selenide, cadmium, oxide (TOPSe, TOPCd, TOPO)	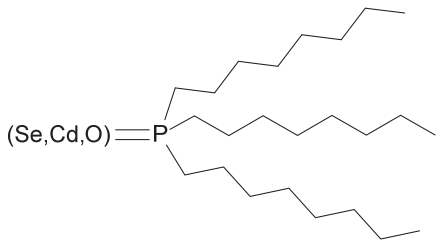	L-type
trioctylephosphine (TOP)	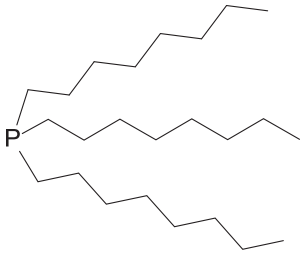	L-type
n-tetradecylphosphonic acid (TDPA)	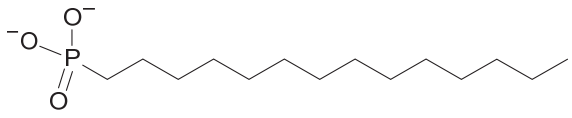	X-type
hexadecylamine (HDA)	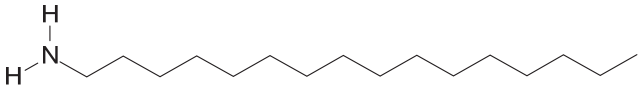	L-type

n-octylphosphonate (OPA)	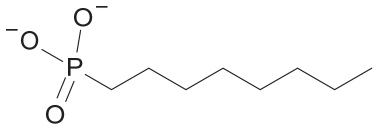	X-type
P'-P'-(di-*n*-octyl) pyrophosphonate (PPA)	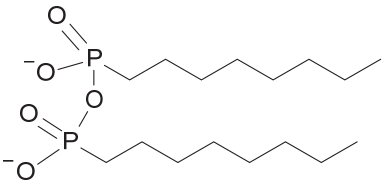	X-type

Table 3.1. The names and chemical structures of ligands present in QDs prepared by hot-injection, as determined in reference 5. The ligand type (X- or L-) is also detailed.

It was shown that throughout the washing procedure predominantly X-type ligands occupy the binding sites on the surface of the QDs. Quantitative analysis revealed that as the washing procedure proceeds, free ligands are removed from the QD solution such that by the third purification cycle less than 15 % of the QD surface area was occupied with L-type ligands whilst X-type ligands occupied a constant 84 % of the area.

Initial studies on both the influence of QD purification on QD sensitized at a surface were conducted by Sambur et al.[7] No photocurrent was observed with photoanodes exposed to unwashed (analogous to "0 wash" in this paper) QD solutions. This observation was attributed to low QD adsorption and/or a high concentration of bulky surfactants present in the unwashed QD solution which hindered the penetration of the linker molecule, 3-Mercaptopropionic acid (3-MPA) (used to attach the QD to the TiO_2 surface)[3,8,9] into the QD TOPO/TOP ligand shell. The QD population was not, however, quantitatively determined.

In this chapter, through quantitative analysis and imaging, we quantitatively demonstrate the influence of QD purification on QD population, morphology and ability to photo-inject electrons into a mesoporous TiO_2 photoanode. Utilizing the recent literature on the identity of surface bound ligands we apply and extend this understanding to the application of QDSSCs. Quantitative analysis of the population of QDs adsorbed at a surface reveal a large increase upon enhanced QD purification. Imaging of the samples reveals the morphology of the surface bound structures (agglomerates). Upon enhanced purification, the surface bound species evolve from a

lower population of large sized aggregates to a higher population of smaller sized agglomerates. We therefore demonstrate the importance of detailing the common purification with respect to understanding the nature and performance of QDSSCs.

3.2 Experimental Methods

3.2.1 Chemicals and Materials

The linker molecule and sensitizing solutions were prepared with 3-mercaptopropionic acid (3-MPA, 99 +%, Aldrich), acetonitrile (anhydrous 99.8 %, Aldrich) and toluene (anhydrous 99.8 %, Aldrich) used as supplied. 18-NR-T titanium dioxide paste (Dyesol) was used to doctor blade the titanium dioxide films. TEC8 glass plate fluorinated tin oxide (FTO) coated glass slides (1 x 2.5 cm) (Dyesol) were used as optically transparent electrodes (OTE). Hydrochloric acid (HCl, 37 %, VWR), nitric acid (HNO_3, 68 %, BDH), sulfuric acid (H_2SO_4, 95 %, VWR) and hydrogen peroxide (H_2O_2, 30 %, Fischer Scientific) were used in the cleaning procedure of the FTO.

Calibration standards and sample solutions for ICP measurements were prepared using Ti (1000 mg/L Ti in 2% HNO_3, Fluka Analytical), Cd (1000 mg/L Cd in 2 % HNO_3, Fluka Analytical), P (1000 mg/L P in 2% HNO_3, Fluka Analytical) and nitric acid (HNO_3, 70%, Fisher) and concentrated sulfuric acid (H_2SO_4, 95 %, VWR). The instrument was calibrated with four solutions (0, 1, 5 and 20 ppm) of Ti, Cd and P, with a drop of H_2SO_4 in HNO_3 prior to measurement. All water used was purified using a Barnstead NANOpure Diamond filtering system.

The electrolyte (hole scavenger) used for photocurrent measurements was aqueous 0.5 M sodium sulphite (Na_2SO_3, ≥ 98 %, Sigma-Aldrich).

All glassware was cleaned by immersion in an ethanolic base bath (1 kg sodium hydroxide: 15 L ethanol) for 2 – 4 h, rinsed with distilled water, and placed into a nitric acid bath (2.5 L concentrated nitric acid: 10 L water). Glassware was subsequently rinsed with distilled water. FTO was cleaned by first immersion into an aqua regia solution (3 part concentrated HCl: 1 part concentrated HNO_3), for 5 min followed by thorough rinse with purified water. The FTO was then immersed into a piranha solution (4 parts concentrated H_2SO_3: 1 part 30 % H_2O_2) for 5 min, followed by another thorough rinse with purified water.

3.2.2 Purification of the QDs

QDs were synthesized following the route described in Chapter 2. Post synthesis, the QD solution was allowed to cool and stored in the dark >24 h prior to purification. This solution was considered "unpurified" and a portion was retained and labeled "0 wash". The remaining solution was subject to purification. 20 ml methanol: 15 ml "unpurified" QD solution were mixed and the QDs were precipitated and isolated by centrifugation. The colorless supernatant was decanted, and the resultant orange pellet re-dispersed in 10 ml toluene. This was considered one washing "cycle" and was labeled "1 wash". Subsequent "cycles" involved the further precipitation (10 ml of QD solution: 12 ml methanol), separation by centrifugation and then re-dispersion of the QDs (10 ml toluene). After every "cycle" a portion of the orange pellet was dried, transferred into the dry box, and re-dispersed in the required volume of dry toluene solution to prepare a *ca.*10 μM QD solution (as determined by UV-vis spectroscopy).[10] The purification procedure of the synthesized QDs is illustrated in the schematic below (Figure 3.1). At every stage of the purification a portion of *ca.*5ml was retained for sensitization/analysis. All comparisons between different levels of QD purification were made from one batch of QDs. In total four solutions were prepared; (x 0 – 3 wash). Solutions were re-used over a 12 months period for the sensitization of several films.

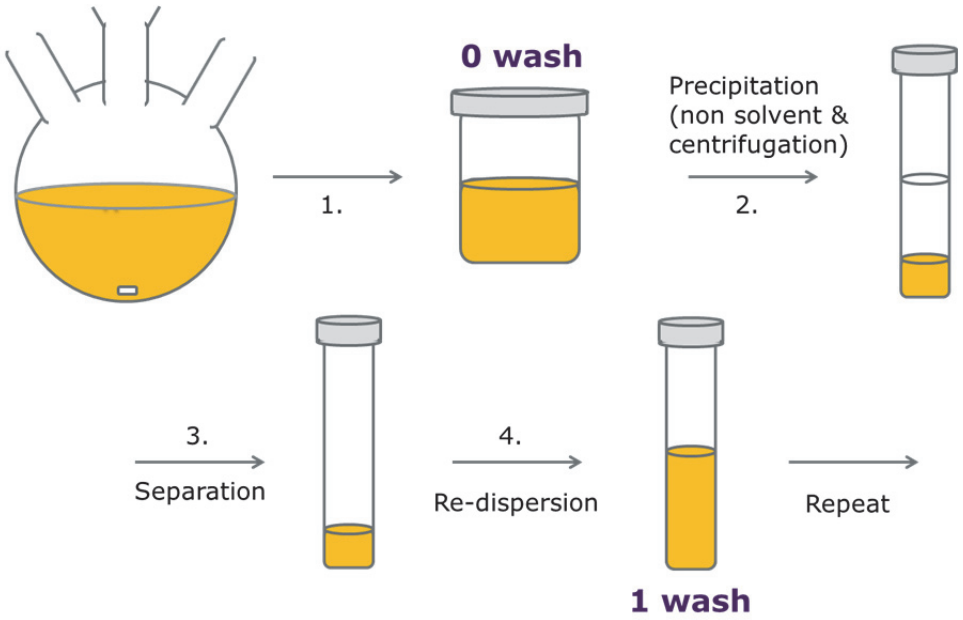

Figure 3.1. Schematic of the purification procedure of "TOPO encapsulated" CdSe QDs. 1. Quench QD synthesis reaction in cold solvent (0 wash): 2. Precipitation of QDs by addition of non-solvent and centrifugation: 3. Separation – remove colorless supernatant: 4. Re-disperse QDs in solvent (1 wash).

3.2.3 Preparation of CdSe-TiO_2 Photoanode (Sensitization)

Opaque TiO_2 films were prepared on the clean, conductive fluorine doped tin oxide (FTO) surface using the doctor-blade technique. The films were annealed in a furnace at 450 ˚C for 30 min. The TiO_2 films were sensitized with the QDs by linker assisted attachment. Initially, TiO_2 films were re-heated to 300 ˚C for 15 min, after which the temperature was reduced to 150 ˚C for >30 min. The hot films were then directly immersed into a dry acetonitrile solution containing 1 M 3-MPA, for >12 h. The functionalized films were washed with acetonitrile, then toluene and finally transferred into the prepared CdSe solutions (*ca.* 10 μM). The electrodes were immersed in the solution for >2 days, rinsed with toluene and left to dry in air. Between measurements, all QD solutions and electrodes were stored in the dark. Figure 3.2 shows a schematic representation of the preparation of the QD sensitized photoanode.

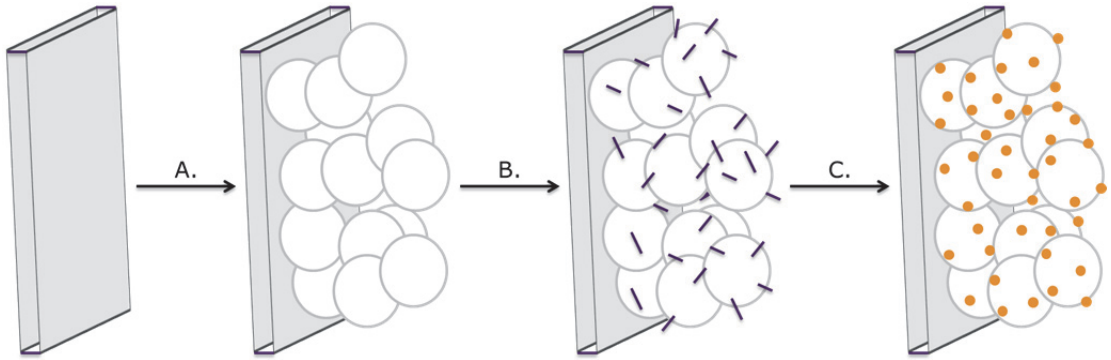

Figure 3.2. Schematic showing the three steps in the preparation of a CdSe sensitized photoanode. A. Doctor blade thin layer of TiO_2 onto conductive glass (FTO); B. Attach the linker molecule 3-MPA; C. Sensitize with CdSe QDs.

Photoanodes were prepared in sets of four electrodes. Each set was sensitized with a QD solution with a different level of purity; "0 wash", "1 wash", "2 wash" or "3 wash".

3.2.4 Optical Analysis of the Sols

Details of the UV-visible absorbance spectroscopy and photoluminescence equipment and setup are given in Chapter 2.

3.2.5 Chemical Analysis, Inductively Coupled Plasma – Optical Emission Spectroscopy (ICP-OES) of QD Sensitized Photoanodes

Sensitized TiO_2 films were crushed and dissolved in 1 ml of hot H_2SO_4 for >6 h. 0.8 ml of the solution was then diluted with 9.2 ml 2 M HNO_3. All samples compared were sensitized by the same batch of QDs. The ratio of Cd:Ti atoms was calculated thus eliminating error due to differences between the doctor bladed TiO_2 films. Three sensitized TiO_2 films for each of the four QD solutions were prepared, analysed and the average concentration determined. To verify that the measured elemental concentrations were within the range for the instrumentation additional mock solutions containing all of the elements present in the samples (cadmium, selenium, titanium, phosphor) plus the organic TOPO and sulphuric acid were prepared in the range of 0.001 – 1.0 ppm (Cd, Ti, and P elemental) concentration. Thus the detection limitation

for Cd, Ti and P were set as 0.1, 0.1 and 0.1 ppm respectively. Where readings were given lower than these limits the data was discarded.

ICP-OES analysis was run to quantitatively monitor the QD population at the surface of the mesoporous TiO_2 films. For each sample, the elemental concentrations of Cd, P and Ti were determined. Results are presented as a ratio of elemental content thus preventing experimental error due to any inconsistency (human error) in the dimensions of the doctor bladed TiO_2 film. All comparisons are made between samples prepared from the same batch of QDs (ca.3 nm diameter). Assuming no change in particle size distribution during washing, each of the sensitizing QD sols was identical.

3.2.6 Morphology – SEM and AFM Imaging

The influence of QD purification on the morphology of a QDs sensitized surface was determined by SEM and AFM. Due to the difficulties of imaging mesoporous structures, single crystal Si (111) with a native surface oxide (SiO_2) was used as a smooth surface replacement for TiO_2. All Si surfaces were treated analogously to the TiO_2 sensitization utilizing the bifunctional linker molecule 3-MPA to adsorb the CdSe QDs to the surface. A control experiment, Si crystal was heat treated and immersed in 3-MPA, (the same treatment as those sensitized by QDs) a smooth morphology is revealed by SEM and AFM imaging (Figure 3.3). Comparisons between the surface morphology of samples sensitized with QD solutions of differing purification were made. SEM imaging was performed using a FEG-SEM (LEO 1525). Typical surface morphology was determined by comparison of at least 7 different randomly selected areas with dimensions ~2.5 μm x 3 μm from each sample. Additional structural information was gained through tapping-mode atomic force microscopy (AFM) images were also obtained using a VeeCo, Nanoscope 4 controller, multimode SPM tapping mode with silicon tips.

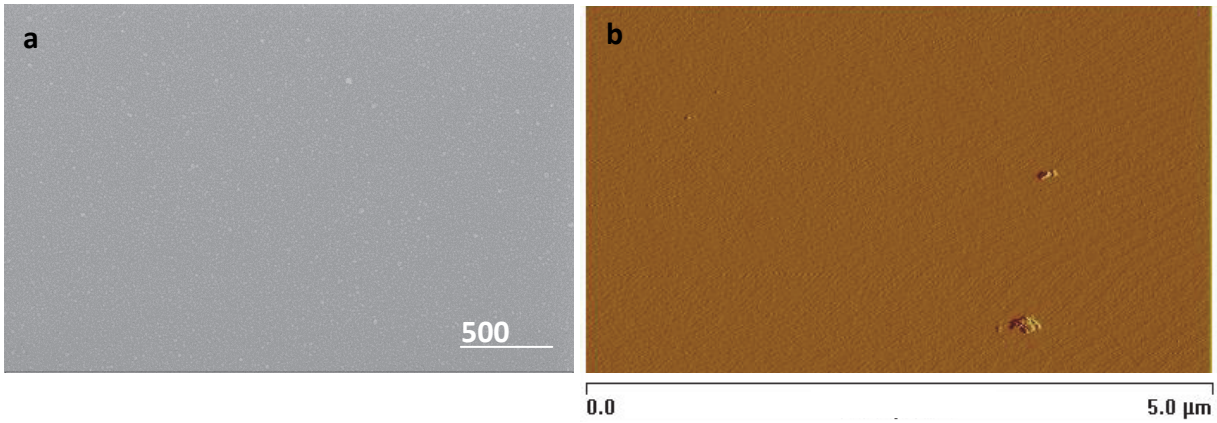

Figure 3.3. Images of the control (MPA only sensitized) surface a) SEM; b) AFM

3.2.7 Photocurrent Measurements

Full details of the experimental setup are listed in Chapter 2. Comparisons between samples were made with incident photon to current efficiencies (IPCE) measured in a three electrode electrochemical cell. Prior to photocurrent measurement, the potentiostat was switched on, sample illuminated, and a data collection delay time was introduced. Once the system reached a stable photocurrent (equilibrium) the autolab interface was used to record data. The photocurrent readings were not corrected for either cell/electrolyte absorbance or reflectance.

3.3 Results and Discussion

3.3.1 Optical Analysis of Solutions

UV-Vis spectroscopy was used to monitor the QD sensitization solutions throughout QD purification. General features of the UV-Vis absorption spectra were found to remain constant throughout (Figure 3.4). Thus, as evidenced by no change in the scattering of the solutions QD size and QD agglomeration remain constant. Analysis of the spectra by fitting to the mathematical sizing curve described by Peng *et al.* give an estimate for the QD size of *ca.* 3 nm diameter.[10]

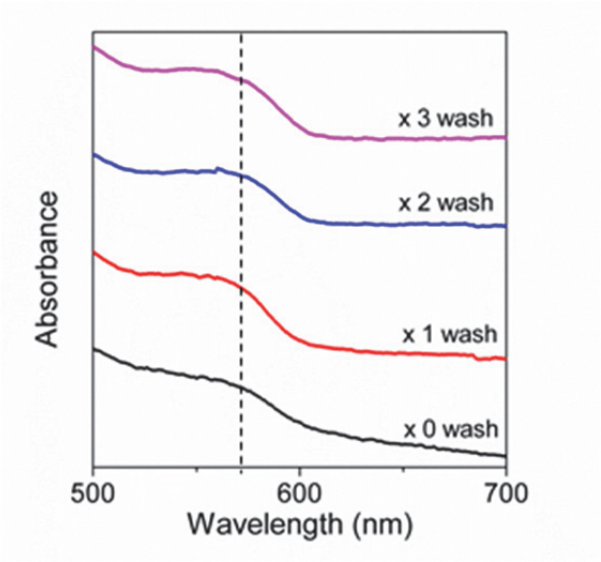

Figure 3.4. UV-Vis absorbance spectra of the four sensitizing QD solutions. The spectra are offset for clarity. A dashed line has been added to ease comparison of data sets.

A typical photoluminescence spectrum (and hence approximate QD size distribution) is shown in Figure 3.5. The FWHM of the sol is approximately 70 nm.

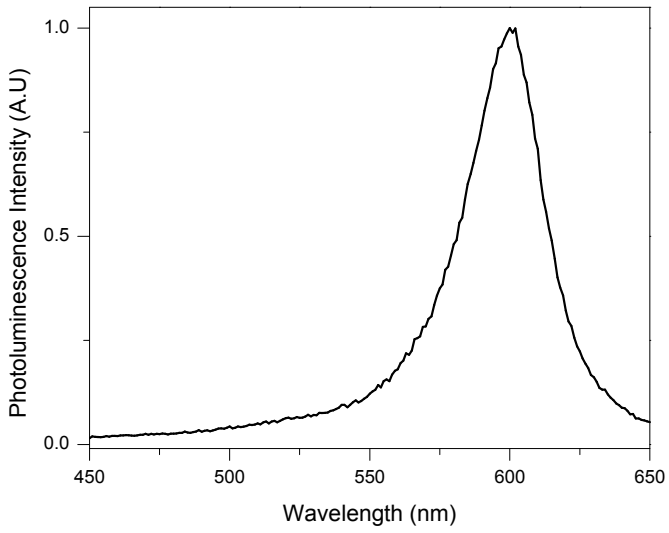

Figure 3.5. A typical photoluminescence spectrum of a QD sol used to sensitize the photoanodes.

3.3.2 Chemical Analysis – The QD Population of the TiO_2 Film

The ICP-OES results are shown with respect to QD purification in Figure 3.6. It is evident that as the QD purification proceeds the concentration of cadmium (Cd) atoms in the samples increases. The increased Cd concentration (normalized by the titanium (Ti) concentration) confirms an increased level of QD sensitization of TiO_2. With respect to the evolution of the surface chemistry throughout the QD purification,[5] we credit the increased sensitization to the reduced number of ligands present at the surface of the QD and hence enhanced ability for the attachment of the bifunctional linker molecule between the QD and TiO_2. Alongside consideration of the evolution of the morphology of surface bound QDs, the influence of this enhanced QD population on the photocurrent of sensitized TiO_2 is investigated below.

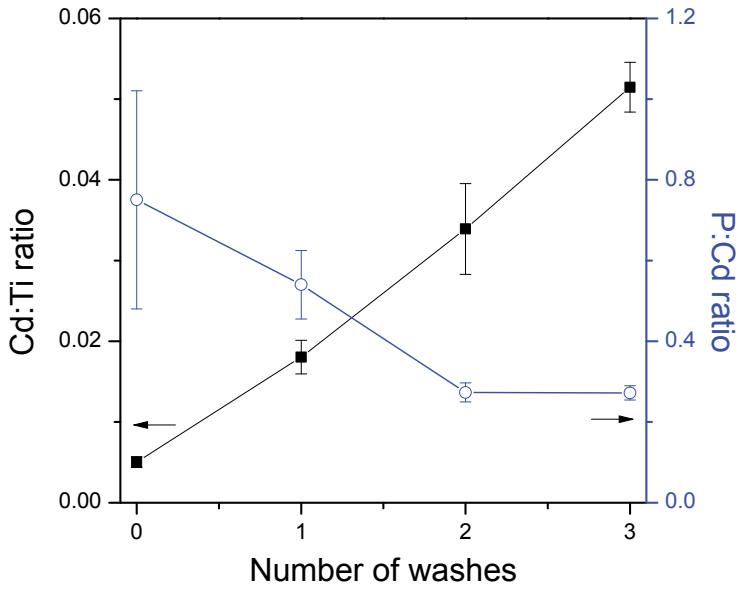

Figure 3.6. ICP-OES determined Cd:Ti (black) and P:Cd (blue) ratios plotted with respect to the number of washes of the sensitization QD solutions.

Most ligands known to bind to the surface (detailed in Table 3.1) of the QDs (including impurities from TOPO) contain phosphorous (P).[5] ICP-OES was therefore also used to monitor the elemental ratio of P:Cd atoms in the QD sensitized TiO_2 films. Figure 3.6 shows a decrease in the relative number of phosphorous atoms per QD between samples 0 wash to 2 wash. The decrease is accredited to either/both the loss of free ligands present in the QD sensitization solutions and the loss of bound ligands from the surface of the QD up to 2 wash.

To establish which of the QD sols contain free ligand ^1H NMR spectra was collected. NMR spectra of free TOPO is known to contain sharp peaks assigned to CH_3 group which have been shown elsewhere[2] to broaden upon the binding of ligand to the CdSe surface. The NMR spectra are shown in Figure 3.7. Here we observe the presence of the CH_3 only in the 0 wash sol. We therefore consider this evidence that purification removes the majority of unbound TOPO ligand from the sol. In combination with the ICP-OES data it can therefore be concluded that the decrease in P:Cd ratio from x 1 to x 2 samples is due to the loss of ligands bound to the QD surface.

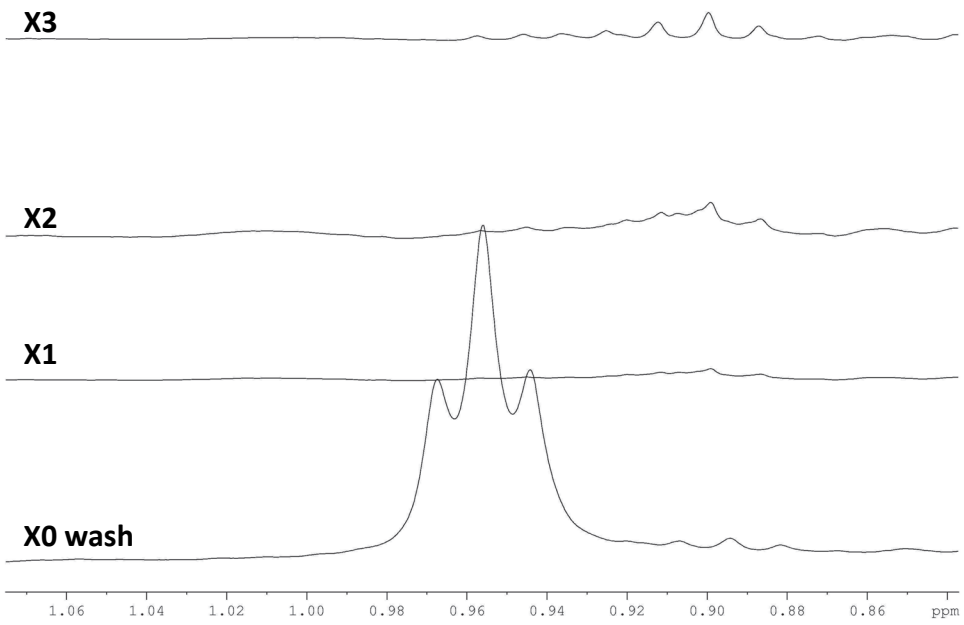

Figure 3.7. ^1H NMR data of the QD sols 0 washed, 1, washed 2 washed and 3 washed.

The ratio of P:Cd remains approximately unchanged from sample 2 wash to 3 wash and thus, the ratio of phosphorus containing ligands remains constant from 2 washes

onwards whilst the number of QDs absorbed on the TiO_2 continues to increase. It is thus determined that after the second purification of the QD solution enhanced sensitization is no longer due to a reduction in the number of *phosphorous* containing ligands. This is discussed further with respect to photocurrent measurements presented below. Using the unit cell dimensions of Wurtzite CdSe,[11] the number of P atoms per 3 nm QD is estimated to be ~75 after three washing cycles. It is therefore calculated that there is one P atom for every ~40 $Å^2$ of QD surface area. Although these results do not enable the distinction between the differing types of P containing ligands, (e.g. X- and L- type) consideration of the size of the typical ligands found in "TOPO" QDs enables some conclusions to be drawn. A schematic of two common QD ligands, TOPO (L-type) and OPA (X-type) are shown in Figure 3.8. Both molecules bind to the QD surface by the phosphate head group, however, the molecules occupy very different surface volumes. For example, the tri-alkyl chain molecule TOPO contains one phosphorous atom and occupies a significantly larger area (~0.25 nm^2 at the alkyl end) than the single alkyl chain ligand n-octylphosphonate OPA (< 0.01 nm^2 at the alkyl end). Thus, a greater number of the single alkyl chain ligands are able to occupy the same QD surface area relative to TOPO. Considering 3 nm QD surface area and the size of the ligands, the surface must therefore be predominantly populated with single chain ligands. It is, however, of note that not all ligands found at the surface of the QD contain P (for example, hexadecylamine) and these calculations are therefore only considered an indication of the level of QD ligand coverage.

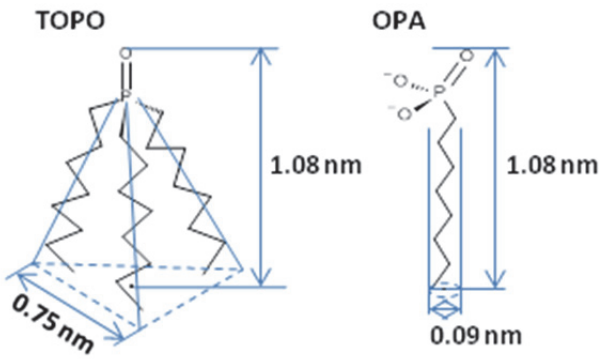

Figure 3.8. Schematic of the approximate dimensions of trioctylphosphine oxide (TOPO), and *n*-octylphosphonate (OPA).

3.3.3 Morphology of the QDs – SEM and AFM Imaging

To study the morphology and population of surface bound QD aggregates adsorbed at a surface SEM and AFM imaging was conducted. Sensitized onto single crystal Si (111) the typical images observed for each sample are shown in Figure 3.9. The number and size of surface bound agglomerates is shown to evolve with purification of the QD sensitization solution. Upon enhanced purification of the QD solutions, the number of surface bound agglomerates (visible by SEM and AFM) increases whilst the size of these features decreases. Through NMR spectroscopy (Figure 3.7), the sensitization solutions purified beyond 0 wash were shown to contain no free ligand (i.e. ligands not attached to the QD surface). It can therefore be assumed that the agglomerates imaged by SEM and AFM for samples 1 wash, 2 wash and 3 wash are composed of QDs and surface bound ligands only.

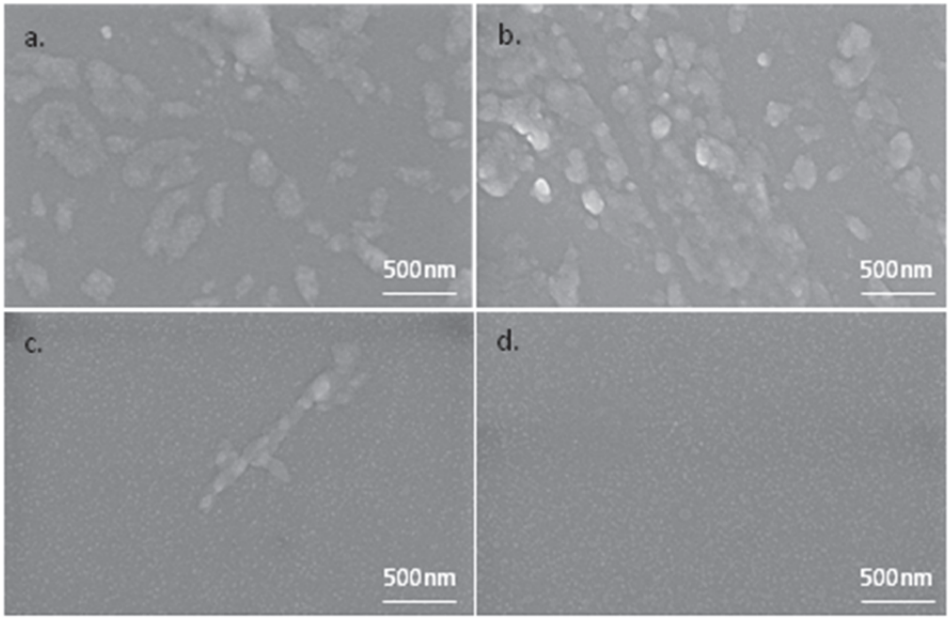

Figure 3.9. SEM images of typical morphology of QDs (at different stages of purification) adsorbed to a Si surface. (a) "0 washed", (b) "1 washed", (c) "2 washed" (d) "3 washed". The control is shown in Figure 3.3.

0 washed QD samples are sensitized in the presence of excess organic surfactant (ligands). It is known that the functional phosphonate group of unbound ligands will bind preferentially (relative to carboxylate groups of the 3-MPA linker molecule) at a TiO_2 surface.[12] Figure 3.9.a. was prepared with excess ligands present in the QD

solution. Excess ligands present are known to bind to the TiO_2 surface thus potentially block QD sensitization, hence, conversely to Figure 3.9.b – d, a lower surface coverage is observed.

3.3.4 Photocurrent Studies

The influence of purification on the QD sensitization of TiO_2 was also investigated by photocurrent measurements (Figure 3.10). With increased purification of the QD sensitizing solution the photocurrent from a sensitized TiO_2 film is enhanced. Specifically the photocurrent is enhanced by approximately 300 % IPCE across 0 wash to 3 wash QD films with respect to purification of the QDs. Thus the purification of "TOPO encapsulated" CdSe QDs has significant control on the ability of the QD to bind to a surface and thus the effectiveness of a photoanode in a quantum dot sensitized solar cell.

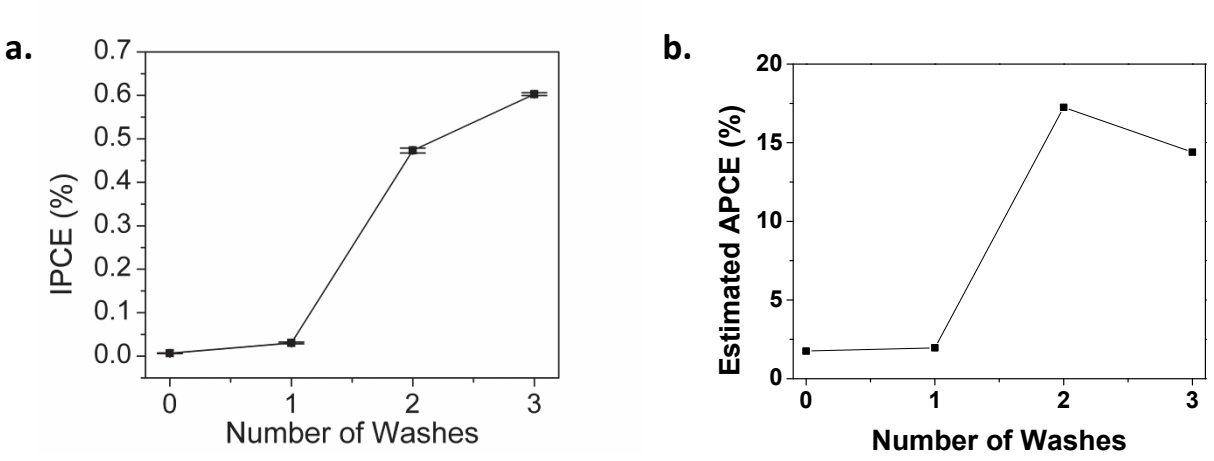

Figure 3.10. (a) The dependence of photocurrent (IPCE at 500 nm) on purification (number of washes). It is apparent that the photocurrent increases as purification of the QD sensitization proceeds. The error bars represent the distribution of results from the mean value. Each anode was sensitized by one of the four QD solutions ("0 wash", "1 wash", "2 wash" or "3 wash"). (b) The dependence of the estimated APCE on purification (number of washes). Photocurrent data was collected at 0 V against a silver/silver chloride reference electrode without the lock-in amplifier/optical chopper.

To determine whether the increase in photocurrent is entirely due to the enhanced level of QD sensitization, the dependence of photocurrent on abundance of QDs (ICP-OES results) was considered. A 300 % enhancement of IPCE values is recorded between x 0 and 3 washes whilst only a 10 % increase in QD coverage (Cd:Ti ratio) is observed. Evidently, if purification solely determines the number of QDs that attach to the TiO_2 surface a linear, positive dependence is predicted. It is most likely that several factors evolve alongside QD population contributing to the photocurrent and thus the true nature of the trend is non-linear. These factors and considerations are discussed below.

Initially, we examine photoanodes sensitized by the 0 wash QD solutions. Here, it is interesting to compare our results with those of Sambur *et al.*[7] who studied the influence of purification on sensitization of QDs to a single crystal TiO_2. In their photocurrent measurements, it was concluded that the presence of excess organic surfactant significantly deteriorated photocurrent IPCE levels. However, their results were not quantitatively correlated to surface coverage, rather they suggest that the small photocurrent signals is due to the first layer of QDs closest to the TiO_2. Here, we affirm the assertion that the presence of excess organic surfactants deteriorates the IPCE of the QDs adsorbed at the TiO_2 surface. As observed by SEM imaging, it is noted that surfaces sensitized by 0 wash and 1 wash QDs are populated with a few large agglomerates. These agglomerates are large in width and height (relative to agglomerates at the 3 wash). In particular, the large height of such agglomerates increases the distance an electron must travel to photoinject into the TiO_2 and hence in part, explains why lower IPCEs are recorded for photoanodes sensitized by QDs with 0 wash and 1 wash QDs. It is also apparent that where a sensitizing QD solution contains bulky agglomerates of QD and organic surfactant, upon attachment to the surface an agglomerate may block the entrances to nanopores within the TiO_2 structure, thus preventing complete QD surface coverage and reducing the IPCE of a photoanode. This assertion is confirmed upon comparison of the (estimated) APCE values of the films prepared (Figure 3.10(b)). APCE is significantly enhanced from 1 wash to 2 wash, thus affirming the enhanced ability of the sensitized films is due to the nature of the sensitized QD rather than QD population.

Sensitizing solutions of higher purification (1 wash, 2 wash and 3 wash) do not contain excess organic ligands (as verified here by NMR, Figure 3.7). Upon the removal

of excess ligands from solution during purification the dynamic equilibrium between bound and non-bound L-type ligands shifts. Consequentially, with increased purification, surface bound ligands dissociate and are not immediately replaced leaving reactive QD surface sites exposed as depicted in Figure 3.11. Our results suggest that the removal of excess ligands (from both the QD surface and solution) increased the number of reactive QD surface sites and therefore enhanced the sensitization of QDs to 3-MPA bifunctional linker molecules. ICP-OES and photocurrent analysis in combination with the AFM images verify our previous assertion that the smaller aggregates are better suited (with respect to size) to fully populate the TiO_2 nanoporous surface and hence enable a higher level of surface coverage. It seems appropriate to speculate that the smaller QD aggregates are on average closer to the TiO_2 surface and hence more QDs are able to inject into the TiO_2 conduction band – as verified by IPCE measurements.

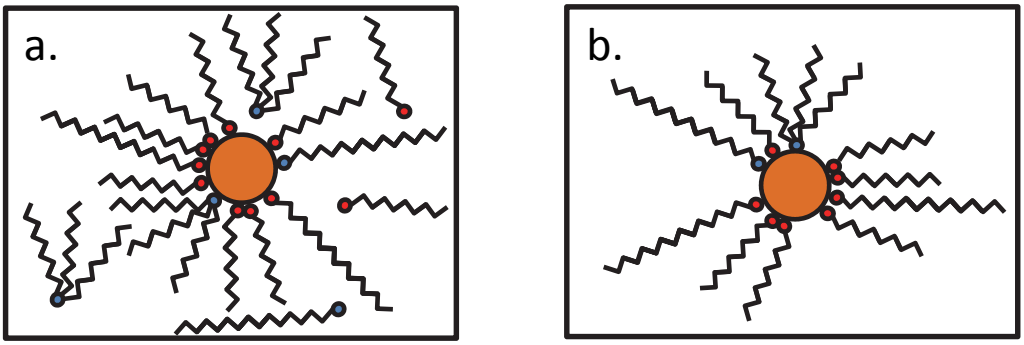

Figure 3.11. Schematic representing the evolution in surface bound ligands with respect to purification for (a). 0 wash and (b) 3 wash QDs. X-type ligands are represented with a red head group; L-type ligands blue.

Whilst the surface bound QD population increases from samples 2 wash to 3 wash, the level of phosphorous remains approximately constant (Figure 3). This enhanced QD sensitization therefore cannot be due to the removal of phosphorous containing ligands. Figure 7, examines the IPCE of samples normalized by the ratio of Cd:Ti (number of QD at the surface) with respect to the number of purification cycles. It is of note that despite the enhanced QD population from sample 2 wash to 3 wash there is no enhancement in the relative IPCE and APCE (rather, a decrease). Kalyuzhny and Murray demonstrated that increased QD purification introduces defects states (such as surface

trapped emission states) due to the removal of surface Cd atoms and that the presence of surface traps is also correlated to the aging of QD solutions.[2] We therefore propose that the decrease in APCE is due to the removal of non-phosphorous containing ligands (impurities sourced in the 90 % technical grade TOPO, or HAD). It is, however, evident from the photocurrent results presented here that the net increase in the IPCE level upon enhanced purification of QDs outweighs any loss of efficiency due surface trap states.

Chemical analysis (ICP-OES) of samples prepared by QDs sensitized at a TiO_2 surface demonstrated that enhanced purification of QD sensitization solutions facilitates a higher population of QDs to adsorb at the TiO_2 surface. In comparison with the morphologies reported here, we infer that this trend is due to the evolution of the size of surface bound QD agglomerates. Surfaces prepared from "0 wash" and "1 wash" are populated by large agglomerates which upon sensitization to porous TiO_2 surface can block pores from further sensitization. Conversely, agglomerates observed at the surface of samples prepared with "3 wash" QDs are sufficiently small in size to adsorb to the TiO_2 without perturbing further sensitization at the surface.

3.4 Conclusions

A systematic study on the influence of QD purification on the QD surface population and morphology is here compiled demonstrating the importance of a quantified QD purification with respect to construction of a photoanode. Through a combination of chemical analysis, SEM and AFM imaging, the concentration, size and shape of sensitized QDs agglomerates sensitized at a surface has been shown to evolve with purification. Specifically, QD purification is shown to promote the adsorption of QDs to a surface (an enhanced population observed). The QDs are shown to agglomerate upon adsorption. Imaging revealed the significant decrease (~100 fold) in size of agglomerates with respect to purification. The results conclusively demonstrate that as the QD surface chemistry evolves the ability of the QD to attach to a surface is enhanced. Through photocurrent measurements, the ability of QDs agglomerates to photoinject has been correlated to the evolution of QD agglomeration; smaller sized aggregates are better able to photoinject. The implications of this study are particularly important with respect to the performance of QDSSCs.

3.5 References

(1) Ruhle, S.; Shalom, M.; Zaban, A. *ChemPhysChem* **2010**, *11*, 2290.

(2) Kalyuzhny, G.; Murray, R. W. *Journal of Physical Chemistry B* **2005**, *109*, 7012.

(3) Guijarro, N.; Lana-Villarreal, T.; Mora-Sero, I.; Bisquert, J.; Gomez, R. *Journal of Physical Chemistry C* **2009**, *113*, 4208.

(4) Wang, F. D.; Tang, R.; Buhro, W. E. *Nano Lett.* **2008**, *8*, 3521.

(5) Morris-Cohen, A. J.; Donakowski, M. D.; Knowles, K. E.; Weiss, E. A. *Journal of Physical Chemistry C* **2010**, *114*, 897.

(6) Owen, J. S.; Park, J.; Trudeau, P. E.; Alivisatos, A. P. *Journal of the American Chemical Society* **2008**, *130*, 12279.

(7) Sambur, J. B.; Riha, S. C.; Choi, D.; Parkinson, B. A. *Langmuir* **2010**, *26*, 4839.

(8) Robel, I.; Subramanian, V.; Kuno, M.; Kamat, P. V. *Journal of the American Chemical Society* **2006**, *128*, 2385.

(9) Mora-Sero, I.; Gimenez, S.; Moehl, T.; Fabregat-Santiago, F.; Lana-Villareal, T.; Gomez, R.; Bisquert, J. *Nanotechnology* **2008**, *19*, 7.

(10) Yu, W. W.; Qu, L. H.; Guo, W. Z.; Peng, X. G. *Chemistry of Materials* **2003**, *15*, 2854.

(11) Wyckoff, R. W. G.; John Wiley & Sons: New York, London, 1963; Vol. 1.

(12) Bae, E.; Choi, W. *Journal of Physical Chemistry B* **2006**, *110*, 14792.

Chapter 4. The Influence of Polysulfide Electrolyte on CdSe QDs

4.1 Introduction to the Electrolyte

The role of the electrolyte redox couple in QDSSCs is to electrochemically connect the photoanode with the counter electrode. As detailed in Chapter 1, the general operation of a sensitized solar cell is that the semiconductor (QD) absorbs a photon which excites an electron-hole pair. The electron is injected into a wide band gap mesoporous substrate (TiO_2) and subsequently into conductive glass. Thus a hole remains in the QD which is regenerated by a reducing species in the electrolyte which transports the hole across the cell to a counter electrode where the species is oxidized and thus the circuit complete. The electrolyte must therefore scavenge the photogenerated holes (inject electrons) at the photoanode.

The most common electrolyte utilized in dye sensitized solar cells (DSSC) is the iodide/triiodide (I^-/I_3^-) redox couple. The success of the redox couple is due to a combination of factors including the relatively slow kinetics of electron transfer from TiO_2 and the oxidized sensitizer (dye) to the triiodide species (recombination) leading to long-lived electron lifetimes of 1 ms – 1 s.[1,2] Another reason for the success is the small size of the redox species which enables the relatively fast diffusion of the species within the mesoporous TiO_2 structure. It is also of note that when iodine oxidises (regenerates) the dye molecule, the iodine forms an ionic intermediate species ($I_2^{-\cdot}$) which subsequently disproportionates (with another $I_2^{-\cdot}$) to form triiodide (I_3^-).

Despite the success of the iodide/triiodide electrolyte there are many limitations of the electrolyte such as corrosion of cell components (e.g. cell sealants and metals connections) as well as strong light absorption by the electrolyte solution (hence the solution competes with the dye for incident photon). Very few QDSSC devices have been prepared utilizing iodine/triiodide electrolyte due to the corrosive nature of the electrolyte towards CdS and CdSeQDs.[3]The need for alternative electrolyte redox couples has therefore been highlighted for QDSSCs. Several factors need to be considered when seeking an alternative electrolyte including; the redox potential, aqueous/non aqueous suitability (in particular this influences the industrial application

of a cell), as well as cell stability and the reversibility of the redox couple. Examples of electrolytes such as ferricyanide-ferrocyanide ($Fe(CN)_6^{4-}$/ $Fe(CN)_6^{3-}$), cobalt (Co^{2+}/Co^{3+}) and organic based electrolytes such as a thiourea based redox couple[4]have been highlighted as possible replacements for the iodide/triiodide electrolyte as discussed in Chapter 1. Throughout the PEC and QDSSC literature polysulfide (S^{2-}/S_n^{2-}) electrolyte has most commonly been utilized. Here, a brief overview of polysulfide and its influence on photoelectrode and relevant solar cells is presented.

4.1.1 Polysulfide Electrolyte

When sodium sulfide is dissolved into an aqueous medium the sulfide ions predominantly exist as HS^- ions as dictated by the following equilibrium;

$$S^{2-} + H_2O \leftrightarrow HS^- + OH^- \quad (4.1)$$

The fact that the equilibrium of reaction 4.1 lies to the right is illustrated by the observation that a 0.1 M aqueous Na_2S solution has a pH of 13 such that SH^- ions dominate the solution. When sulfur is dissolved in the presence of sodium sulphide, various hydrolysis and complexation reactions occur (below) forming polysulfide species denoted S_n^{2-} where typically n = 2 – 5.[5]

$$nS + S^{2-} \rightarrow S_n^{2-} \quad (4.2)$$

Thus the polysulfide redox couple is generally written as:

$$nS^{2-} \leftrightarrow S_n^{2-} + (n-2)e^- \quad (4.3)$$

The exact redox couple is known to vary with the exact electrolyte composition, concentrations and solution pH.[5-7] Hence, the aqueous polysulfide redox couple (S^{2-}/S_n^{2-}) is chemically very complex, and remains poorly defined with respect to chemical potential.[5,8] The electrolyte is also limited with regards to stability by its gradual disproportionation of polysulfide species to sulfide and oxosulfur species.[9] Despite the limitations, polysulfide electrolyte remains the most popular redox couple for many

solar cells due to its ability to support a high open circuit voltage and the acclaimed stability during solar cell operation.[10,11]

4.1.2 Polysulfide Cadmium Selenide Photoelectrochemical Cells

Due to the suitability of their band gaps for solar photon harvesting, (≤2.4 eV) cadmium chalcogenides (CdX where X = S, Se or Te) have attracted significant attention as photoelectrodes in photoelectrochemical cells (PECs) since early work began in the 1970s.[10,12-18]Throughout the literature polysulfide electrolyte has been commonly utilized in cadmium chlcogenide based PECs. In the 1970-80s, there were, however, several studies into the stability of the CdSe/polysulfide cell. Inconsistent reports of stability (ranging from the minute to month timescale) were finally accredited to differences in crystal structure and face, electrolyte composition and photocurrent density.[19] It was shown that "stabilization" of the photoanodes corresponded to a light induced surface substitution reaction. Through elemental analysis, it was demonstrated that under illumination the cadmium (Cd) concentration of the electrolyte was constant,[15]conversely, as verified by XPS, selenium (Se) concentrations at the surface of the bulk crystal were shown to decrease. The intensity of sulphur (S) levels was shown to increase simultaneously.[20,21]Thus a selenium/sulfur (Se/S) substitution mechanism was proposed in which the top layer of CdSe is gradually replaced by CdS. The thickness of the substituted CdS layer at the surface of the photoelectrode was estimated to be of the order of tens to hundreds of Angstroms.[19,20] Stable cell photocurrents were proposed to correlate with the quenching of the substitution layer.

The proposed mechanism for Se/S substitution is shown below. In summary; upon absorbance of two photons CdSe forms two electron hole pairs which can lead to the dissolution of the Se resulting in the formation of Cd^{2+}. Due to the high concentration of S^{2-} in the electrolyte solution Cd^{2+} will re-precipitate with S^{2-} adsorbed at the crystal surface forming CdS. Thus the overall reaction is the replacement of CdSe with CdS.

$$2hv \xrightarrow{CdSe} 2e^- + 2h^+ \tag{4.4}$$

$$2h^+ + CdSe_{(s)} \rightarrow {Cd^{2+}}_{(s)} + Se_{(aq)} \tag{4.5}$$

$$Se_{(aq)} + S^{2-}{}_{(aq)} \rightarrow SSe^{2-}_{(aq)} \quad (4.6)$$

$$Cd^{2+}{}_{(s)} + (S^{2-})_{(ads)} \rightarrow CdS_{(s)} \quad (4.7)$$

4.1.3 Polysulfide Cadmium Selenide Quantum Dot Sensitized Solar Cells

Throughout the CdSe QDSSC literature the polysulfide redox couple is most commonly utilized as the electrolyte. This is commonly attributed to the large photovoltage and stability of the cell. There have, however, been a few reports of a spectral mismatch in the onset of the optical absorbance and photocurrent IPCE of the QD and QDSSCs respectively.[7,22] In both of these reports a redshift in the QD sensitized photoelectrode photocurrent spectra by up to 25 nm relative to the onset of the QD absorbance was recorded post exposure to polysulfide electrolyte. Analogous to the 1970s bulk CdSe/polysulfide literature, discussions and proposed S/Se substitution mechanisms were suggested for CdSe QD (Eqs (4. 4) - (4. 7)). This was suggested on the basis of SEM-EDX elemental identification of sulfur in the QD sensitized photoanode post polysulfide exposure only.

4.1.4 Quantum Dot Only Photoelectrodes

QD films coated on conductive substrates have been realised for potential applications in solar cells.[23] Similarly to the operating principles of QDSSCs, upon absorbance of a photon in the QD an exciton is produced in the photoelectrode. The exciton is subsequently separated, the electron/hole extracted at electrodes at opposite ends of the cell and thus photocurrent is produced. Electrons/holes can be extracted by the FTO front contact whilst holes/electrons are extracted by a metal contact or electrolyte solution. To date, such devices have attracted significant attention due to the ease of solution processable preparation (by drop-casting[24] and spin coating[25]) of the QD films. PbS and PbSe QDs have attracted particular attention in this field due to their small bulk bandgaps which enable tuneability of absorbance across the visible *and* infrared regions of the solar spectrum.[26,27] This is particularly attractive for application in triple-junction photovoltaics where power efficiencies are significantly enhanced by

absorbance across the entire solar spectrum and hence these materials and types of devices have recently attracted significant attention.[23,26]

The operation of QD photovoltaic devices is considered similar to p-n semiconductor junctions, however, contrary to continuous photoactive films there are some differences in films composed of QDs as reviewed here. Primarily, the discrete structure of QDs (typically an inorganic core surrounded by an insulating organic capping layer) is retained in the QD film such that carriers (excitons) remain within the QD rather than delocalized within a bulk film. The mechanisms for electron transfer in QD films are therefore quantum tunnelling (between QD states) and hopping (between QD states and surface trap states) rather than diffusion within the bulk crystal.

Since the introduction of QD only photovoltaic devices, there have been several advances in solar cell performance. These advances to higher efficiencies have largely been attributed to the shortening of the distance between QDs, cross-linking between QDs and recombination site (defect) passivation.[28] Of particular relevance to this thesis, many of these advances have involved surface treatments with thiols.[24,28-31] In particular, the replacement of as-synthesised surface bound organic capping layer with thiol ligands was shown to significantly increase the depletion width of a device whilst simultaneously reducing the number of trap states (passivated by thiol attachment). Similarly, surface passivation by halide ligands has also been found to reduce the density of trap states producing the highest certified QD device efficiency to date (December 2012) of 5.1 %.[32]

The work presented in this chapter was conducted with a view to understanding the role of polysulfide electrolyte in CdSe QD electrodes. Characterisation was performed with a view to verifying and providing an explanation for the influence of polysulfide electrolyte on QD, and QD sensitized TiO_2 films.

4.2 Experimental

4.2.1 Materials

Quantum dots were prepared and purified as outlined in Chapter 2. Polysulfide solution was prepared with sodium sulfide nonahydrate ($Na_2S.9H_2O$, > 99.99 %, Aldrich) and sulphur powder, (S, sublimed, ~100 mesh, 99.5%, Alfa Aesar).The

electrolyte (hole scavenger) used for photocurrent measurements was aqueous 0.5 M sodium sulphite (Na_2SO_3, ≥ 98 %, Sigma-Aldrich).

TEC8 glass plate fluorinated tin oxide (FTO) coated glass slides (1 x 2.5 cm) (Dyesol) were used as optically transparent electrodes (OTE). Hydrochloric acid (HCl, 37 %, VWR), nitric acid (HNO_3, 68 %, BDH), sulfuric acid (H_2SO_4, 95 %, VWR) and hydrogen peroxide (H_2O_2, 30 %, Fischer Scientific) were used in the cleaning procedure of the FTO. Single crystal (undoped)<0001>CdSe (Semiconductor Wafer, Inc.) were used as received.

Calibration standards and sample solutions for ICP-OES measurements were prepared using S (1000 mg/L S in 2% HNO_3, Fluka Analytical), Cd (1000 mg/L Cd in 2 % HNO_3, Fluka Analytical), Se (1000 mg/L Se in 2% HNO_3, Fluka Analytical) and nitric acid (HNO_3, 70%, Fisher) and concentrated hydrochloric acid (HCl, 36 %, VWR).

One batch of QDs was utilized for all of the experimental work presented in this chapter. The average diameter of the QDs was 3.3 nm (estimated from the excitonic peak position determined by absorbance spectroscopy of the QD soln Figure 4.13[33]).

4.2.2 Preparation of Cadmium Selenide Quantum Dot Photoanodes

A concentrated CdSe QD paste was prepared by centrifugation of the QD soln and re-dispersion in a 1 ml toluene and 1 ml ethanol mix. 15 µL of QD soln was used to prepare films on the clean, conductive fluorine doped tin oxide (FTO) using the doctor-blade technique. Samples were left to dry in the dark for >24 hours prior to further measurement.

4.2.3 Preparation of Cadmium Selenide Quantum Dot Sensitized Titanium Dioxide Photoanodes

The linker molecule 3-mercaptopropionic acid (3-MPA) was utilized to sensitize the QDs at the surface of the TiO_2. 5 ml of 1 M 3-MPA (acetonitrile) was added to 0.15 g P25 Degussa TiO_2 powder. The solution was left to stir for >12 h. The solutions were then washed with excess acetonitrile, centrifuged, the QD-TiO_2 pellet dried, re-dispersed in toluene and re-separated from solvent by centrifugation. 4.38 mol of CdSe QDs was then added to TiO_2 with 5 ml of toluene and left to stir for >4 days. Upon addition of a

further 5 ml toluene the solutions are left to stand and separate (QD-TiO_2 orange solid settles at the bottom of the vial). The transparent supernatant was then extracted by pipette. To each of the samples 4.4 ml of ethanol was added and left to stir vigorously for >12 h. 15µL of each sample were used to prepare films on the clean, conductive fluorine doped tin oxide (FTO) using the doctor-blade technique. Figure 4.1 shows a schematic representation of the preparation of the QD sensitized photoanode. The films were pressed in an isostatic press at 30 MPa for 30 s.[34] Between measurements, all QD solutions and electrodes were stored in the dark.

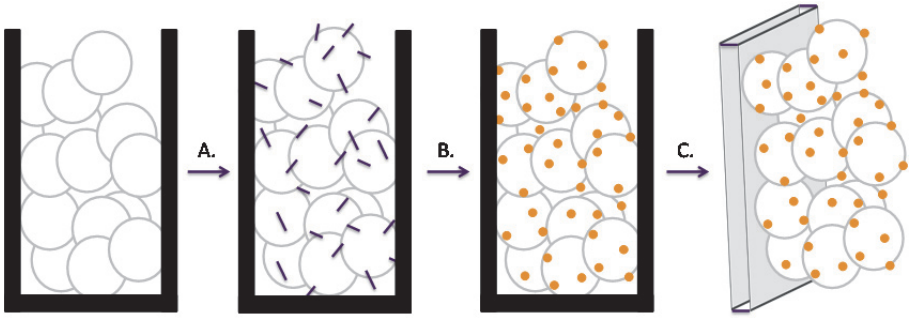

Figure 4.1. Schematic for the three step sensitization of TiO_2 for the preparation of photoanodes. A. Addition of 1 M 3-MPA to the TiO_2 particles. B. Addition of QD soln. C. Doctor bladed QD-3-MPA-TiO_2 onto FTO conductive glass and pressed.

4.2.4 Polysulfide Treatment

Samples subject to "polysulfide treatment" were prepared on FTO and then submersed in a 0.1 M Na_2S and 0.1 M S solution for 30 mins. Treated films were subsequently rinsed of excess polysulfide by repeated submersion in distilled water. For each set of characterisation/analysis (except photocurrent measurements) one CdSe film was prepared and cut in half; one half was exposed to polysulfide solution, the other left untreated. For the photocurrent spectra, untreated films were firstly measured; the sample was then treated with polysulfide solution; finally the photocurrent spectra were re-recorded.

4.2.5 SIMS

SIMS was performed on single crystal CdSe films for both untreated and polysulfide treated samples.

4.2.6 ICP-OES

Three samples were prepared for ICP analysis; untreated CdSe film, polysulfide treated CdSe film, and an FTO control. Each sample was digested in 4 ml aqua regia solution (3 part concentrated hydrochloric acid : 1 part concentrated nitric acid) followed by 30 min of sonication. Two dilutions of each digested sample were prepared for ICP-OES analysis; 1 ml of digested sample with 9 ml 2 M nitric acid and 2.5 ml of digested sample with 7.5 ml 2 M nitric acid. Each solution was analysed for Cd, Se and S content against 0, 1, 5 and 20 ppm calibration solutions. The FTO sample was used as a baseline for each elemental composition and thus these baseline concentrations were subtracted from sample concentrations. The quoted values are averaged for the two dilutions prepared. Elemental ratios were calculated for data interpretation thus avoiding discrepancies due to sample size, area and thickness.

For selenium, accurate concentrations were not attained using ICP. Samples containing both carbon (sourced in the QD capping ligands) and selenium elemental concentrations are known to be difficult to decipher by ICP analysis. This is due to matrix effects in the ionization of selenium in the presence of carbon. Experimentally determined values of selenium were, however, confirmed to be proportioned to concentration and hence the *relative* elemental concentrations/ratios are valid.

4.2.7 SEM-EDX

SEM-EDX analyses were performed in 7 randomly selected regions across the surface of the untreated and polysulfide treated films.

4.2.8 Photocurrent Measurements

Photocurrent signals recorded on QD only films were sufficiently high to record without the lock-in amplifier. They were therefore recorded by photocurrent transients; at each wavelength a time delay was introduced such that the photocurrent was not recorded until the signal plateaued (Figure 4.2). The difference between the dark and light current was calculated and thus used for photocurrent efficiency calculation.

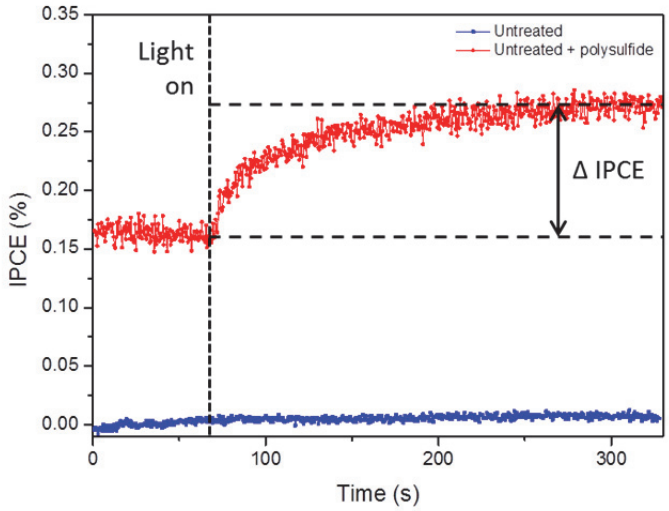

Figure 4.2. Photocurrent transient recorded in 0.5 M Na_2SO_3 at 0 V against a Ag/AgCl reference electrode illuminated at 560 nm. The black vertical broken line represents the time at which the light source was switched on. The plotted spectra are the photocurrent transients for the same QD only photoanode before (blue) and after (red) polysulfide treatment.

4.2.9 Optimization of the Photocurrent Spectra

To optimize the maximum photocurrent efficiencies a photoanodewith a stable photocurrent response (on the hour timescale) was used to determine the optimum sodium sulfite (hole scavenger) concentration and pH. Average efficiencies for the conditions were measured under 560 nm illumination and are tabulated in Table 4.1 and Table 4.2.

Concentration (M)	IPCE (%)
0.5	0.51
1.0	0.47

Table 4.1. IPCE for different concentrations of sodium sulfite solution (pH 7) measured under 560 nm incident illumination at 0 V against a Ag/AgCl reference electrode. The measurements were conducted without the optical chopper and lock-in amplifier.

It is evident that the sodium sulfite concentration has a minimal effect on IPCE. The dark current recorded for the samples was, however, significantly higher for the 1.0 M solution; thus 0.5 M was selected for subsequent measurements.

pH	IPCE (%)
6.8	0.58
9.0	0.24

Table 4.2. IPCE for two different pH of sodium sulfite solution (0.5 M) measured under 560 nm incident illumination at 0 V against a Ag/AgCl reference electrode. The measurements were conducted without the optical chopper and lock-in amplifier. The pH was adjusted using sulphuric acid.

Enhanced photocurrent efficiencies were measured for 0.5M sodium sulfite at pH 6.8 relative to pH 9.0. Therefore all subsequent experiments were performed at this pH. Fresh electrolyte was used on each day of measurement. The pH was monitored before and after photocurrent measurements to ensure all measurements were comparable.

4.3 Results and Discussions

4.3.1 Chemical Analysis

ICP-OES analysis was performed to determine the ratio of elemental concentrations of cadmium, selenium and sulfur for untreated and polysulfide treated CdSe films. Averaged composition ratios are detailed in Table 4.3.

Sample	Se per Cd	S per Cd
Untreated	0.23	0.00
Polysulfide treated	0.17	0.17

Table 4.3. Average elemental ratios for the dissolved untreated and polysulfide treated CdSe films. It is of note that the absolute concentration of selenium is unreliable due to problems with regards to ICP preparation. A constant ratio of selenium signal (relative to the real signal), however, enables comparative conclusions to be drawn.

The elemental ratios reveal a decrease in the selenium (Se) and an increase in the sulfur (S) content of the samples. Sulfur/selenium (S/Se) substitution and sulfur deposition into the QD films are therefore highlighted as possible reactions in polysulfide solution. Both Se/S substitution and sulphur (or sodium sulfide) deposition into/onto the film are therefore proposed here. With regards to the QD and QD film, several different chemical structures, compositions and morphologies are proposed as illustrated in Figures 4.3 and 4.4 respectively. On the nano-scale (QD) several possibilities are viable, each of which introduce sulphur into/at the surface of the QDs including the possible formation of either $CdSe_{x-1}S_x$ alloy or core/shell architectures.

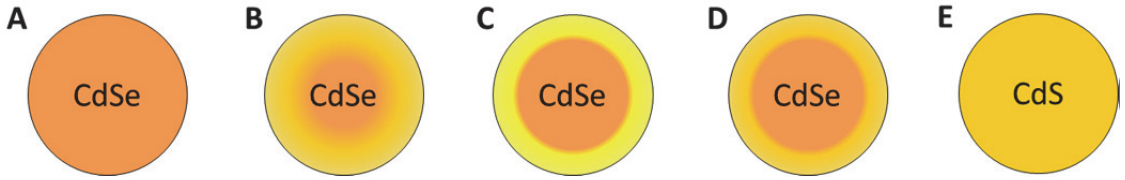

Figure 4.3. Schematic of proposed QD structures as a result of the polysulfide treatment. Note, no change in symmetry or size is detailed here. (A) CdSe QDs untreated. (B) $CdSe_{1-x}S_x$ QDs such that the QD surface has a greater population of CdS and the centre remains CdSe. (C) CdSe coated/capped by a sulfur layer. (D) CdSe core with CdS shell; selenium/sulfur substitution at the edge of the QD. (E) CdS only; complete selenium/sulfur substitution leaving.

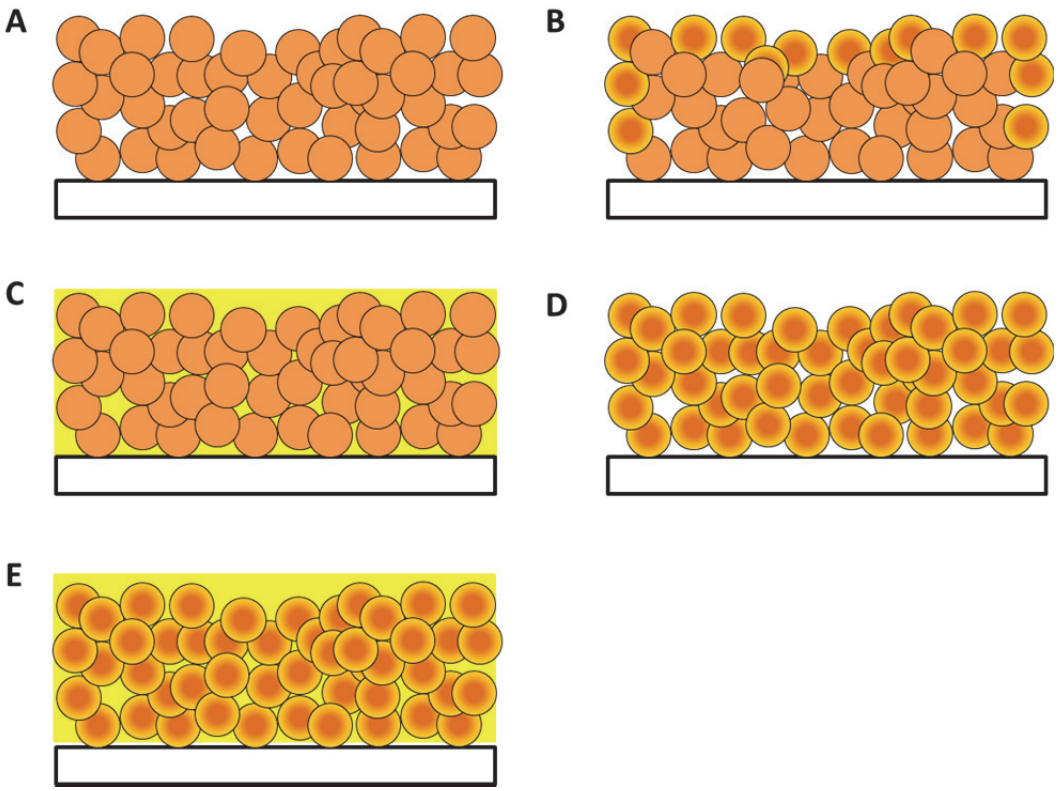

Figure 4.4. Schematics of proposed possible influences of polysulfide on QD only films. (A) Untreated CdSe film. (B) Sulfur substitution in the surface bound QDs only (as detailed in Figure 4.3). (C) Sulfurization of pores within the QD film, no change to QDs. (D) A change in the chemical identity (as detailed in Figure 4.3) of all CdSe QDs. (E) A combination of both sulfurization of pores in the QD film and a change in the chemical identity of the QDs.

Given the unit cell of CdSe is wurtzite and the known diameter of the QD the number of atoms within an average QD can be estimated (~266 of each Cd and Se atoms). Assuming that the sulfide/polysulfide can potentially bind to the QD surface at Cd atoms only, it can be estimated that there are ~50 potential binding sites for each QD. If the sulfide binds as S^{2-} (rather than polysulfide species) the S per Cd atomic ratio is thus calculated at 0.19. This is indeed in relatively good agreement with the experimentally determined ratios determined by ICP-OES analysis (Table 4.3).

Chemical analysis was also performed on the QD films by SEM-EDX analysis of the elemental composition (Figure 4.5). Cadmium, carbon, chromium, oxygen, phosphor and selenium were detected in each of areas tested for the untreated sample. For the polysulfide treated samples, sodium and sulfur were detected in addition to the elements detected in the untreated sample. The presence of chromium is attributed

tothe chromium coating utilized for SEM imaging. Phosphor, carbon and oxygen are credited to the CdSe QDs and organic capping layer of the QDs; cadmium and selenium from the CdSe QD. Sulfur and sodium are sourced from the polysulfide electrolyte.

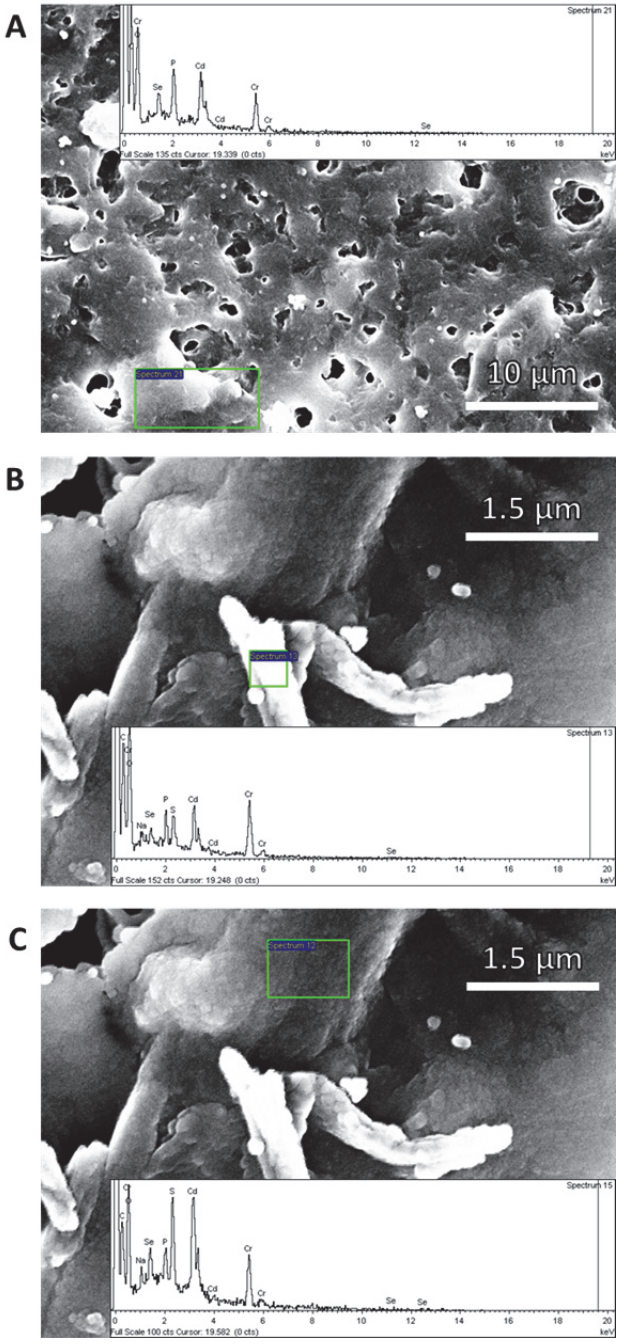

Figure 4.5. Typical examples of SEM and corresponding EDX of untreated (A) and polysulfide (B) and (C) polysulfide treated CdSe films. The areas analysed with EDX are shown in green boxes on each image.

Secondary ion mass spectroscopy (SIMS) was performed on the films before and post polysulfide treatment to investigate the depth dependent chemical content. Measurements were conducted on CdSe single crystals to avoid discrepancies in the measurement due to film morphology in the QD samples. Chemical depth profiles (plotted with respect to sputter time) are shown in Figure 4.6. In the negative mode (Figure 4.6 (a) and (b)), the sulfur intensity in treated films is significantly enhanced (by approximately 100 times) relative to the untreated sample. For the positive ion mode the sodium signal intensity is also slightly enhanced at the surface of the film in the treated sample. The intensity profiles for both the untreated and treated samples decay to approximately the same signal intensity and hence the enhanced sulfur content must reside in the sample surface and not the bulk crystal. The surface enhanced sulfur content is in agreement with the single and polycrystalline crystal studies conducted in the 1970s and thus verifies selenium/sulfur substitution as a contributing mechanism in the polysulfide treatment.[10,20,21,35,36]

With regards to extrapolation of the single crystal SIMS analyses to CdSe QDs it can be inferred that polysulfide treatment does indeed introduce sulfur into the surface of CdSe. Whilst here the signal intensity has not been resolved for depth (distance) it is noted that the bulk crystal remains unchanged in composition.

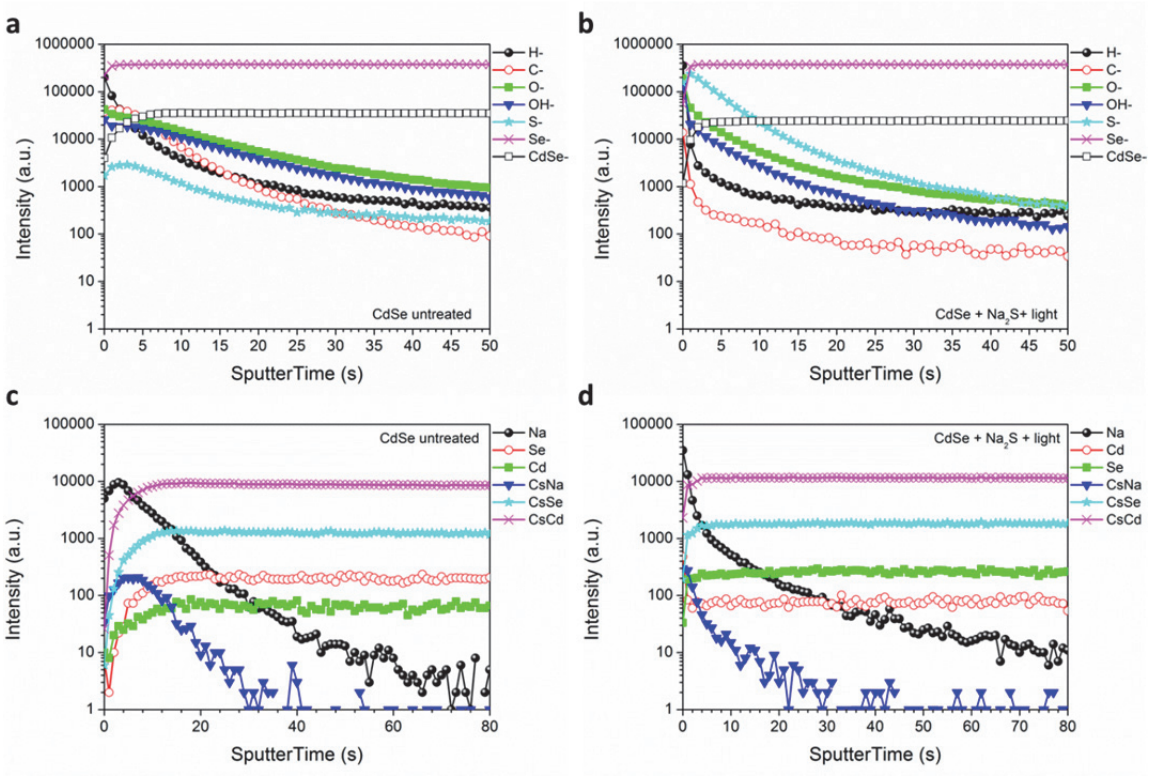

Figure 4.6. SIMS profiles for CdSe single crystal samples; negative (a) and (b) and positive (c) and (d) ions are shown separately. (a) and (c) profiles are for CdSe untreated samples; (b) and (d) for polysulfide treated CdSe samples.

To monitor the presence and structure of the organic capping layer of the CdSe QD films FT-IR was conducted (Figure 4.7). The difference between the spectra (pre and post polysulfide treatment) is minimal and thus verifies that the organic species present in the QD films remains unchanged with respect to chemical identity and structure. Given the close proximity of the surface bound organic capping molecules it is predicted that the bond vibration (and hence peak structure) corresponding to P=O (QD bound head group present in most of the capping ligands) should reflect the chemical identity of the QD surface identity. Unfortunately, due to the quantity and complexity of the spectra present in the samples the P=O stretch signal (expected 1085 – 1415 cm^{-1}) is not readily identified and thus conclusions cannot be inferred.

The magnitude of FT-IR peak is proportionate to the concentration of the species responsible for the signal. However, due to the sample holder/loading, delamination of the films was observed for these measurements and therefore no conclusions can be drawn from these measurements with respect to concentration.

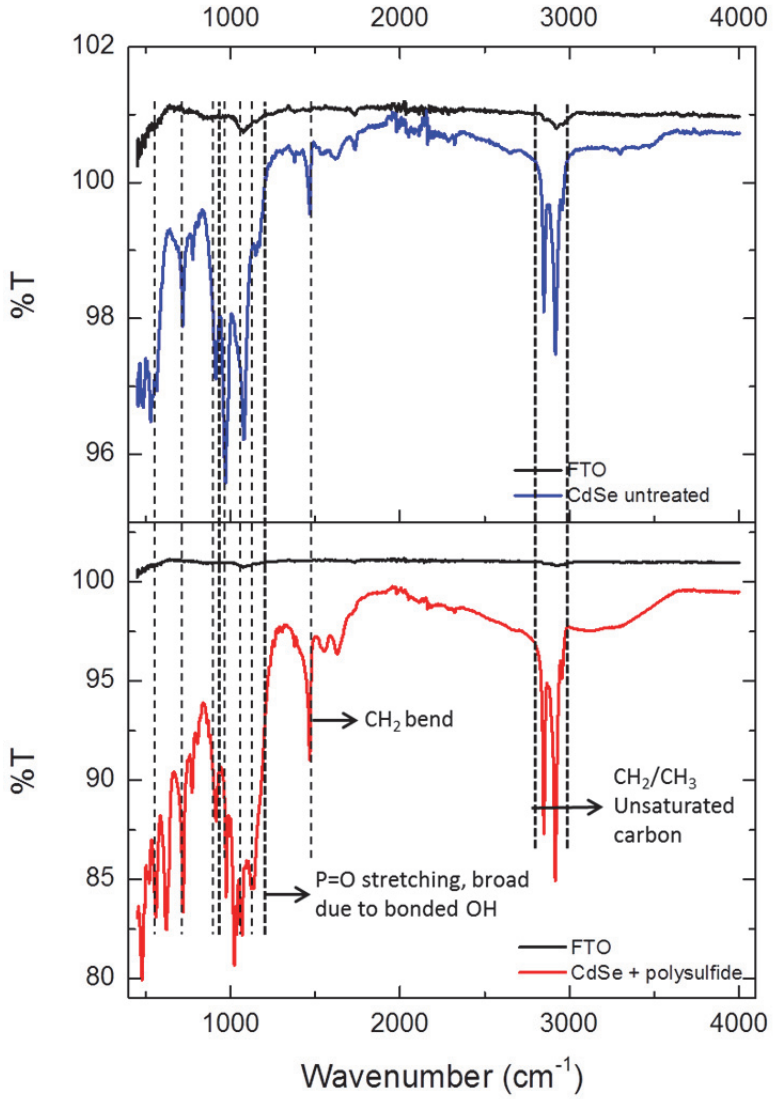

Figure 4.7. FT-IR spectra of an untreated (blue) and polysulfide treated (red) CdSe film. An FTO reference spectrum is also shown (black). Some of the distinct peaks/regions known to be present in the QD capping layer are labelled.

4.3.2 Morphology

SEM imaging was conducted to determine any changes in morphology post polysulfide treatment for the QD films. Surface images are grouped by three different levels of magnification for comparison of the overall (macro-) and finer film morphology. Typical SEM images of the film surfaces and cross-section profile (Figure 4.11) for both treated and untreated films are shown in Figure 4.8 – Figure 4.10.

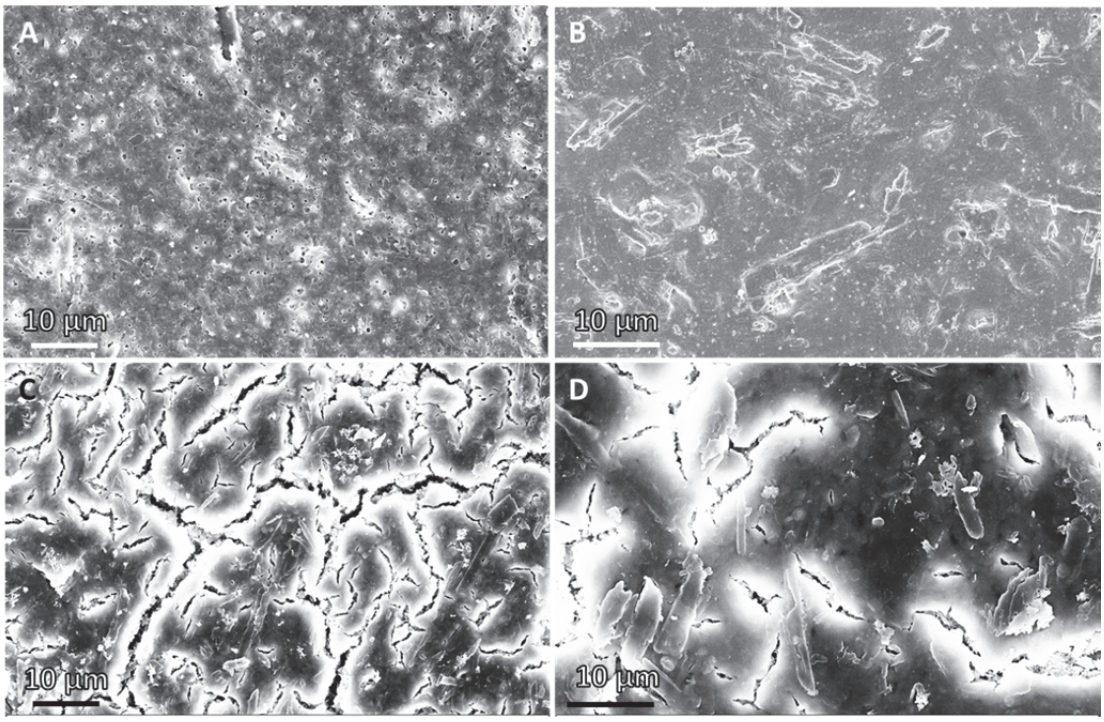

Figure 4.8. Low magnification SEM images of untreated (A (2 K magnification) and B (5 K magnification)) and polysulfide treated (C (2 K magnification) and D (5 K magnification)) CdSe films.

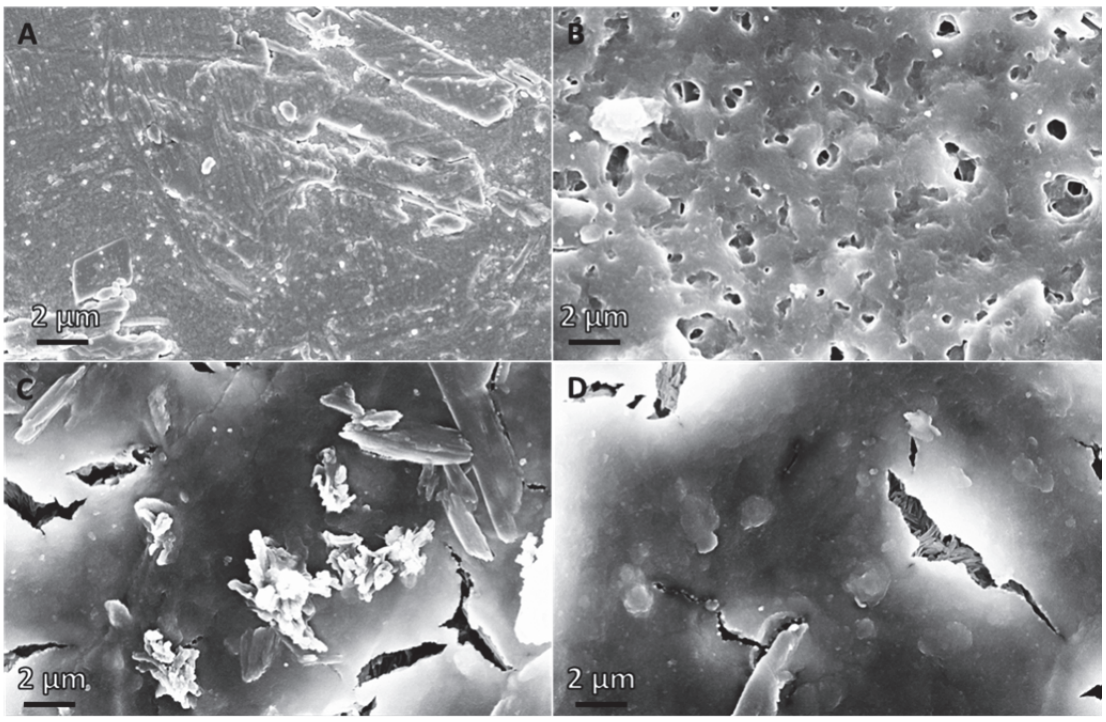

Figure 4.9. Higher magnification (15 K magnification) SEM images of untreated (A and B) and polysulfide treated (C and D) CdSe films.

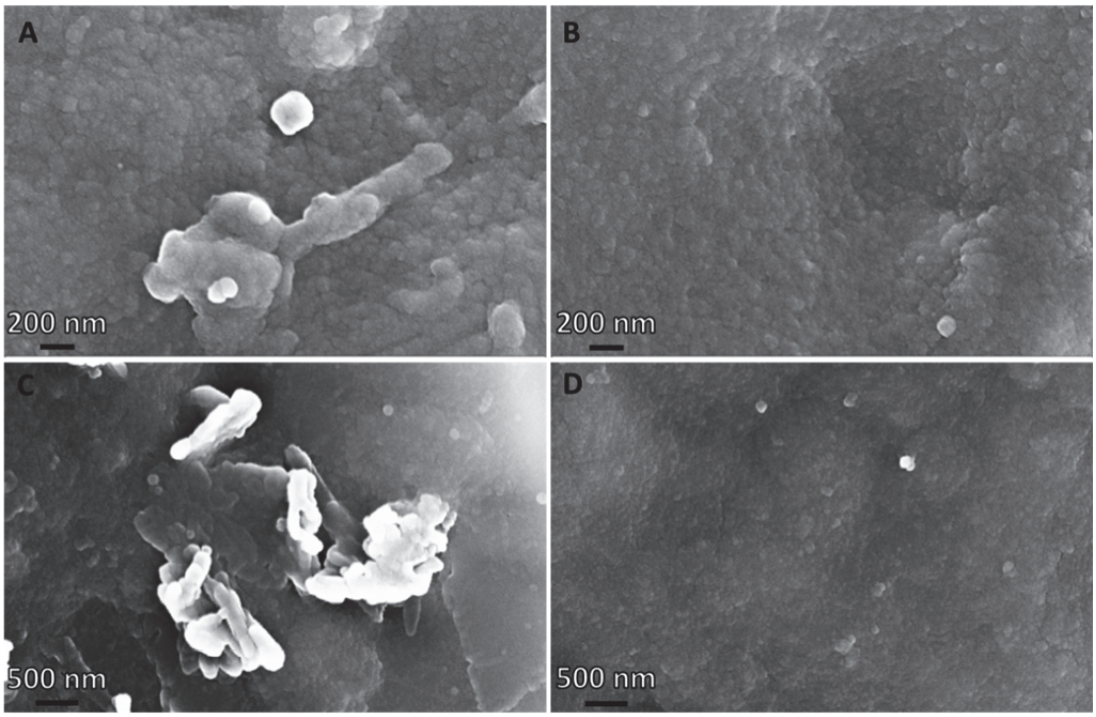

Figure 4.10. High magnification SEM images of untreated (A and B (100 K magnification)) and polysulfide treated (C and D (50 K magnification)) CdSe films.

The low/medium magnification imaging of the film surfaces reveal a vast increase in surface cracking of the films post polysulfide treatment (Figure 4.8 and Figure 4.9). The induced cracks are up to 70 μm in length and up to 800 nm in width. The untreated film is relatively more continuous (Figure 4.8 (b)), however, in some regions randomly distributed, non-regularly shaped pores (~ 0.2 – 1.5 μm in diameter) (Figure 4.9 (b)) are observed. Samples were also imaged by cross-sectional profiles revealing the depth of the cracking (Figure 4.11). Cracking has previously been observed for ethanethiol treated PbS CQD films.[28] This was attributed to induced stress in the films upon excess thiol treatment and hence the formation of cracks. In that study, aluminium was used as a top contact for the QD film and thus the devices failed due to short circuiting. In the work presented here, electrolyte solution was utilized rather than a metallic top contact and hence no short circuiting was observed.

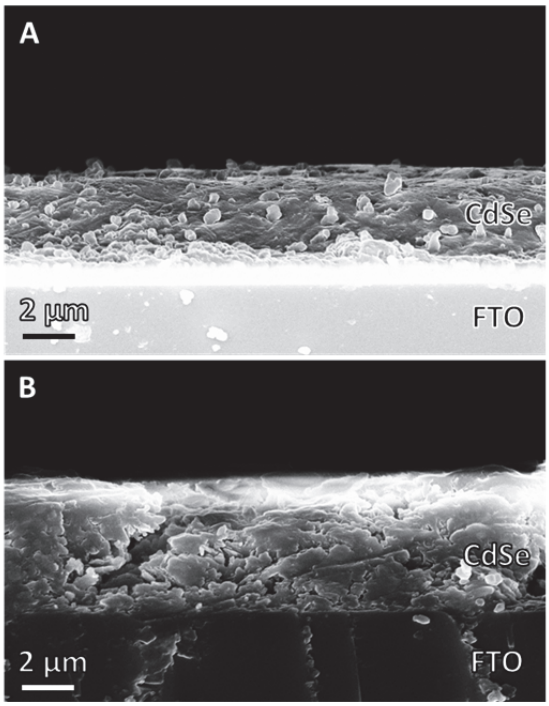

Figure 4.11. Typical low magnification (15 K) cross-sectional SEM images of untreated (A and B) and polysulfide treated (C and D) CdSe films.

Regions of charging (white areas) are observed along the crack boundaries are also observed in the polysulfide treated film SEM micrographs. Both the untreated and treated samples were prepared and coated (with chromium) for SEM imaging under the same conditions and hence it can be assumed this is due to a difference in conductivity (non-conducting areas) of the films. We therefore propose that the presence of the non-conductive areas alongside cracks in the films reflects a loss in contact between the top of the CdSe film and the conductive FTO glass (partial film delamination).

Film thicknesses of 3.6 ± 0.5 µm and 4.4 ± 0.5 µm were estimated from the images for the untreated and polysulfide treated films respectively. Given the crude technique used to prepare the samples (hence non perpendicular cross-sections) the film thickness is quoted as a rough estimate. In agreement with film delamination, cracks and areas of delamination were observed in the cross-sectional images of the films treated in polysulfide.

At 15 K magnification, surface bound crystals were observed in the polysulfide treated samples (e.g. only Figure 4.9 (c)). This could infer surface deposition of material; probably either sulfur or sodium sulfide crystals.

At higher magnification (Figure 4.10) the films were imaged in the dark non-charging regions between cracks and surface features. In these regions the surfaces of both films are populated with a textured surface of approximately spherical features of ~ 60 nm diameter and less.

STEM imaging of a QD sensitized TiO_2 pressed film was conducted (Figure 4.12). The micrographs show a relatively monodisperse distribution of the QDs at the TiO_2 surface.

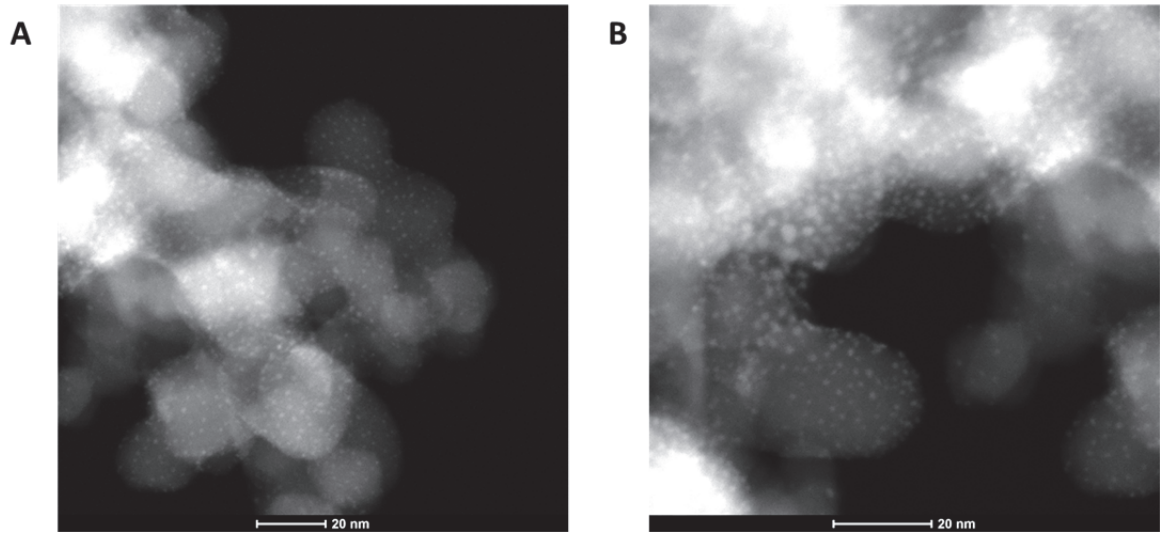

Figure 4.12. STEM micrographs of QD sensitized TiO_2 imaged with the TITAN TEM at magnifications (A) 450 K and (B) 640 K.

4.3.3 Optical Analysis

UV-Vis absorbance and photoluminescence (steady state and time resolved) spectroscopies were conducted to monitor the optical properties of the QD photoanodes before and after the polysulfide treatment.

The UV-Vis absorbance spectra of the untreated and polysulfide treated QD films measured in a linear spectrometer (see Chapter 2) are shown in Figure 4.13 (a). The normalized spectra of these same data are shown in Figure 4.13 (b) with the normalized QD soln spectrum for comparison. Post polysulfide treatment several observations are of note; approximate preservation of peak shape, a red shift in the first excitonic peak position and enhanced absorbance across the entire spectra.

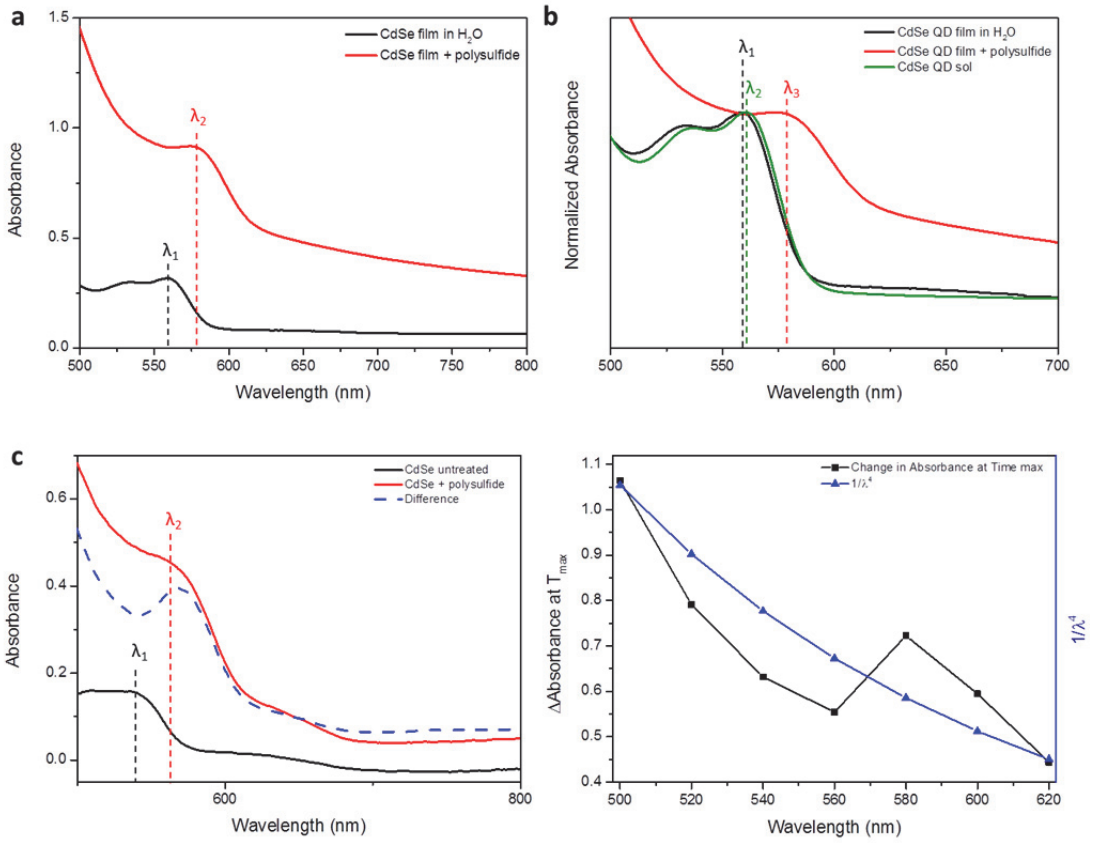

Figure 4.13. (a) Absorbance and (b) normalized absorbance spectra (linear measurement) of an untreated CdSe QD film (on FTO) before (black) and after (red) polysulfide treatment. Both were measured in water/polysulfide solution. (c) Total absorbance of the same, dry films (measured with an integrating sphere). (d) The wavelength dependent change in absorbance plotted with the inverse of wavelength to the power of four.

Relative to the QD soln, the general shape of the untreated QD film absorbance spectra confirms the preservation of a "QD type" structure and optical activity within the prepared films.

Post polysulfide treatment the first excitonic peak position red shifts from 560 nm to 576 nm. A shift in the first excitonic peak position (Figure 4.13) infers a redistribution of electronic distribution within the QD. Excitonic delocalization has been observed for both inorganic core/shell QD structures and, more recently for aromatic (relative to non-conjugated) organic capping ligands.[37,38] In the untreated films the QDs are surrounded by an organic capping layer, a system where the radial probabilities of finding an electron or hole are expected to be very low outside the CdSe QD boundary. The redshift measured post polysulfide treatment corresponds to an increase in the

electron distribution; likely due to an expansion of the physical size of the QD or an alteration in the material surrounding the QD such that excitonic tunnelling/leakage at the QD boundary is extended into an extended matrix and hence a shift to lower energies. Alongside the red shift, the absorbance peak broadens, which could infer Oswald ripening of the QDsas CdSe is dissolved and re-deposited as $CdSe_{1-x}S_x$.

Vegard's Law dictates that the band gap of a semiconductor alloy is approximately linearly proportionate with respect to the concentration of constituents. "Band bowing" is the phenomenon whereby the band gap of alloyed materials exhibits non-linearity dependence with respect to alloy composition (contrary to Vegard's Law). In a recent publication by Cherns et al,[43] extremely strong band bowing was reported for $CdSe_{1-x}Te_x$QDs such that for alloys where $x < 0.5$ a red shift in absorbance is observed. For QD alloys with a composition of $x > 0.5$ the effect is reversed and indeed a blue shift (in agreement with Vergard's Law) is observed. To date, no such effect has been reported for $CdSe_{1-x}S_x$. Indeed the data presented in this thesis does not verify such an effect for $CdSe_{1-x}S_x$, however, it is a possible explanation for the red shift observed post polysulfide treatment. Further investigation with a series of $CdSe_{1-x}S_x$ QDs whereby QD diameter is fixed, but x is varied would be required to verify this as an explanation for the red shift.

A further difference between the pre and post treated films is enhanced absorbance across the entire spectra which suggest an increase in scattering. Contrary to absorbance measurement where the difference between incident and transmitted light is monitored in a linear geometry (with respect to light source, sample and detector), the absolute absorbance is determined from a combination of diffuse and specular transmittance and reflectance data, thus eliminating scattering from the measurement (for further detail see Chapter 2). The difference between the two measurements indicates that polysulfide treated QD films scatters light much more readily than the untreated films. Rayleigh scattering dictates that light scattering is proportional to the inverse of wavelength to the power of four. The change in absorbance (the difference between untreated and polysulfide treated films) was plotted with respect to wavelength, λ (Figure 4.16 (d)). On the same figure, $1/\lambda^4$ is also plotted. The discrepancy between the two spectra verifies that the change in absorbance cannot entirely be attributed to scattering; rather, the shift in λ of the first excitonic peak is real.

Photoluminescence spectroscopy was also used to monitor the influence of polysulfide electrolyte on the CdSe QD films (Figure 4.14). In agreement with the absorbance spectra (Figure 4.13), a red shift in the peak position is observed. Specifically, the peak shifts from 562 nm (untreated) to 592 nm (polysulfide treated) ($\Delta\lambda_{max}$ = 30 nm). In addition to the spectral shift, the photoluminescence peak width (FWHM) broadens from 33 nm to 43 nm. Peak broadening corresponds to Oswald ripening in the QD size distribution. This is discussed in further detail in the further discussion section of this chapter.

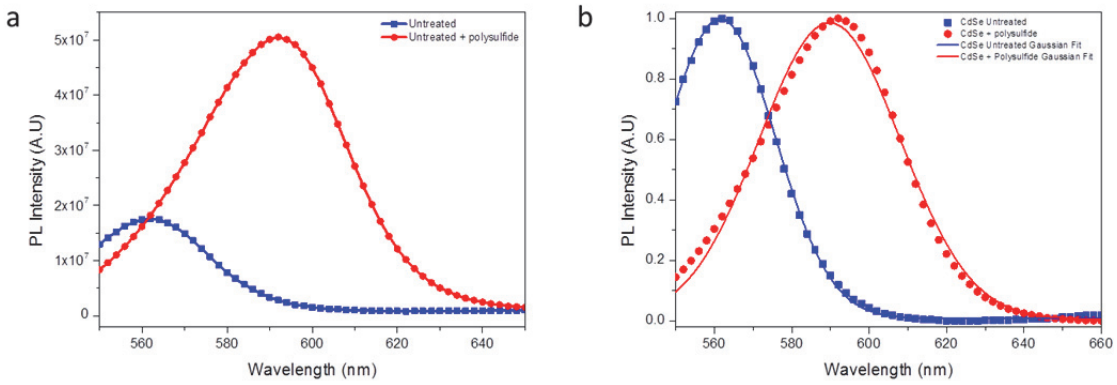

Figure 4.14. Photoluminescence response of CdSe QD film before (black) and after (red) polysulfide treatment. The films were excited at 500 nm. (a) is the raw photoluminescence spectra; (b) is the normalized data (data points) and corresponding Gaussian fits (line).

4.3.4 Temporal Evolution of Polysulfide

The evolution of the spectral shift due to polysulfide treatment was monitored with respect to time using UV-Vis absorbance spectroscopy (Figure 4.15). Figure 4.15 (d) tracks the wavelength of the first excitonic peak position (λ_{max}). It is evident that the optical evolution saturates/plateaus after ~800 s (13.3 min). Polysulfide treatment was therefore defined as the exposure of a sample to polysulfide solution for 30 mins to ensure each CdSe QD film is fully converted.

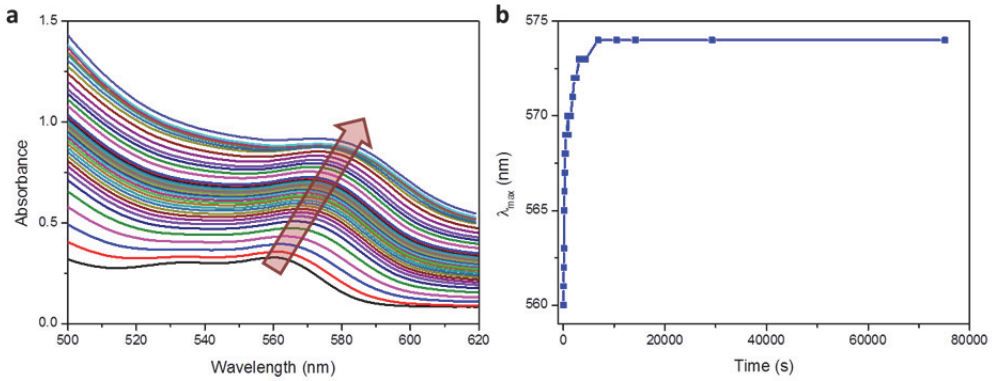

Figure 4.15. (a) Temporal evolution of the absorbance spectra (linear measurement). The first measurement (black) was conducted pre-polysulfide treatment. (b) λ_{max} (the first excitonic peak absorbance spectra) of the QD film plotted with respect to time. All measurements were conducted in water/sodium sulphite solution.

To track the influence of the polysulfide treatment at different wavelengths, wavelength optical absorbance was plotted with respect to time (Figure 4.16 (a)). The same data normalized is shown in Figure 4.16 (b) and enlarged for clarity in Figure 4.16 (c). The spectral evolution with respect to absorbance at each wavelength appears to be approximately consistent implying chemical change responsible for the transition contributes at all wavelengths.

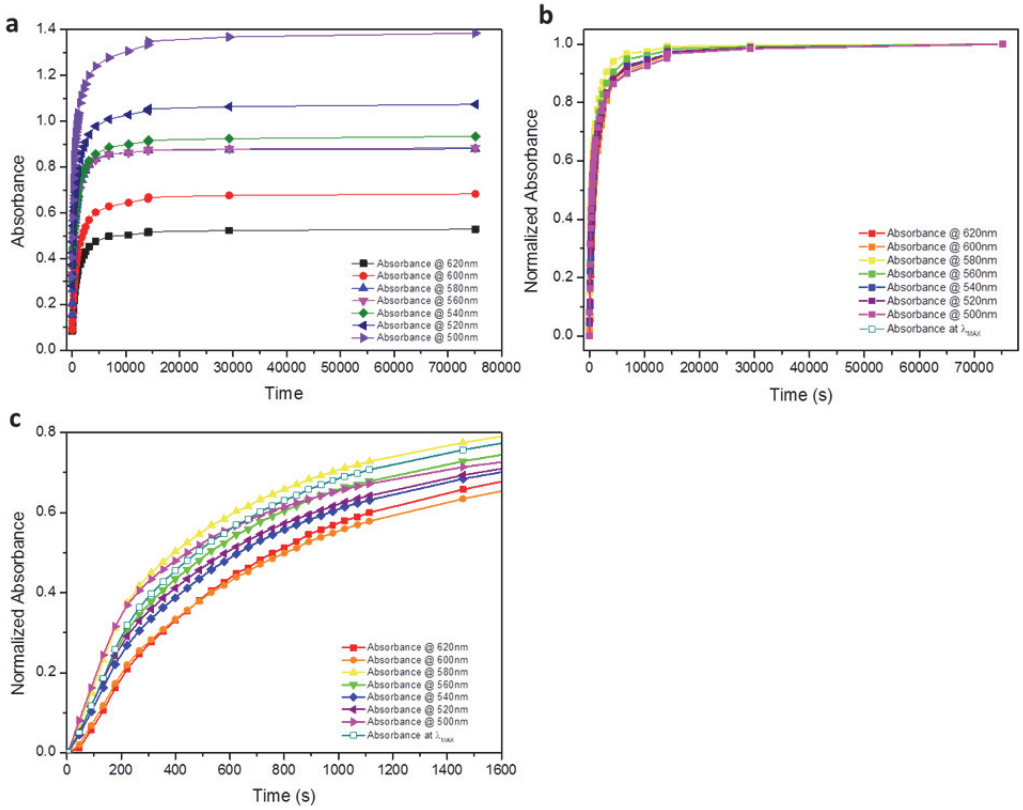

Figure 4.16. (a) Evolution of absorbance with respect to time at 620 nm, 600 nm, 580 nm, 560 nm, 540 nm and 520 nm (b) normalized with absorbance at first excitonic peak position, (c) normalized with absorbance at first excitonic peak position, the first 1600s is only shown.

4.3.5 Time Resolved Fluorescence Spectroscopy

Time resolved fluorescence was used to monitor the photoluminescence decay rate of the QD soln and untreated/treated QD films. The decay spectra for each sample (excited at 560 nm) are shown in Figure 4.17. The average lifetime photoluminescence decay rates are shown in Table 4.4.

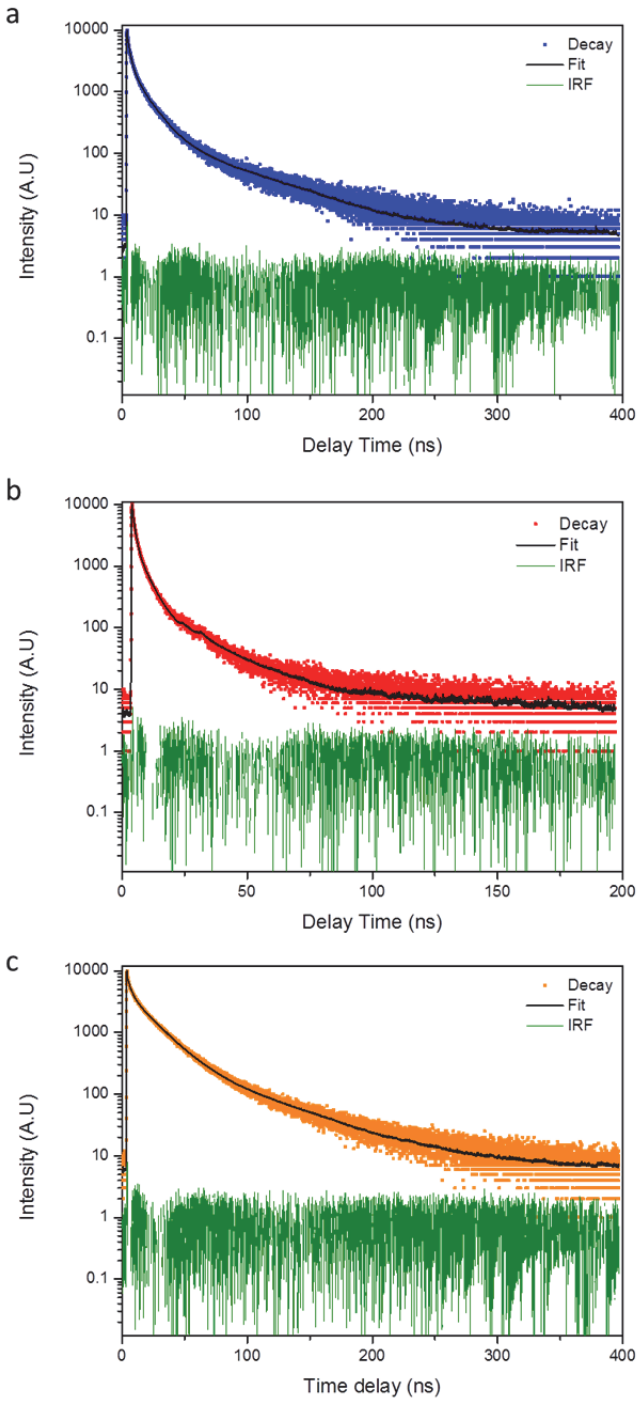

Figure 4.17. Photoluminescence delay rate, fit and instrument response function (IRF) trace of (a) untreated CdSe film, (b) polysulfide treated CdSe film and (c) CdSe QD soln used to prepare the films. The data was recorded with 560 nm excitation.

Sample	τ_{AVG}(ns)
Untreated CdSe film	18.6
Polysulfide treated CdSe film	6.6
CdSe QD soln	26.8

Table 4.4. Average decay rate for the photoluminescence decay spectra shown in Figure 4.17.

Electron-transfer (injection) rate constants for this system can be calculated following the mathematical analysis used elsewhere for QD injection into a TiO_2 substrate.[39,40] The calculation assumes that all photoexcited electrons in the QD films decay by either electron injection into the conductive glass (FTO) or radiative relaxation (emission of a photon);(4. 8), where τ_{QD+FTO} and $\tau_{QD}$are the measured average photoluminescence decay time constants for QD-FTO film and QD soln respectively. Calculated electron transfer rates (k_{et}) are tabulated in Table 4.5 where k_{et} is calculated by Eq 4.8. The rate of electron transfer is enhanced by 7 post polysulfide treatment.

$$k_{et} = \frac{1}{\tau_{QD+FTO}} - \frac{1}{\tau_{QD}} \qquad (4.8)$$

Sample	k_{et}(s^{-1})
Untreated CdSe film	0.017
Polysulfide treated CdSe film	0.114

Table 4.5. Calculated injection rate constants for the untreated and polysulfide treated CdSe films on FTO.

Although literature procedures have been followed to estimate these rate constants, a discrepancy in attributing time resolved fluorescence decays to charge injection has been raised.[41] For example, in a recent study the fluorescence decay times for a QD soln was found to be quenched upon QD sensitized on a ZrO_2 film.[42] Unlike TiO_2, electron injection from QD to ZrO_2 is not energetically permitted (conduction band edge of ZrO_2

is higher than the QD) and thus the quenching cannot be due to injection only. Hence it is demonstrated that fluorescence lifetime measurements cannot differentiate between electron injection into the TiO_2 substrate and recombination processes at the QD-TiO_2 interface. Here, the technique is used to determine the lifetimes of fluorescence in two QD only films, one treated with polysulfide. The quenching could, therefore, be due to a combination of both electron injection and non-radiative mechanisms induced upon polysulfide treatment.

4.3.6 Photoelectrochemistry

4.3.6.1 Cadmium Selenide Quantum Dot Only Photoelectrodes

The photocurrent response of untreated and polysulfide treated CdSe QD films are shown in Figure 4.18. The corresponding normalized UV-Vis absorbance spectra are shown for comparison. The untreated CdSe QD films show no photocurrent response. Conversely, photocurrent responses were recorded for the same CdSe film post polysulfide treatment. Hence the chemical/structural changes in the QD and/or film due to polysulfide treatment must switch on the photocurrent. The photocurrent onset (~640 nm) for polysulfide treated samples mimics that of the absorbance spectra. The photocurrent spectrum peaks at 570 nm, directly in between the absorbance maxima positions of the untreated (560 nm) and polysulfide treated (576 nm) films.

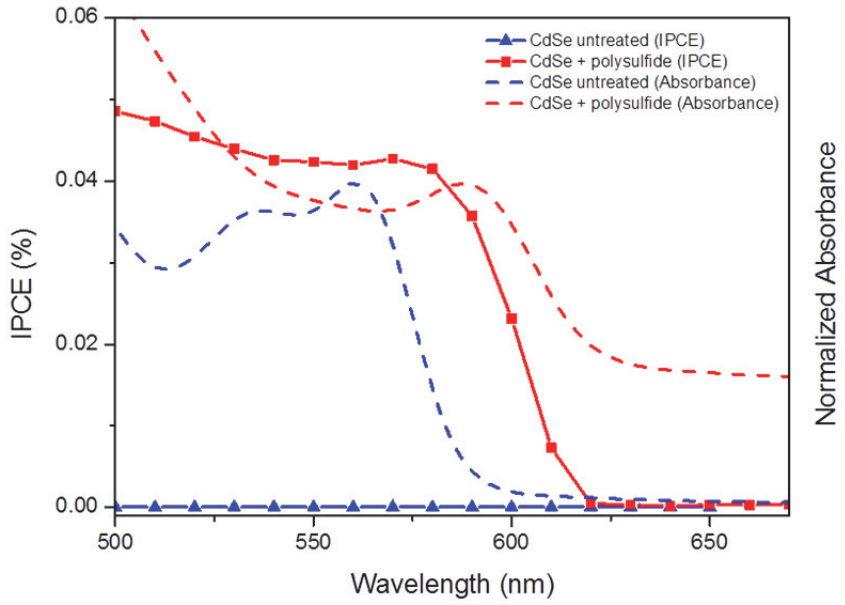

Figure 4.18. IPCE photocurrent (continuous lines) and normalized absorbance (dashed line) (at the first excitation peak) spectra measured in 0.5 M Na_2SO_3 (pH 7) pre (blue) and post (red) polysulfide treatment. The photocurrent was measured at 0 V against a silver/silver chloride reference electrode with a lock-in amplifier with a chopper frequency of 0.5Hz.

The absorbed photon conversion efficiency (APCE) was calculated for the photoanodes as shown below in Figure 4.19. In agreement with Figure 4.18, the films are only photoactive (produce photocurrent) post polysulfide treatment. With regards to the spectral shape, the onset of APCE is 620 nm in agreement with the absorbance onset. The spectral shape of the polysulfide treated photoanode verifies that the chemical and optical changes reported in this work indeed alters the photoactivity of the QD films. With regards to the magnitude of the APCE values, at the peak absorbance position of the QD treated film (~590 nm) is 0.8 %. This is the percentage of the absorbed light that is successfully converted to photocurrent and hence infers that there are significant loss mechanisms in the quantum dot film. The low efficiencies can be accredited to a combination of factors as discussed here. Firstly the films investigated here are significantly thicker than those prepared in the QD only photoanode literature, hence charge carrier transport across the films (electron and hole separation) is less favourable. Also, given the morphology of the films post treatment (cracked) it can be expected that significant portions of the films will lose contact with conductive glass

interface. Finally, for the successful injection of an electron into the FTO for QD only photoanode the electron/hole pair must be transported through the QD film. Given that QD size dictates the band gap size and conduction band edge any large QDs within the film will trap charge carriers and hence substantially suppress photocurrent efficiencies.

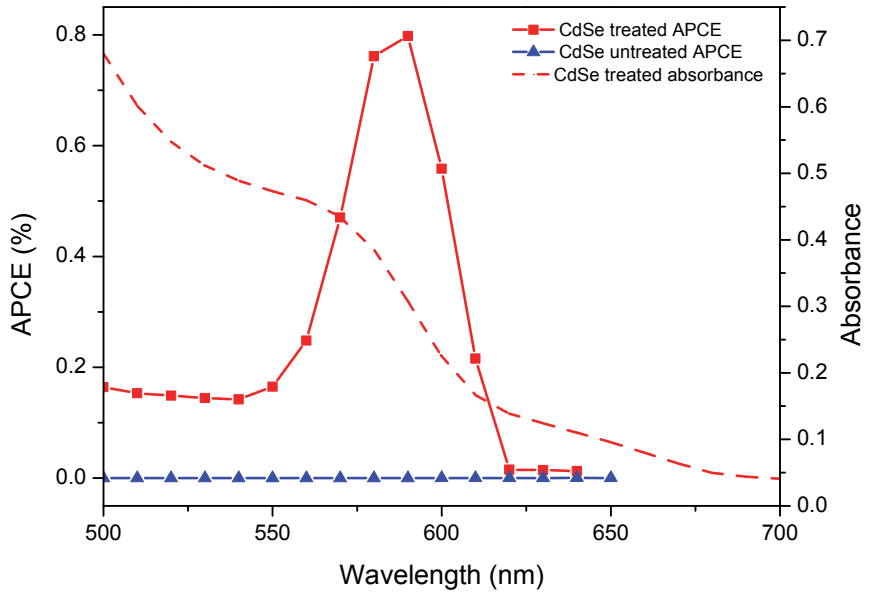

Figure 4.19. The absorbed photon conversion efficiency (APCE) for the untreated (blue) and polysulfide treated (red) cadmium selenide photoanodes. The spectra were calculated from the data presented in Figure 4.18 and Figure 4.13(c).

4.3.6.2 Titanium Dioxide Only Photoelectrodes

To determine the influence of polysulfide electrolyte on TiO_2 only films the photocurrent response of TiO_2 only film was measured pre (untreated) and post polysulfide treatment (Figure 4.20). It is apparent that the photocurrent response of the TiO_2 film is slightly decreased post polysulfide treatment at wavelengths <380 nm. However for the >400 nm region the photocurrent spectra remain approximately unchanged.

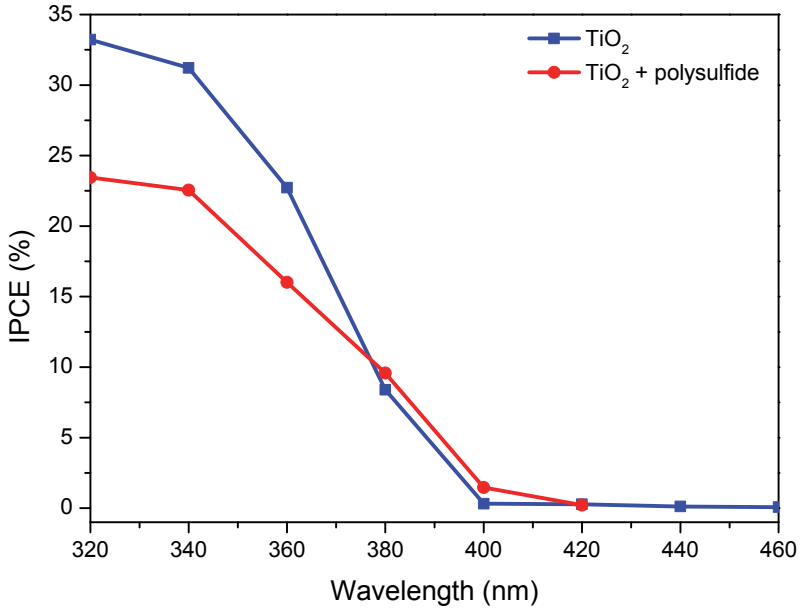

Figure 4.20. IPCE photocurrent spectra of TiO_2 only film measured in pH 7, 0.5 M Na_2SO_3 pre (blue) and post (red) polysulfide treatment at 0 V against a silver/silver chloride reference electrode. The spectra were recorded without the optical chopper/lock-in amplifier.

4.3.6.3 Cadmium Selenide Quantum Dot Sensitized Titanium Dioxide Photoelectrodes

The photocurrent response of untreated and polysulfide treated CdSe sensitized TiO_2 (Figure 4.21) shows an overall decrease in the photocurrent response of the films post treatment particularly at the lower wavelengths (400 nm – 540 nm). However, the photocurrent signal is slightly enhanced at wavelengths >540 nm. Prior to polysulfide treatment the photocurrent onset coincides with the onset of absorbance of the QD soln at approximately 600 nm. Post treatment the onset is red shifted to approximately 620 nm which coincides with that of the treated CdSe QD only films (Figure 4.18). Thus, in the spectral region 420 nm – 650 nm where there is no response from the TiO_2 (Figure 4.20) it can be assumed that the change in QD with respect to polysulfide treatment is analogous in both the QD only and QD-TiO_2 films. Further experimental work on the influence of the pressing on optical and photocurrent spectra are presented in the Appendix.

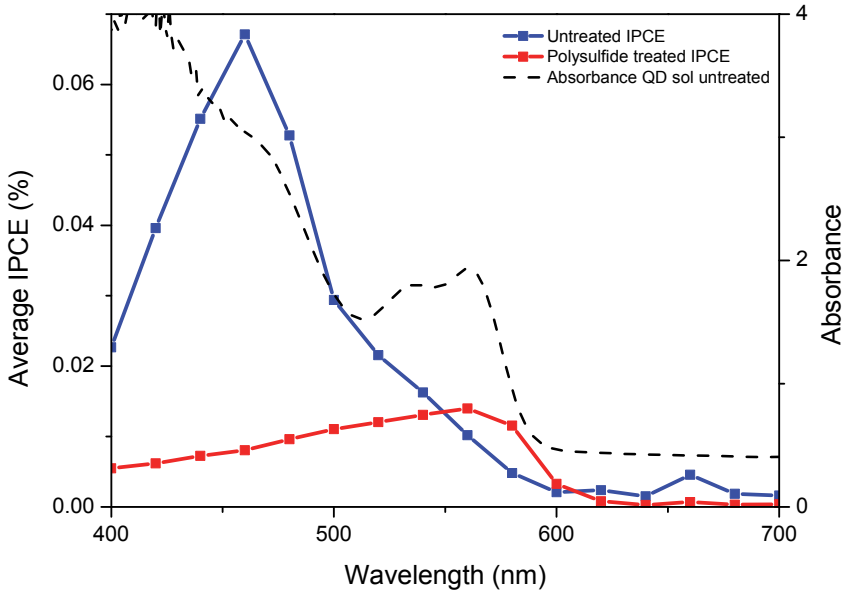

Figure 4.21. Photocurrent spectra of untreated (blue) and polysulfide treated (red) QD sensitized TiO_2photoanode. The absorbance of the (untreated) QD soln is plotted for comparison.

The relatively low efficiencies of the QD sensitized TiO_2 photoanodes are accredited the photoanode architecture. As depicted in Figure 4.1, QDs are sensitized at the surface of the TiO_2 particles prior to the preparation of the porous film. Thus the transfer of electrons through the TiO_2 film will be substantially quenched.

4.3.7 Further Discussions

Individually, the experimental results and discussions on the influence of polysulfide solution on the CdSe QD and QD sensitized TiO_2photoanodespresented in this chapter have enabled multiple chemical and structural changes to be proposed, and in some cases verified. In this section a collective overview of these discussions is given with particular emphasis on providing an explanation for the photocurrent results.

To address the explanation for switching on of photocurrent in CdSe QD films it is first necessary to discuss the possible reasons that the photocurrent may be absent in the untreated CdSe QD film. This can be explained by one or a combination of the following three factors;

1. **Exciton separation**

Upon absorbance of a photon of frequency v, $hv > E_g$ an electron is excited from the valence band to the conduction band of the semiconductor QD. However, for the device to produce photocurrent the electron and hole must separate and transport to opposite ends of the device. Failure to separate the excitonic pair will prevent photocurrent generation.

2. **Conductivity across the cell**

Post electron/hole separation both of the charge carriers must have an energetically favourable charge transport route such that the electron/hole can transport across the cell to opposite electrodes. If charge transport across the cell is blocked, the photocurrent will be zero.

3. **Trap states in the QD**

Trap states (generally associated with crystal surface defects) exist in QDs band structure and, as discussed in Chapter 1, competitively compete with photocurrent generation as loss mechanisms for exciton decay, thus reducing/quenching photocurrent production.

Structurally, cracks and voids were observed in the QD films post polysulfide treatment introducing film porosity and exposing thinner regions of the film to electrolyte. The introduction of porosity into the films significantly increases the surface area of the film exposed to electrolyte. Thus, similarly to sensitized solar cells an enhanced photocurrent response of the films could be expected. However, given that no photocurrent was observed in the planar films it is unlikely to be an explanation for the switching on of the photocurrent. With regards to film thickness, the films prepared for this work were shown ~4.0 ± 0.5 μm thick. In the literature much thinner QD only photoanodes of ~250 nm thickness are typically prepared.[28] Thus, perhaps charge transport across the untreated films is not possible; post polysulfide treatment, it is possible that thinner regions become exposed by the cracks and voids formed in the films and can therefore produce photocurrent. Explanation for low photocurrent efficiencies could be the extremely low surface area of thin film which is exposed to electrolyte. Given that the photocurrent onset matches the red-shifted UV-Vis

absorbance onset for treated films it is undisputable that the altered QD structure is optically active and able to photo inject. We therefore propose that this is not the only factor which contributes to switching on of photocurrent post polysulfide treatment.

The preservation of absorbance spectra with regards to spectral shape (post polysulfide treatment) confirms approximate conservation of the QD-type structure. Given the red shift in QD peak position and the broadening of the peak, however Ostwald type ripening of the QDs can be inferred. However, the chemical changes (as determined by elemental ratios of S, Se and S + Se to Cd) post polysulfide treatment, confirm both a relative decrease in Se content and the introduction of S into the films. Elsewhere, it has been proposed that analogous to the photoelectrochemical cells (PECs) this is due to the substitution of sulfur replacing selenium in the QD.[7] However, the results presented here contradict substation as the *only* change for the QD films in polysulfide solution. With regards to the optical studies, substitution reaction implies the replacement of CdSe with CdS. CdS has a smaller band gap relative to CdSe and thus, a blue shift in the first excitonic peak would be expected for Se/S substitution. It is also of note that the unit cell structure of CdS is smaller than that of CdSe and thus substitution would slightly decrease the QD volume and thus a blue shift in the first excitonic peak would be expected.

The red-shift for the first excitonic peak position indicates an increased electron distribution of the QD exciton which is likely due to the introduction/change (from the organic capping ligands) material at the QD surface. The introduction of elemental sulfur at the surface of CdSe (either deposition and/or substitution) was verified by chemical analysis for polysulfide treated films. Confirmation of the location of the introduced sulfur within the QDs, however, can only be speculated.

Passivation of QD trap states (recombination centres) has been reported by several groups post surface treatment. Thiols have been highlighted elsewhere as being particularly good at passivating recombination centres. As evidenced by FT-IR, the organic capping layer remains present in the QD film post polysulfide treatment, however, sulfur substitution and deposition does occur. It is possible that the change in surface composition could contribute to the passivation of trap states. However, given the decrease in photocurrent efficiency of the QD-TiO_2photoanodes post polysulfide treatment, we do not postulate this.

Contrary to the QD only films, where a change in the macro structure of the QDs (cracking) could be attributed to the switching on of the photocurrent response, for the TiO_2 sensitized films photocurrent is observed both before and after polysulfide treatment. Specifically, there is a decrease in the photocurrent efficiency post treatment. In combination with the difference in morphologies of QD only films (agglomerates) and QD sensitized TiO_2 (QDs attached by a linker molecule to TiO_2) the difference in photocurrent response cannot in this instance be attributed to structural contributions analogous to the film structure. Prior to polysulfide treatment the photocurrent response matches the absorbance spectra of the QD with regards to photocurrent onset. In agreement with the CdSe QD sensitized TiO_2 literature,[7,22] post exposure to polysulfide, the photocurrent onset is red-shifted relative to the initial wavelength for the CdSe QD UV-Vis absorbance spectra. The onset is indeed red-shifted to the same wavelength onset (620 nm) as the photocurrent data for QD only films post polysulfide treatment. The shift must therefore correspond to the same structural/chemical change in the QD composition/capping layer responsible for the change in optical properties of the CdSe QD films.

4.4 Conclusions

In this work we have conducted an in depth analysis into the influence of polysulfide electrolyte on CdSe QD photoanodes. This search was motivated by the intriguing onset of photocurrent in QD only films post polysulfide exposure. Although multiple models and explanations are here proposed (and in some cases discarded) we verify sulfur substitution and deposition into QD films post exposure to polysulfide. We have proposed that for the QD only films a combination of changes in film morphology (introduction of cracks) and chemical identity of the QDs results in the switching on of photocurrent. With regards to QD sensitized TiO_2photoanodes we conclude that the polysulfide treatment induces a chemical change at the surface of the QD (introduction of sulfur) resulting in a shift in the optical band gap of the QD.

4.5 References

(1) Huang, S. Y.; Schlichthorl, G.; Nozik, A. J.; Gratzel, M.; Frank, A. J. *Journal of Physical Chemistry B* **1997**, *101*, 2576.

(2) Boschloo, G.; Hagfeldt, A. *Accounts Chem. Res.* **2009**, *42*, 1819.

(3) Hodes, G. *Journal of Physical Chemistry C* **2008**, *112*, 17778.

(4) Ning, Z.; Yuan, C.; Tian, H.; Fu, Y.; Li, L.; Sun, L.; Agren, H. *J. Mater. Chem.* **2012**, *22*.

(5) Lessner, P. M.; McLarnon, F. R.; Winnick, J.; Cairns, E. J. *J. Electrochem. Soc.* **1993**, *140*, 1847.

(6) Winnick, J.; Lessner, P. M.; McLarnon, F.; Cairns, E. J. *Appl. Phys. Lett.* **1988**, *53*, 1985.

(7) Chakrapani, V.; Baker, D.; Kamat, P. V. *Journal of the American Chemical Society* **2011**, *133*, 9607.

(8) Khan, S. A.; Hughes, R. W.; Reynolds, P. A. *Vibrational Spectroscopy* **2011**, *56*, 241.

(9) Jovanovski, V.; Gonzalez-Pedro, V.; Gimenez, S.; Azaceta, E.; Cabanero, G.; Grande, H.; Tena-Zaera, R.; Mora-Sero, I.; Bisquert, J. *Journal of the American Chemical Society* **2011**, *133*, 20156.

(10) Ellis, A. B.; Kaiser, S. W.; Wrighton, M. S. *Journal of the American Chemical Society* **1976**, *98*, 6855.

(11) Tenne, R.; Lando, D.; Mirovsky, Y.; Muller, N.; Manassen, J.; Cahen, D.; Hodes, G. *J. Electroanal. Chem.* **1983**, *143*, 103.

(12) Ellis, A. B.; Kaiser, S. W.; Wrighton, M. S. *Journal of the American Chemical Society* **1976**, *98*.

(13) Ellis, A. B.; Kaiser, S. W.; Bolts, J. M.; Wrighton, M. S. *Journal of the American Chemical Society* **1977**, *99*, 2839.

(14) Ellis, A. B.; Kaiser, S. W.; Wrighton, M. S. *Journal of the American Chemical Society* **1976**, *98*, 1635.

(15) Hodes, G.; Manassen, J.; Cahen, D. *Nature* **1976**, *261*, 403.

(16) Miller, B.; Heller, A. *Nature* **1976**, *262*.

(17) Manassen, J.; Hodes, G.; Cahen, D. *J. Electrochem. Soc.* **1977**, *124*, 532.

(18) Miller, B.; Heller, A.; Robbins, M.; Menezes, S.; Chang, K. C.; Thomson, J. *J. Electrochem. Soc.* **1977**, *124*, 1019.

(19) Hodes, G.; Manassen, J.; Cahen, D. *J. Electrochem. Soc.* **1981**, *128*, 2325.

(20) Cahen, D.; Hodes, G.; Manassen, J. *J. Electrochem. Soc.* **1978**, *125*.

(21) Noufi, R. N.; Kohl, P. A.; Rogers, J. W.; White, J. M.; Bard, A. J. *J. Electrochem. Soc.* **1979**, *126*.

(22) Bang, J. H.; Kamat, P. V. *Acs Nano* **2009**, *3*, 1467.

(23) Sargent, E. H. *Nature Photonics* **2012**, *6*, 133.

(24) Koleilat, G. I.; Levina, L.; Shukla, H.; Myrskog, S. H.; Hinds, S.; Pattantyus-Abraham, A. G.; Sargent, E. H. *Acs Nano* **2008**, *2*, 833.

(25) Maenosono, S.; Okubo, T.; Yamaguchi, Y. *J. Nanopart. Res.* **2003**, *5*, 5.

(26) Tang, J. A.; Sargent, E. H. *Adv. Mater.* **2011**, *23*, 12.

(27) Sargent, E. H. *Adv. Mater.* **2008**, *20*, 3958.

(28) Barkhouse, D. A. R.; Pattantyus-Abraham, A. G.; Levina, L.; Sargent, E. H. *Acs Nano* **2008**, *2*, 2356.

(29) Klem, E. J. D.; Shukla, H.; Hinds, S.; MacNeil, D. D.; Levina, L.; Sargent, E. H. *Appl. Phys. Lett.* **2008**, *92*, 3.

(30) Wuister, S. F.; Donega, C. D.; Meijerink, A. *Journal of Physical Chemistry B* **2004**, *108*, 17393.

(31) Klem, E. J. D.; MacNeil, D. D.; Cyr, P. W.; Levina, L.; Sargenta, E. H. *Appl. Phys. Lett.* **2007**, *90*, 3.

(32) Tang, J.; Kemp, K. W.; Hoogland, S.; Jeong, K. S.; Liu, H.; Levina, L.; Furukawa, M.; Wang, X. H.; Debnath, R.; Cha, D. K.; Chou, K. W.; Fischer, A.; Amassian, A.; Asbury, J. B.; Sargent, E. H. *Nat. Mater.* **2011**, *10*, 765.

(33) Yu, W. W.; Qu, L. H.; Guo, W. Z.; Peng, X. G. *Chemistry of Materials* **2003**, *15*, 2854.

(34) Wijayantha, K. G. U.; Peter, L. M.; Otley, L. C. *Solar Energy Materials and Solar Cells* **2004**, *83*, 363.

(35) Noufi, R. N.; Kohl, P. A.; Bard, A. J. *J. Electrochem. Soc.* **1978**, *125*, 375.

(36) Desilva, K. T. L.; Haneman, D. *J. Electrochem. Soc.* **1980**, *127*.

(37) Liang, Y. Q.; Thorne, J. E.; Parkinson, B. A. *Langmuir* **2012**, *28*, 11072.

(38) Dabbousi, B. O.; RodriguezViejo, J.; Mikulec, F. V.; Heine, J. R.; Mattoussi, H.; Ober, R.; Jensen, K. F.; Bawendi, M. G. *Journal of Physical Chemistry B* **1997**, *101*, 9463.

(39) Hyun, B. R.; Zhong, Y. W.; Bartnik, A. C.; Sun, L. F.; Abruna, H. D.; Wise, F. W.; Goodreau, J. D.; Matthews, J. R.; Leslie, T. M.; Borrelli, N. F. *Acs Nano* **2008**, *2*, 2206.

(40) Shepherd, D. P.; Sambur, J. B.; Liang, Y. Q.; Parkinson, B. A.; Van Orden, A. *Journal of Physical Chemistry C* **2012**, *116*, 21069.

(41) Pijpers, J. J. H.; Koole, R.; Evers, W. H.; Houtepen, A. J.; Boehme, S.; Donega, C. D.; Vanmaekelbergh, D.; Bonn, M. *Journal of Physical Chemistry C* **2010**, *114*, 18866.

(42) Leventis, H. C.; O'Mahony, F.; Akhtar, J.; Afzaal, M.; O'Brien, P.; Haque, S. A. *Journal of the American Chemical Society* **2010**, *132*, 2743.

(43) Hou, B. P., D. Kissling, G. P. Jones, J. A. Fermin, D. J. Cherns, D., *Journal of Physical Chemistry C* **2013**. DOI 10.1021/jp400208a.

Chapter 5. An Alternative Sensitizer, Molybdenum Disulfide

5. 1 An Introduction to Molybdenum Disulfide

Whilst the research field of quantum dot sensitized solar cells continues to expand there remain several limitations and concerns surrounding the use of cadmium selenide (CdSe) quantum dots (QDs) as the light harvesting material in solar cells. The limitations of QDSSCs are reviewed in Chapter 1 but those addressed by the replacement of the sensitized with MoS_2 include:

- The scalability of the reproducible synthesis of nanoparticles – including issues such as surface ligands, as highlighted in Chapter 1.[1-4]
- The traps within the band gap of the QDs (shallow, midgap and deep) leading to loss mechanisms for electron transfer. [5-8]
- Non-aqueous solution processed materials for solar cells – more appropriate would be aqueous for scalable manufacturing.
- Attachment of the QDs to the TiO_2 surface – reliance on linker molecule.[9,10]
- Toxicity of materials such as cadmium and selenium, plus the unknown hazards of working with nano sized materials.
- Low efficiencies of QDSSC – to date (December 2012) the maximum power efficiency of a liquid QDSSC is 5.32 %.[11]

The focus of this chapter concerns the photoactive material molybdenum disulfide (MoS_2). As reported in Chapter 1, bulk crystals of MoS_2 is known to have suitable bandgap energies and photostability for solar to energy conversion in photoelectrochemical cells (PECs).

Despite the promising photocatalytic and PEC properties of MoS_2, scalability remains a common challenge for TMD-based photoanodes. Growth of bulk single crystals is slow and the crystal sizes are typically limited to a few centimetres. Whilst thin film deposition via sputtering and evaporation offer potential routes to scaling up, crystal quality is often compromised [12-15]. Chemical synthesis of TMD nanoparticles is to

date, however, limited by poor control of particle structure and scalability. In contrast, atomically thin sheets of TMDs offer solution based routes toward scalable synthesis.[16-18] Chemical exfoliation of bulk TMDs is an efficient route for producing monolayer TMDs in aqueous colloidal suspensions[19]. The exfoliated sheets can be readily deposited uniformly over large areas [17] or hybridized with other materials,[20] enabling simple and scalable schemes for PEC device implementation.

While chemical exfoliation of MoS_2 has been known since the 1960s,[19] deposition of exfoliated sheets in uniform monolayered thin films form was only achieved recently.[17] Here, we utilize chemically exfoliated MoS_2 thin films and composites with TiO_2 nanoparticles are here investigated as PECs. We show that MoS_2 monolayer films exhibit effective PEC properties similar to bulk materials, generating photocurrent at excitation wavelengths above the direct band gap edge at ~ 660 nm (~1.9 eV). We find that in MoS_2 sensitized TiO_2 photoanodes, photoexcited electrons generated in MoS_2 are able to be injected into TiO_2 while holes are removed by the electrolyte so as to generate electrical current from incident light. Our results highlight the potential of solution-processed MoS_2 monolayers for PEC applications.

The work presented here was conducted in collaboration with Prof. Goki Eda (currently in the Departments of Chemistry and Physics, National University of Singapore, Singapore). G.E prepared all of the MoS_2 colloidal solutions and MoS_2 thin films. Hence only brief details of the experimental methodology and colloidal/thin film characterisations are presented. Full details of these have been published by G.E elsewhere, reference [17]. The MoS_2-TiO_2 synthesis, photoelectrochemical measurements, microscopy and optical analyses presented here were conducted by L. A. King.

5.2 Experimental

5.2.1 Preparation of MoS_2 Thin Films

In brief, MoS_2 nanosheets and films were prepared by forced hydration exfoliation of Li_xMoS_2 following the method described in reference [17]. The films were prepared on fluorine doped tin oxide (FTO) conductive glass with thicknesses spanning 1.7 – 18.9 nm. The films were annealed in a nitrogen atmosphere at 300 ˚C for 1 hour in order to stabilize the desired 2H phase (See Ref [17] for details). Film thickness was estimated from the UV-Vis absorbance spectra in reference to the empirical data of reference[17].

5.2.2 Preparation of MoS_2-TiO_2 Films

MoS_2-TiO_2 composite films were prepared by dispersing Degussa P25 TiO_2 into the aqueous solutions of 0.1 mg/ml MoS_2 nanosheets. The solutions were sonicated for 40 min, stirred and then separated by centrifugation. The transparent supernatant was removed and the remaining off-white pellet was re-dispersed in ethanol as a paste. UV-Vis analysis of the transparent supernatant confirmed the transfer of MoS_2 to the solid paste. The resultant paste was left to stir for >12 hours. Films were prepared by the doctor blade technique.

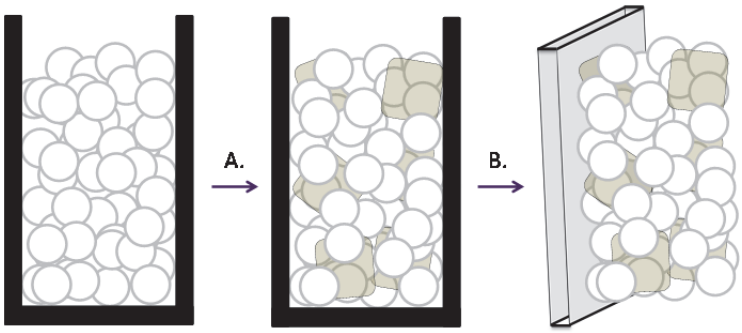

Figure 5.1. Schematic representing the route to MoS_2-TiO_2 electrodes. A. Addition of colloidal MoS_2 to TiO_2 nanoparticles. B. Doctor blade the composite paste onto FTO conductive glass to anneal at 300˚C in an argon atmosphere.

Three batches of films were prepared. Each batch contained a different ratio of MoS_2-TiO_2. Batch A contained TiO_2 only, B and C both contained 0.4 mg MoS_2, however B contained double the quantity of TiO_2 (0.5 g) relative to C (0.25 g). Each paste was prepared with a quantity of ethanol proportionate to the quantity of TiO_2. Each film was prepared using the same volume of paste (20 µL) on FTO conductive glass using the doctor blade technique. The films were annealed for 30 min under a flow of argon at 300˚C. The thickness of prepared films (determined by SEM) was approximately 10 µm.

5.3 Results and Discussion

5.3.1 Optical Analysis

The absorption spectra of the MoS_2 thin films (Figure 5.2 (a)) exhibit the characteristic optical peaks of bulk MoS_2. The optical transitions associated with these

peaks in the visible region (400-800 nm) correspond to the photoexcitation of d- orbital electrons (Figure 5.2 (b)) which do not contribute to the chemical bonding of MoS_2.[21] The energy band structure of MoS_2 and the optical transitions associated with the absorption peaks are illustrated in Figure 5.2.b.[22,23] The A/B peaks correspond to the band edge excitons at the K and K' points of the Brillouin zone[24] while the C/D transitions are interband transitions from the occupied dz^2 orbital to unoccupied dxy, x^2-y^2 and dxz, yz orbitals. The measured A/B excitonic peaks (Figure 5.2 (a)) show a slight blue shift by approximately 14 nm as film thickness decreases from 18.9 nm to 1.7 nm (prominent in normalized spectra, Figure 5.3) due to confinement effects.[17] The excitonic peak A wavelength for the 1.7 nm thickness film was 655 nm, consistent with the previously reported peak position for mechanically exfoliated MoS_2 monolayers,[25] confirming that the majority of the re-assembled film is a monolayer.

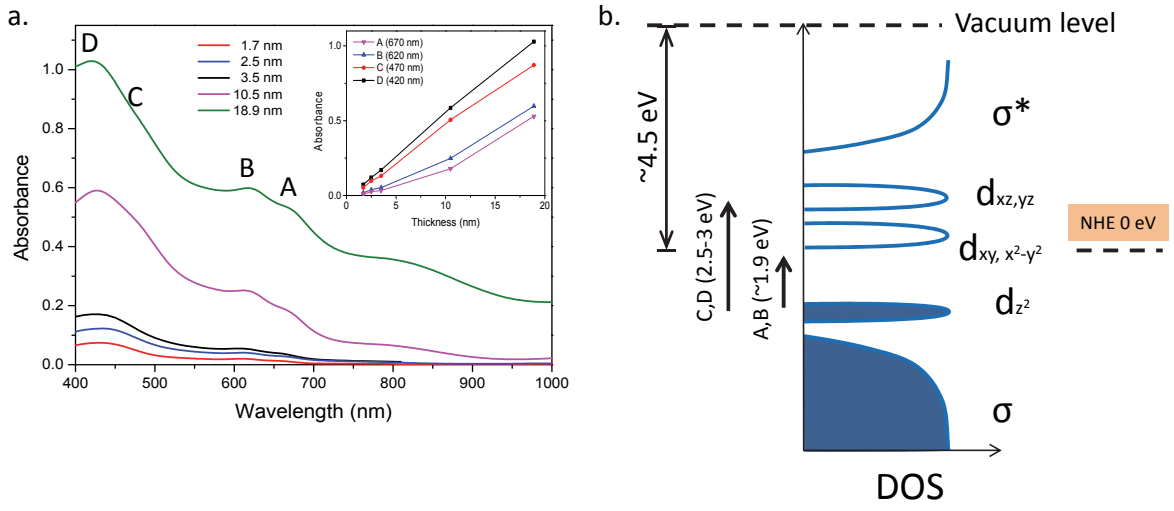

Figure 5.2. (a) UV-Vis absorbance of the MoS_2 thin films of different thicknesses (see legend) deposited on FTO conductive glass and annealed in a nitrogen environment at 300°C. The average film thicknesses were calculated from the empirical data of reference.[17] The inset shows the absorbance dependence on MoS_2 thickness for each of the four excitonic peaks A, B, C and D. (b) An approximate interband structure for MoS_2 adapted from reference 21. The transitions labelled A, B, C and D correspond to the transitions labelled in (a).

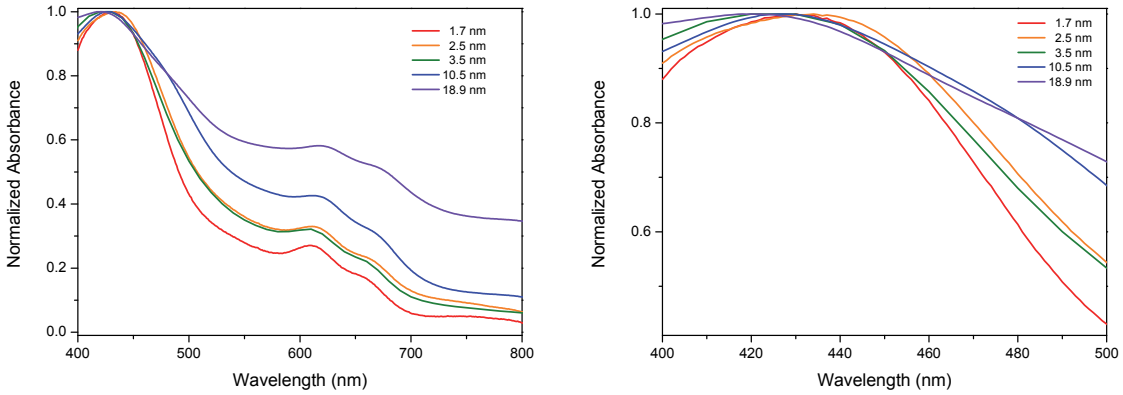

Figure 5.3 Normalized absorbance spectra (a) entire spectra, (b) 400 – 500 nm only, highlighting the red shift in absorbance peak for the thinnest films.

5.3.2 Photocurrent Studies

Photocurrent measurements were conducted on the thin MoS_2 films with thicknesses ranging from 1.7 to 18.9 nm. In order to compare samples with different thicknesses, we employed absorbed photon-to-current efficiencies (APCE) instead of IPCE to characterize the photocurrent efficiencies of our samples. APCE spectra for the films prepared with different film thickness are presented in Figure 5.4.

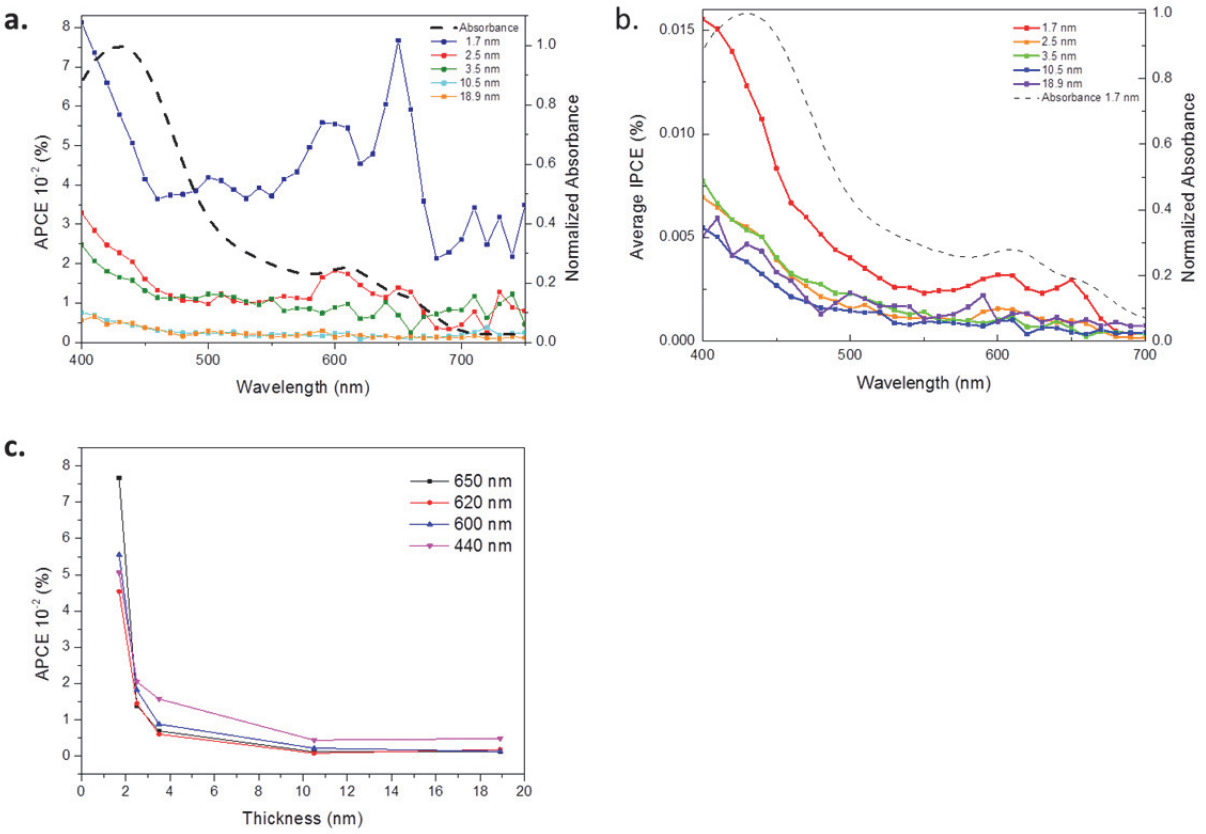

Figure 5.4. (a) Averaged (3 data for each film thickness) APCE spectra of the MoS_2 films of different film thickness (solid lines) conducted at 0 V potential against Ag/AgCl/1 M KCl reference electrode. The spectra are overlaid with the normalized UV-Vis absorbance of a thin (1.7nm) MoS_2 film (dashed black line). It is of note that relatively large APCE signals recorded for $\lambda > 680$ nm is due to accentuated noise (the monolayer has extremely low absorbance across this region, the IPCE data is shown in b). (c) Wavelength specific APCE values plotted with respect to film thickness.

The general features of the APCE spectra (Figure 5.4) of exfoliated MoS_2 thin films mimic the shape of their UV-Vis spectra. That is, all four excitonic peaks A, B, C and D absorb and photoinject electrons into FTO. With regards to photoanode stability, it is of note that samples stored dry, in the dark between measurements were stable with respect to photocurrent efficiency over the 12 month period that data were collected.

For most of the films prepared, the photocurrent spectra show distinct features near 590-670 nm corresponding to the A/B optical transitions, however, they lack clear features corresponding to C/D absorption peaks at 400 – 480 nm. It is of note that despite the higher absorption cross section of C/D peaks relative to A/B peaks, (Figure 5.2) lower photocurrent for the C/D excitations were observed. Similar behaviour has

been previously reported for bulk single crystals of $MoSe_2$ and WSe_2.[12] This may be related to different relaxation kinetics for the A/B excitons and the C/D electron-hole pairs.

An increase in film thickness from 1.7 nm to 10 nm was found to increase the absorbance of the MoS_2 films by 400 % (inset Figure 5.2 (a)). The corresponding IPCEs conversely decreased to less than 20 % of the original value. With respect to film thickness, a non-linear decrease in the APCE was observed (Figure 5.4 (b)), that is, once the film thickness reaches ~2.2 nm the photocurrent response plummets. By 10 nm thickness, the photocurrent signal is reduced below the level of experimental noise. We propose that the decrease in efficiency is due to a combination of factors. Firstly, as a consequence of the layered structure of MoS_2 out-of-plane charge mobility is considerably lower than the in-plane mobility. For monolayer MoS_2 where the transport distance and therefore time, for electrons to reach the MoS_2/FTO interface is minimized, the photocurrent efficiency is therefore highest. On the other hand, for samples of thickness greater than monolayer, the transit time for electrons to reach MoS_2/FTO interface is significantly increased and the exciton recombination is more likely to take place before electrons and holes are separated relative to in the monolayer film. Since the MoS_2 sheets are randomly stacked, the inter-plane charge transport is limited compared to commensurately stacked single crystals. Therefore, as the thickness of absorbing material increases, kinetics tends to favour exciton recombination rather than separation due to hampered charge transport leading to a decrease in the APCE.

Another possible contributing factor to the rapid decrease in APCE with film thickness is the evolution of MoS_2 band structure upon the isolation of a monolayer film. In the bulk, MoS_2 is an indirect bandgap semiconductor. The defining indirect transition exists at energies lower than the direct band gap transition corresponding to A/B excitons and is thus a competing relaxation mechanism for an exciton relative to injection into FTO (contribution to photocurrent). As the film becomes thicker, A/B excitons have additional pathways for relaxation to lower energy levels/recombination and thus the probability of exciton separation and charge transfer to FTO electrode is reduced.

5.3.3 Photoelectrochemical Studies

In order to investigate the energetics of the materials interface, the potential dependence of photocurrent of MoS_2/FTO electrodes was measured (Figure 5.5 (a)). As the potential across the cell is stepped up (or down) the Fermi level of FTO shifts relative to the MoS_2 conduction band (Figure 5.5 (b)). If the appropriate potential range is applied to the cell, the FTO conduction band can be raised higher than the MoS_2 conduction band minima and hence electron injection into FTO is suppressed. We observed that photocurrent associated with A/B and C/D excitations is dependent on the potential applied across the cell (Figure 5.5 (a)). These results suggest that electrons excited to the conduction band can thermalize to form band edge A/B excitons from where they are also able to inject into the FTO. The photocurrent signal corresponding to A/B transitions were shown to disappear at potentials lower than -0.13 ± 0.05 V (v SHE electrode) and hence this is the approximate flat band potential for the conduction band of excitons A/B.

This assertion was further confirmed by the observation that when potentials lower than -0.15V (against SHE) were applied, the film degraded and further measurements were no longer possible. This was likely due to the injection of electrons from the FTO into the d_z^2 orbital (valance band) (Figure 5.2 (b)) and thus irreversible reduction of MoS_2.

The possible mechanistic routes for electron-hole separation or recombination associated with C/D transitions are shown in Figure 5.5 (b). k_1 and k_2 correspond to injection of an electron into the FTO conduction band and hence these routes contribute to photocurrent. Conversely, k_3 and k_4 in combination with photoluminescence (k_6) correspond to loss mechanisms. As the potential applied across the cell is shifted the position of the FTO band changes and thus injection from k_1 in addition to k_2 is switched on.

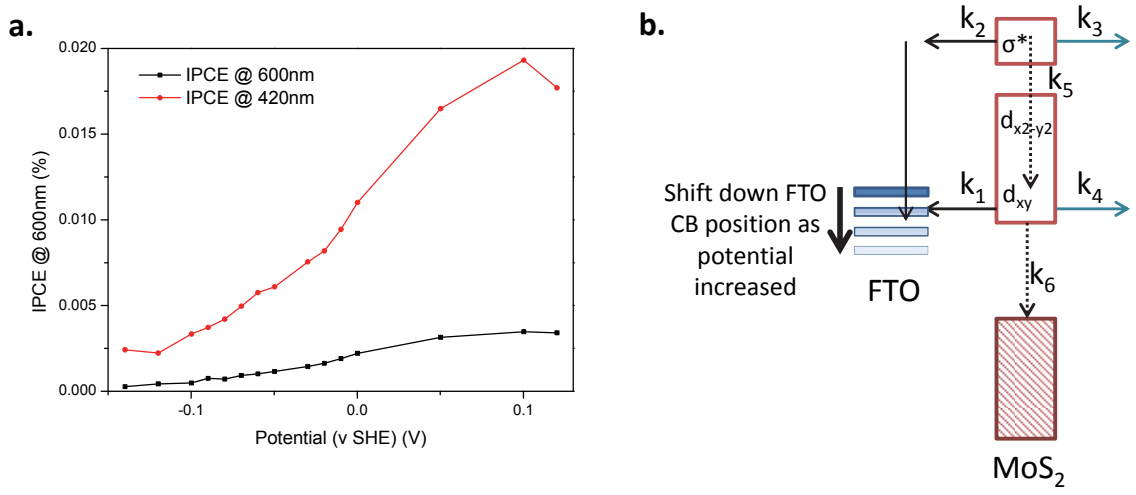

Figure 5.5. (a) The average IPCE photocurrent response plotted against potential (v SHE reference electrode) of a 4 nm MoS_2 film on FTO substrate. Between every second and third potential photocurrent measurement, the IPCE was re-measured at 0 V to confirm that the sample had not degraded from the photocatalytic efficiency. (b) The possible mechanistic routes for the decay of a C/D exciton. On the right hand side (red), k_1 and k_2 are the possible routes of injection of the electron into the FTO. On the left hand side (blue), k_3, k_4 and photoluminescence (k_6) are the competing recombination loss mechanisms. We propose that the upper conduction band can also decay to the lower conduction band via k_5.

The photocurrent spectra highlight that chemically exfoliated MoS_2 retains the bulk photoelectrochemical properties and demonstrates potential as a photoactive components in PEC solar cells. However, in order to achieve higher photon-to-current conversion efficiencies, alternative photoanode architectures need to be explored whereby the surface area of the MoS_2 monolayers is increased per unit area of illumination to overcome the small absorption cross section of monolayer MoS_2 and also encourage exciton separation. In the following sections, we discuss the PEC properties of photoeletrode consisting of MoS_2-TiO_2 hybrid. The structure of the electrode is analogous to the photoanode of the dye sensitized solar cell (DSSC)[26] where the exfoliated MoS_2 can be seen as a sensitizer to the mesoporous TiO_2. In such devices a photoexcited electron in the MoS_2 is expected to first inject into TiO_2 and subsequently diffuse through the TiO_2 film to the FTO substrate while the hole in MoS_2 is removed by electrolyte solution which penetrates into the mesoporous structure. The hole is transferred via electrolyte diffusion towards the counter electrode where electrons re-enter the cell, thus completing the circuit.

5.3.4 MoS_2 Sensitized TiO_2

5.3.4.1 Proof of Composition and Structure

Annealed composite films of MoS_2-TiO_2 were characterized by Raman spectroscopy by Dr. Zhao Weijie, National University of Singapore, Singapore to demonstrate the presence of MoS_2 in the as prepared photoanodes. Figure 5.6 (c) shows the spectra of the MoS_2-TiO_2 composite films overlaid with spectra of TiO_2 and MoS_2 only films. Enlarged around the 400 cm^{-1} peak (Figure 5.6 (b)) it is evident that the composite signal is the combination of both MoS_2 and TiO_2 peaks, indicating that the exfoliated MoS_2 remains intact during the preparation of the films.

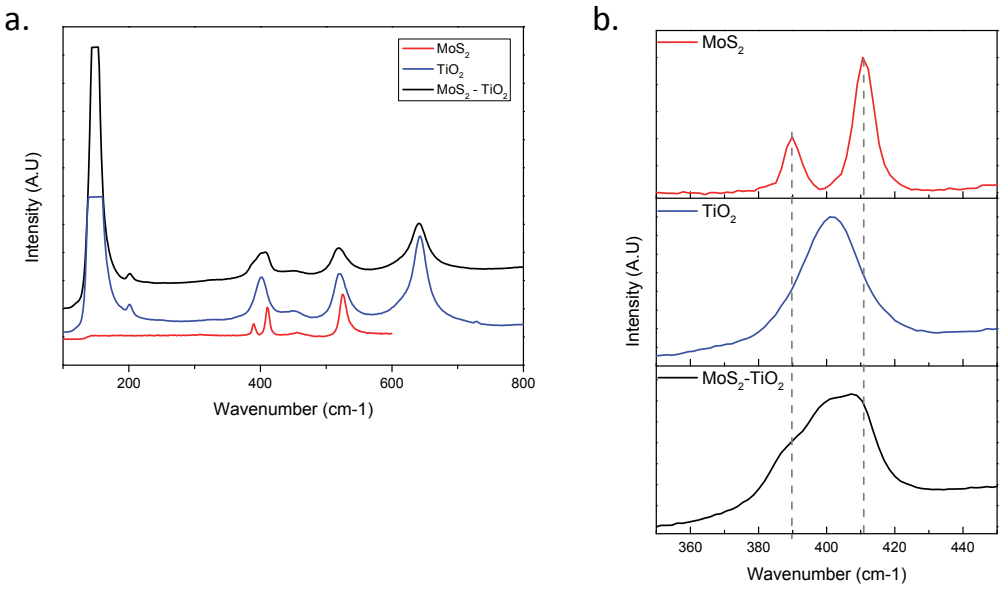

Figure 5.6. The Raman spectra of TiO_2, MoS_2 and MoS_2-TiO_2 composite films after annealing. (a) Full scale (b) The enlarged spectra at 400 cm^{-1} evidencing the presence of MoS_2.

The MoS_2-TiO_2 films were also characterised by both SEM and TEM imaging, Figure 5.7 (a). The SEM imaging confirms the mesoporous surface structure of the prepared photoanodes. Despite SEM imaging numerous (> 20) randomly selected regions on the photoanode surface identification of MoS_2 crystals was inconclusive. Conversely, the lattice spacing of TEM micrographs confirmed the presence of MoS_2 upon identification of the lattice fringes of individual TiO_2 particles and MoS_2 nanosheets (Figure 5.7 (b)). The lattice spacing of 0.3 nm correspond to the lattice plane spacing of anatase TiO_2

(101). The broader lattice spacing at 0.6 nm is assigned the hexagonal (002) plane of MoS_2.

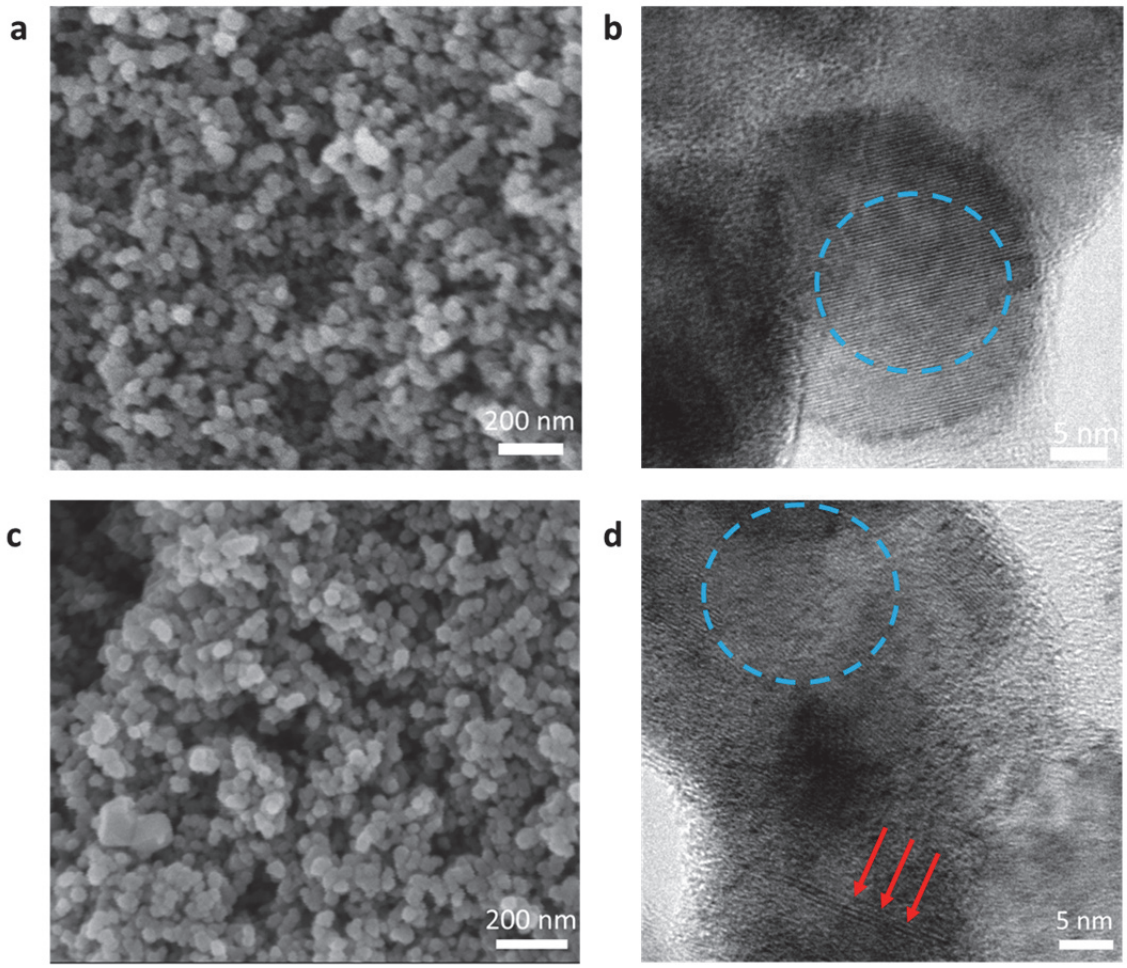

Figure 5.7. (a) SEM and (b) TEM image of an annealed TiO2 film. (c) SEM and (b) TEM image of MoS_2-TiO_2 film. Lattice planes circled in blue corresponds to TiO_2. Red arrows indicate lattice fringes assigned as MoS_2.

5.3.4.2 Photocurrent Studies

The photocurrent response of MoS_2-TiO_2 composite photoanodes is shown in Figure 5.8. Three sets of films were prepared, two containing different quantities of MoS_2 nano-sheets, and a control sample containing TiO_2 only. The successful sensitization of TiO_2 with MoS_2 is evidenced by the extension of the photocurrent response into the visible region of the spectrum relative to the TiO_2 only film. An increase by 500% for the IPCE spectra from the sensitized film relative to the highest photocurrent recorded from the thin films (1.7 nm thick) is observed. It is also noted that the estimated APCE

values are of the same order of magnitude to the values determined for the monolayer MoS_2 film, hence verifying the successful sensitization of TiO_2 with exfoliated MoS_2. Conversely to the thin MoS_2 films where all four of the absorbance peaks contribute to the photocurrent spectrum, (Figure 5.4) for the composite films photocurrent is only recorded at wavelengths corresponding to peaks C/D of the absorption spectrum as predicted from the band alignment detailed in Figure 5.5 (b).

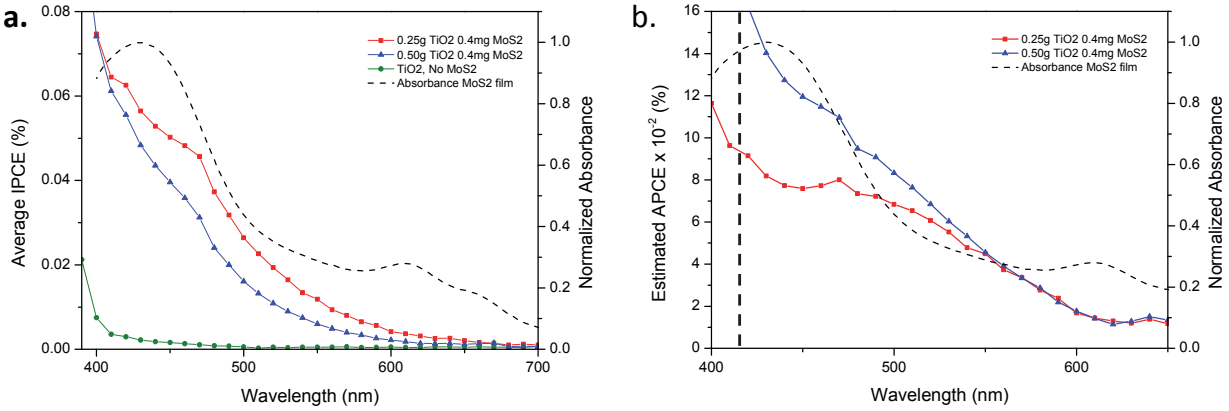

Figure 5.8. (a) Averaged IPCE (3 data sets) photocurrent spectra (solid lines) of MoS_2/TiO_2 composite (blue and red) and TiO_2 only films (green). The spectra are overlaid with the normalized absorbance of 1.7 nm MoS_2. (b) The estimated APCE for the prepared composite films. The estimate is calculated utilizing the known concentration and volume of MoS_2 in each photoanode. The vertical dashed line represents the onset of photocurrent response from TiO_2.

Despite the successful sensitization of TiO_2 evidenced by the extension of the photocurrent response into the visible wavelengths (relative to the TiO_2 only control), we observe relatively low efficiencies with regards to IPCE. Comparison between the different sets of composite films reveals the enhanced IPCE with respect to MoS_2 film loading Figure 5.8 (a)). Contrary to a DSSC where only the surface of the mesoporous structured TiO_2 is sensitized, we speculate that the MoS_2 sheets are randomly dispersed throughout the film such that not all of the TiO_2/electrolyte interface is sensitized. We speculate that a sizeable fraction of the TiO_2/electrolyte interface remains unsensitized because the MoS_2 nanosheets do not uniformly coat the entire TiO_2 surface and that some of the MoS_2 sheets may also be positioned at the interface of TiO_2 particles, inhibiting electron transport. In addition to the MoS_2 crystal distribution, the crystal

size and resultant constraints on charge carriers must also be considered. A carrier lifetime of 100 ps ± 10 ps and a corresponding diffusion length of 450 nm have recently been measured for ultrathin MoS_2 layers.[27] Given that an exciton that reaches a crystal edge will recombine due to crystal defects, the crystal sizes utilized in this work (less than 300 – 800 nm diameter) may limit the photocurrent efficiencies of our devices. The likelihood of an exciton reaching the TiO_2 interface (rather than the crystal edge) is increased for larger sized monolayer crystals. We therefore highlight sensitization with larger crystals as a possible route to higher photocurrent efficiencies.

The above MoS_2-TiO_2 photocurrent spectra can be explained by considering the energy band structures of MoS_2 and TiO_2. The flat band potential of TiO_2 corresponds to the minimum energy required for a photoexcited electron in MoS_2 that is able to inject into the TiO_2 and hence contribute to the photocurrent of the composite photoanode. The flat band position of mesoporous TiO_2 has been shown to be strongly dependent on the pH of the penetrating electrolyte solution,[28] and thus we can estimate the flat band potential of our TiO_2 at approximately -0.80 V (vs. SHE). The relevant band positions/gaps of MoS_2 and TiO_2 are shown on a common scale in Figure 5.9. Evidently, excitons A/B in the lower conduction band of MoS_2 are of insufficient energy to inject into the TiO_2 conduction band. The position of the C/D flat band potential is estimated above the flat band potential of A/B (Figure 5.9) and thus is positioned such that excitons have sufficient energy to inject into the TiO_2 conduction band.[29]

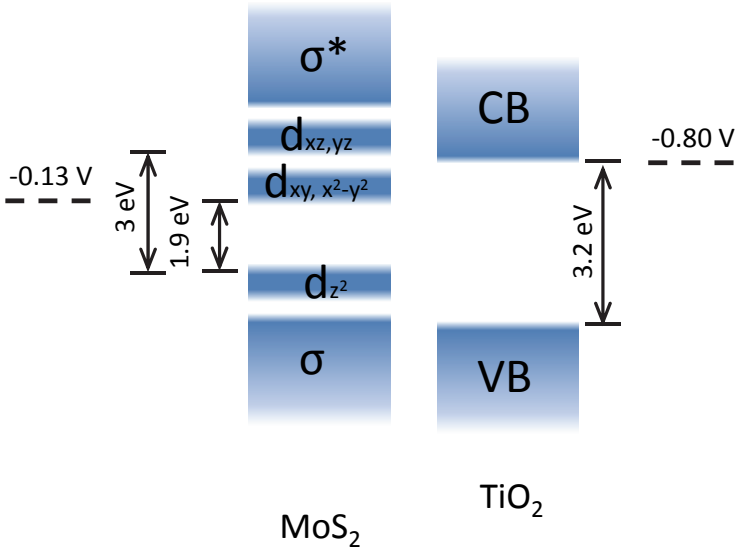

Figure 5.9. Schematic representing the conduction bands (positioning and relevant gaps) of MoS_2 and TiO_2 plotted on SHE scale. The energy levels of TiO_2 and MoS_2 were obtained from ref 28 and ref 21, respectively.

5.4 Conclusions

Fundamental studies on the PEC properties of chemically exfoliated MoS_2 have been conducted. Photocurrent dependence on MoS_2 film thickness reveals a non-linear decay of efficiency with respect to increased film thickness with monolayer MoS_2 films producing the highest photocurrent. The results have been rationalised as stemming from two contributing factors. First, the anisotropy of charge carrier mobility in layered structures and in particular in the re-stacked structure (in contrast to single crystals) of the exfoliated films prevent out-of-plane transport of charges. Second, for the difference in the band structure of monolayer and multilayer MoS_2 lead to increase in the possible decay channels for excitons such that electron injection in to the electrode is kinetically unfavourable.

The aqueous solution-processability of exfoliated MoS_2 and its photoelectrochemical stability have been translated to sensitization of the mesoporous TiO_2. Simple direct adsorption of MoS_2 sheets onto TiO_2 surfaces has been shown to result in effective sensitization and enhanced photocurrent efficiencies of photoanodes. Contrary to the photocurrent spectra of MoS_2 films, in the composite films only the optical transition C/D contributes to the photocurrent. Through photoelectrochemical analysis it has been shown that the conduction band minimum of MoS_2 lies below that of TiO_2 such that electron injection is suppressed.

Appropriate band gap energies and photostability in combination with solution-processable exfoliated routes to MoS_2 nanosheets highlight the material as a promising candidate for a conceptually new type of semiconductor-sensitized PEC solar cells. Optimization of the photoanode architecture and use of other types of transition metal dichalcogenides such as WSe_2 could significantly enhance photocurrent efficiencies.

5.5 References

(1) Wang, F. D.; Tang, R.; Buhro, W. E. *Nano Lett.* **2008**, *8*, 3521.

(2) Morris-Cohen, A. J.; Donakowski, M. D.; Knowles, K. E.; Weiss, E. A. *Journal of Physical Chemistry C* **2010**, *114*, 897.

(3) Morris-Cohen, A. J.; Frederick, M. T.; Lilly, G. D.; McArthur, E. A.; Weiss, E. A. *J. Phys. Chem. Lett.* **2010**, *1*, 1078.

(4) King, L. A.; Riley, D. J. *Journal of Physical Chemistry C* **2012**, *116*, 3349.

(5) Hodes, G. *Journal of Physical Chemistry C* **2008**, *112*, 17778.

(6) Knowles, K. E.; Frederick, M. T.; Tice, D. B.; Morris-Cohen, A. J.; Weiss, E. A. *J. Phys. Chem. Lett.* **2012**, *3*, 18.

(7) Kramer, I. J.; Sargent, E. H. *Acs Nano* **2011**, *5*, 8506.

(8) Gomez-Campos, F. M.; Califano, M. *Nano Lett.* **2012**, *12*, 4508.

(9) Robel, I.; Subramanian, V.; Kuno, M.; Kamat, P. V. *Journal of the American Chemical Society* **2006**, *128*, 2385.

(10) Kongkanand, A.; Tvrdy, K.; Takechi, K.; Kuno, M.; Kamat, P. V. *Journal of the American Chemical Society* **2008**, *130*, 4007.

(11) Pan, Z. X.; Zhang, H.; Cheng, K.; Hou, Y. M.; Hua, J. L.; Zhong, X. H. *Acs Nano* **2012**, *6*, 3982.

(12) Kam, K. K.; Parkinson, B. A. *J. Phys. Chem.* **1982**, *86*, 463.

(13) Kline, G.; Kam, K. K.; Ziegler, R.; Parkinson, B. A. *Solar Energy Materials* **1982**, *6*, 337.

(14) Tributsch, H. *Faraday Discussions* **1980**, *70*, 189.

(15) Djemal, G.; Muller, N.; Lachish, U.; Cahen, D. *Solar Energy Materials* **1981**, *5*, 403.

(16) Matte, H.; Gomathi, A.; Manna, A. K.; Late, D. J.; Datta, R.; Pati, S. K.; Rao, C. N. R. *Angew. Chem.-Int. Edit.* **2010**, *49*, 4059.

(17) Eda, G.; Yamaguchi, H.; Voiry, D.; Fujita, T.; Chen, M. W.; Chhowalla, M. *Nano Lett.* **2011**, *11*, 5111.

(18) Coleman, J. N.; Lotya, M.; O'Neill, A.; Bergin, S. D.; King, P. J.; Khan, U.; Young, K.; Gaucher, A.; De, S.; Smith, R. J.; Shvets, I. V.; Arora, S. K.; Stanton, G.; Kim, H. Y.; Lee, K.; Kim, G. T.; Duesberg, G. S.; Hallam, T.; Boland, J. J.; Wang, J. J.; Donegan, J. F.; Grunlan, J. C.; Moriarty, G.; Shmeliov, A.; Nicholls, R. J.; Perkins, J. M.; Grieveson, E. M.; Theuwissen, K.; McComb, D. W.; Nellist, P. D.; Nicolosi, V. *Science* **2011**, *331*, 568.

(19) Joensen, P.; Frindt, R. F.; Morrison, S. R. *Mater. Res. Bull.* **1986**, *21*, 457.

(20) Divigalpitiya, W. M. R.; Frindt, R. F.; Morrison, S. R. *Science* **1989**, *246*, 369.

(21) Mattheis.Lf *Phys. Rev. Lett.* **1973**, *30*, 784.

(22) Acrivos, J. V.; Liang, W. Y.; Wilson, J. A.; Yoffe, A. D. *Journal of Physics Part C Solid State Physics* **1971**, *4*, L18.

(23) Yoffe, A. D. *Annu. Rev. Mater. Sci.* **1973**, *3*, 147.

(24) Coehoorn, R.; Haas, C.; Dijkstra, J.; Flipse, C. J. F.; Degroot, R. A.; Wold, A. *Phys. Rev. B* **1987**, *35*, 6195.

(25) Mak, K. F.; Lee, C.; Hone, J.; Shan, J.; Heinz, T. F. *Phys. Rev. Lett.* **2010**, *105*, 4.

(26) Oregan, B.; Gratzel, M. *Nature* **1991**, *353*, 737.

(27) Wang, R.; Ruzicka, B. A.; Kumar, N.; Bellus, M. Z.; Chiu, H. Y.; Zhao, H. *Phys. Rev. B* **2012**, *86*, 5.

(28) Rothenberger, G.; Fitzmaurice, D.; Gratzel, M. *J. Phys. Chem.* **1992**, *96*, 5983.

(29) McMenami.Jc; Spicer, W. E. *Phys. Rev. Lett.* **1972**, *29*, 1501.

Chapter 6. Conclusions & Outlook

This thesis has presented research on the fabrication and characterisation of semiconductor sensitized solar cells (SSSCs). The overarching aim of the work was to investigate and expand the underlying scientific understanding of both existing and newly proposed SSSCs. Specifically, much of the work involved probing nano scale surfaces with respect to chemical identity and morphology; an incredibly ambitious task. However, as shown in this thesis, these aspects are significant and influential on the photocurrent of photoanodes and hence the efficiency of solar cells.

The work was split into three more specific topics; two focused on quantum dot (QD) sensitized solar cells (QDSSC) and one on a molybdenum disulphide (MoS_2) sensitized solar cell. With regards to the QDSSCs investigation, the fundamental influence of the QD surface has been highlighted as being particularly crucial to photoanode photocurrents. Through the studies conducted here on QDSSCs, probing the structure and chemical identity of QD surfaces highlighted the importance of this interface on photocurrent measurements.

In Chapter 3, the quantification of the purification procedure and its importance with regards to QD adsorbance was demonstrated. The evolution of surface adsorbance was correlated to the chemical identity and population of the surface bound capping layer (ligands). Non-purified QDs exhibited a low surface coverage with a few large QD agglomerates. QD purification was shown to promote adsorption of QDs at a surface. Coincident with enhanced surface coverage, the morphology of bound agglomerates was also shown to evolve. Specifically, a decrease in the size of QD agglomerates was observed with enhanced purification. Moreover, enhanced photocurrent efficiencies were correlated to a combination of both enhanced QD surface adsorbance and the evolution of QD agglomeration.

The redox couple typically utilized in QDSSCs is the polysulfide electrolyte. Whilst there have been many studies monitoring the influence and stability of single crystal CdSe PEC in the presence of polysulfide there have been a few reports for CdSe QDs. In the case of the bulk CdSe PEC photoanodes, a sulfur substitution of selenium reaction in the outmost layer (~10 nm) was proven. Here, an in depth study into the optical properties, chemical identity and morphology of QD films before and after exposure to

polysulfide are utilized to explain photocurrent results. For the QD only films, both sulfur substitution and deposition into the CdSe QDs/films in combination with film cracking are proposed explanations for the shift in optical bandgap and switching on of photocurrent. The red shift in both the absorbance, and the photocurrent onset is attributed to a change in the QD structure that extends the volume for electronic distribution of the QD exciton.

In the third chapter, two dimensional sheets of molybdenum disulfide (MoS_2) were investigated as a potential candidate for sensitization in SSSCs. Fundamental photocurrent studies on mono- and n- layered (where n = 1 - 20) MoS_2 were conducted revealing photocurrent dependence on film thickness. A non-linear decay of efficiency with respect to film thickness was measured with, most notably monolayer MoS_2 films producing the highest photocurrent efficiencies. These results are attributed to two contributing factors. Firstly, the anisotropy of charge carrier mobility in layered structures and in particular, in the re-stacked structure of exfoliated films preventing out-of-plane transport of charges. Secondly, the difference in the band structure of monolayer and multilayer MoS_2 leading to an increase in the possible decay channels for excitons such that electron injection in to the electrode is kinetically unfavourable in the multilayer films. The flat band potential of n-layered MoS_2 was identified and thus predicted to have favourable alignment with regards to photoinjection into TiO_2. Successful sensitization (electron injection from MoS_2 into TiO_2) was experimentally verified by photocurrent spectra thus demonstrating the viability of monolayer MoS_2 for SSSCs.

6.1 Outlook & Future Direction

Whilst none of the photoanodes prepared in this thesis produce significant photocurrent, the significance of the work resides in the development of both existing and alternative SSSCs. To date, the primary limitation of SSSCs is the lagging (relative to other solar cell technologies) power efficiencies (currently at 5.32 %). As described in the introduction (Chapter 1), device efficiency is set by both the open circuit voltage and short circuit current. Significant enhancement here can be achieved by minimisation of the sensitizer absorbance onset and a decrease in the photovoltaic drop across the cell.

With regards to molybdenum disulphide (MoS_2) monolayer sensitized solar cells the work presented here highlights a significant potential to develop further such sensitized

cells. Through optimization of the photoanode architecture with regard to selective sensitization at the mesoporous TiO_2/electrolyte interface with monolayer MoS_2, significantly higher IPCE efficiencies would be expected. Appropriate band gap energies and photostability, in combination with solution-processable exfoliated routes to MoS_2 nanosheets, highlight the material as a promising candidate for a conceptually new type of semiconductor-sensitized PEC solar cell. Optimization of the photoanode architecture by alternative sample preparation remains a challenge for improved device efficiencies. Fundamental investigations into utilization of alternative monolayer transition metal dichalcogenides (such as WS_2 and WSe_2) could also, perhaps, lead to enhanced photocurrent efficiencies.

In the QDSSC field, expansion of the fundamental scientific understanding of QDs in such cells, is certainly essential to their development. Of particular importance, and as highlighted by the work. In a more general outlook, emphasis on both the standalone and collective choice of materials utilized in the preparation of the cells must be critically reviewed. We highlight the following as areas in need of particular attention;

- **Sensitizer**. An ideal sensitizer requires a low energy onset for photon absorbance, a simplistic and scalable synthesis from abundant, hazard free elements.
- **Electrolyte**. Limited electrolyte redox couples have been tested in SSSCCs. In addition to cell efficiency, particular attention to stability and chemical potential need to be considered for electrolyte selection. Ultimately, a solid state electrolyte is desired.
- **Interfaces**. Particular attention must be made to the interfaces in the SSSC where charge is transferred. Development in this field will enable the minimisation of loss mechanisms and thus enhance cell performance.
- **Cell efficiency**. Reductions of the potential drop across the cell and expansion of the solar harvesting onset and efficiency will contribute to improved power efficiency.

The future of SSSCs will ultimately be assessed by a combination of power efficiency, cost (materials and manufacturing) and cell stability. The cost remains dependent on a combination of materials, safety (hazardous substances entail greater costs), manufacturing processes, module stability and efficiency, (which dictates the solar module value), all of which dictate the solar module viability.

Appendix. The Photoanode Preparation

A.1 Introduction

One of the remaining challenges in the progression of QD sensitized photoanodes is with respect to complete surface coverage with monodisperse QDs. Currently, there exist two fundamentally different routes to QD sensitization; *in situ* and *ex situ* routes. *In situ* sensitization refers to the synthesis of QDs adsorbed onto the mesoporous TiO_2 surface. The QDs are grown either by the successive ionic layer adsorption and reaction (SILAR) or chemical bath deposition (CBD). Typically these routes result in surfaces of high QD coverage, however QD size and shape control is poor. Conversely, the *ex situ* route, whereby the QDs are synthesised prior to sensitization, facilitate good QD size and shape control, however lower surface coverage. The low surface coverage is due to the techniques reliance on diffusion into the highly porous TiO_2 a time consuming process. *Ex situ* sensitization has been utilized in various techniques. For example, direct absorbance and electrophoretic deposition of QDs onto TiO_2 have been realised. The third and most common *ex situ* technique is a bifunctional linker approach, a two-step process whereby the mesoporous TiO_2 layer is first functionalised with the linker, followed by sensitization with the QD.

In this appendix we present initial results on an alternative route to the assembly of the photoanode removing the reliance of the *ex situ* sensitization on QD diffusion into the mesoporous structure. Here, QDs are prepared by hot injection technique, purified and sensitized with the linker molecule 3-mercaptopropionic acid (3-MPA) at the surface of powdered TiO_2. The sensitized TiO_2 is subsequently processed into a film by one of the following routes pressing[1] and/or annealing.

A.2 Methods

A.2.1 Materials

The linker molecule and sensitizing solutions were prepared with 3-mercaptopropionic acid (3-MPA, 99+ %, Aldrich), acetonitrile (anhydrous 99.8 %, Aldrich) TEC8 glass plate fluorinated tin oxide (FTO) coated glass slides (1 x 2.5 cm) (Dyesol) were used as optically transparent electrodes (OTE). Hydrochloric acid (HCl, 37 %, VWR), nitric acid (HNO_3, 68 %, BDH), sulfuric acid (H_2SO_4, 95 %, VWR) and

hydrogen peroxide (H_2O_2, 30 %, Fischer Scientific) were used in the cleaning procedure of the FTO. Degussa P25 TiO_2 was used as received.

A.2.2 Preparation of CdSe-TiO_2 Photoanodes

QDs were synthesized by the hot injection technique (as detailed in Chapter 2). For each set of photoanodes 1 M 3-MPA (acetonitrile) linker molecule was added to the TiO_2 powder. The solution was left to stir for >12 h. The solutions were then centrifuged, the TiO_2 pellet dried, re-dispersed in toluene and subsequently re-centrifuged. 4.38 mol of CdSe QDs was then added to TiO_2 with 5 ml of toluene and left to stir for >4 days. Upon addition of a further 5 ml toluene the solutions are left to separate. The opaque supernatant was then extracted by pipette. To each of the samples ethanol was added in the ratio TiO_2 : ethanol 1 : 4.4 and left to stir for >12 h. 15µL of each sample were used to prepare films on the clean, conductive fluorine doped tin oxide (FTO) using the doctor-blade technique. Annealed samples were treated at 300°C for 30 min in an argon atmosphere. Pressure treated (pressed) samples were pressed in an isostatic press at 30 MPa for 30 s.

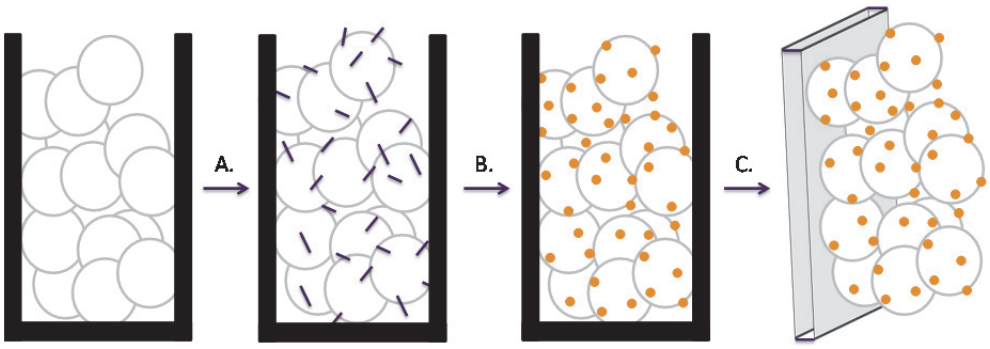

Figure A.1. Schematic for the three step assembly of photoanodes. A. Addition of 1 M 3-MPA to the TiO2 particles. B. Addition of QD sol. C. Doctor blade QD-3-MPA-TiO_2 onto FTO conductive glass.

Between measurements, all QD solutions and electrodes were stored in the dark. Figure A.1 shows a schematic representation of the preparation of the QD sensitized photoanode.

A.2.3 Preparation of CdSe QD Films

A concentrated CdSe QD paste was prepared by centrifugation of the QD sol and re-dispersion in a 1 ml toluene and 1 ml ethanol mix. 15µL of QD sol was used to prepare films on the clean, conductive fluorine doped tin oxide (FTO) using the doctor-blade technique. Samples were split into four batches; untreated, annealed, pressed and annealed and pressed. Three samples were prepared for each batch.

A.3 Results

A.3.1 Optical Analysis

UV-visible spectroscopy was conducted to monitor the QDs with respect to size and size distribution as shown in Figure A.2. The QD films are here compared to the original QD sol.

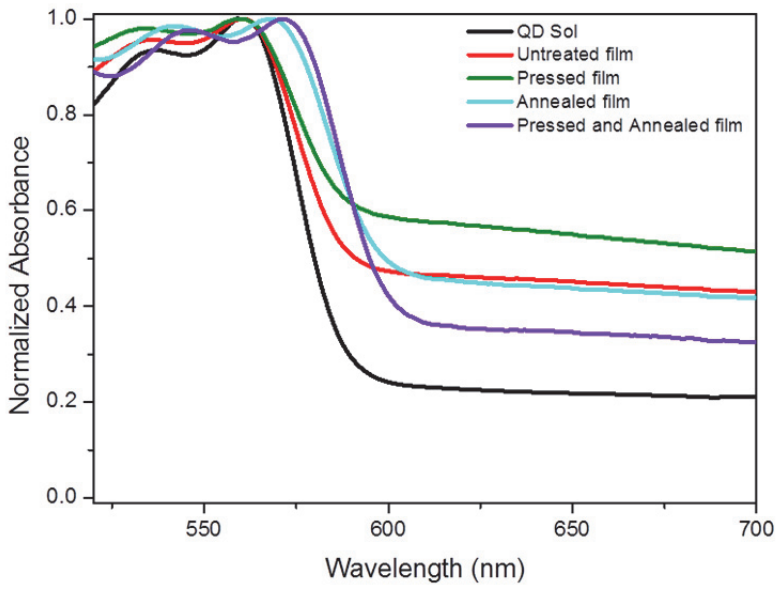

Figure A.2. Normalized UV-visible absorbance spectra for the QD sol and films; untreated (red), pressed (green), annealed (blue) and pressed and annealed (purple).

Sample	Peak width @ 0.98 Normalized absorbance (nm)	Peak position (nm)
QD sol	8.5	561
Untreated film	10	561
Pressed film	12	560
Annealed film	11	568
Pressed and annealed film	10	571

Table A.1. Summary of UV-Visible absorbance spectra – peak positions and widths for each of the samples prepared.

Peak positions and widths are detailed in Table A.1. It is evident that the average QD size (peak position) for optically active QDs in the untreated and pressed samples remains constant from sol to film. Conversely, for the annealed films, there is a red shift in the peak position by ~8nm. With respect to the peak widths, the QD sol has the narrowest width. Upon casting into the films the breadth of the peaks widen.

The influence of annealing and pressing on QD film optical properties was also monitored by photoluminescence (Figure A.3 and Figure A.4 respectively).

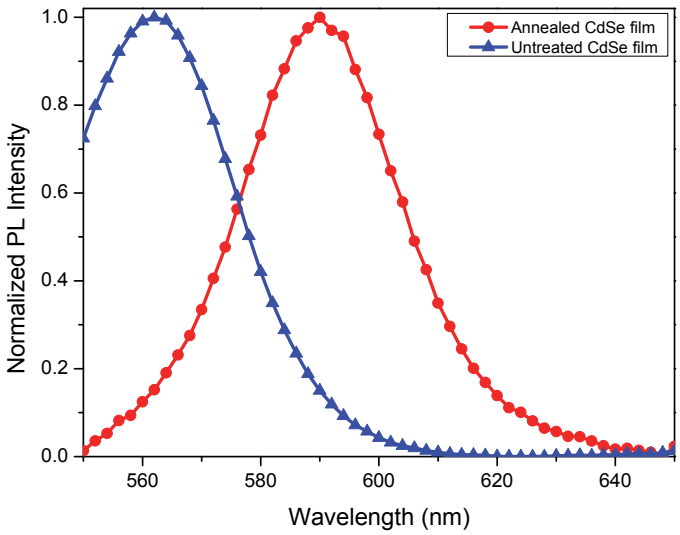

Figure A.3. Normalized photoluminescence spectra for an untreated (blue) and annealed (red) CdSe film.

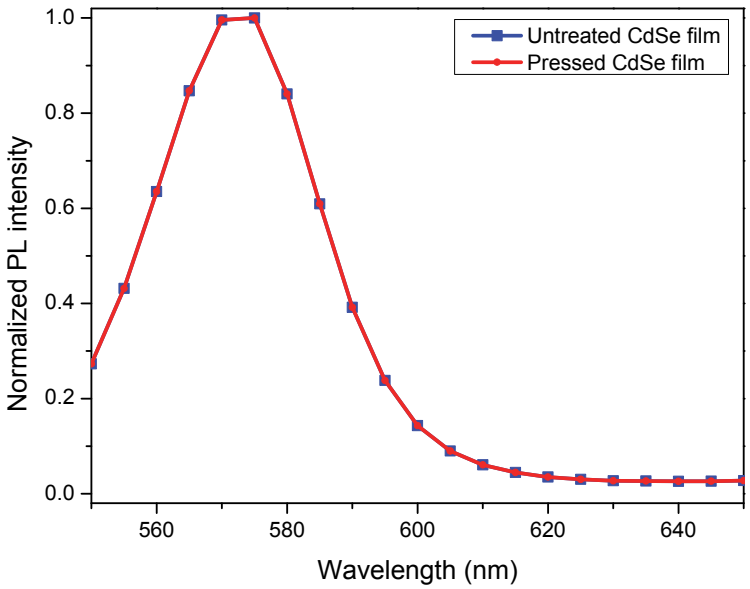

Figure A.4. Normalized photoluminescence spectra of untreated (black) and pressed (red) CdSe films.

A.3.2 Photocurrent Spectra

A.3.2.1 Delamination

Throughout studies of pressed films there were issues for some photoanodes with respect to delamination and film cracking post submersion in electrolyte. Delamination was visually observed for some photoanodes. Film delamination appeared to be randomly distributed across the films prepared with respect to composition, processing procedure and age. Delamination was readily observed during photocurrent measurements where the photocurrent efficiency rapidly decreased with respect to time as illustrated in Figure A.5. Films that showed any visual signs of delamination were disregarded from study.

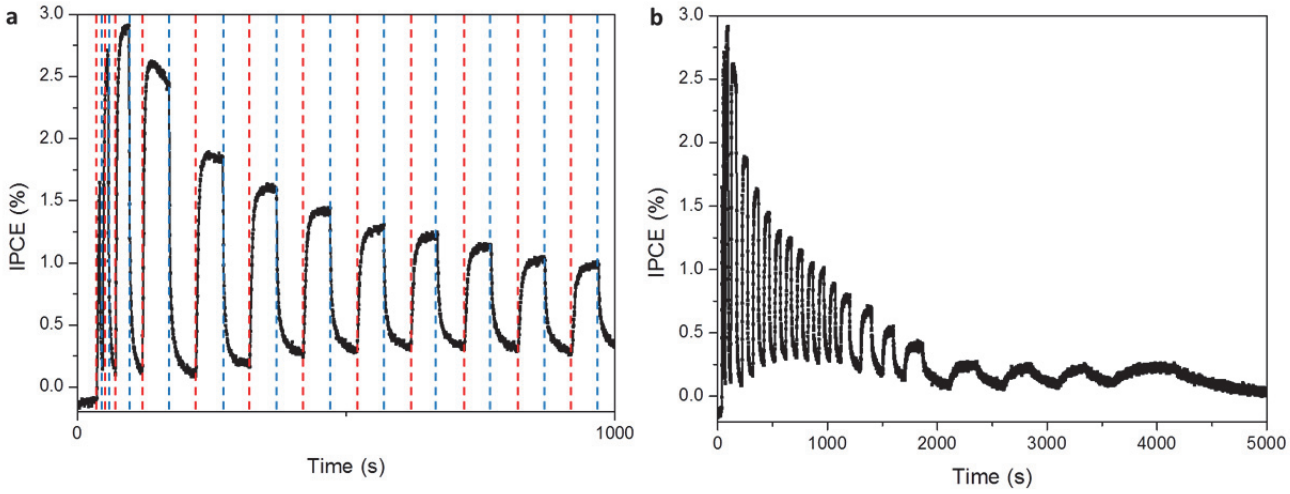

Figure A.5. Transient Photocurrent spectra of a pressed TiO_2 only film. The measurement is conducted with chopped illumination (frequency of chopping was altered throughout measurement). (a) is enlarged over the first 1000 s, (b) full data. Red lines (dotted) represent the turning on of light (400nm), blue lines are where the light is blocked.

A.3.2.2 Influence of Annealing and Pressing on the Photocurrent

Quantum dot sensitized titanium dioxide photoanodes were prepared as described in Chapter 4. Photocurrent measurements were conducted as shown in Figure A.6. The data has been normalized to enable comparison with regards to the spectra response. The extension of the photocurrent onset from 400 nm (TiO_2) into the red for each of the samples presented in Figure A.6 demonstrates the success of the preparation and processing routes utilized in this appendix (and Chapter 4).

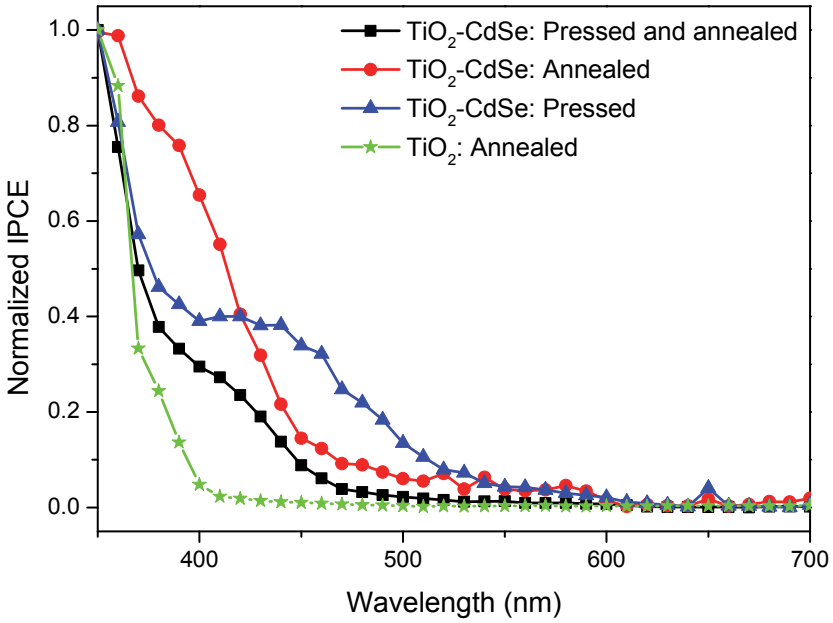

Figure A.6. Normalized average IPCE spectra for pressed (blue), annealed (red) and pressed and annealed (black) QD sensitized TiO_2 photoanodes. TiO_2 only is also shown for reference (green). All measurements were conducted in 0.5 M Na_2SO_3, pH 7.

A.4 Preliminary Conclusions

The absorbance data shows a red shift in the first excitonic peak position post annealing implying an increase in the size of QDs in the film. Conversely, a blue shift in the onset of the photocurrent spectra is observed post annealing inferring a decrease in the size of the QDs adsorbed (and hence able to inject) at the TiO_2 surface. These are, however, preliminary findings and further characterization would be required to confirm this hypothesis.

A.5 References

(1) Wijayantha, K. G. U.; Peter, L. M.; Otley, L. C. *Solar Energy Materials and Solar Cells* **2004**, *83*, 363.